

Decoherence of coupled solid state qubits

von Markus János Storcz

Diplomarbeit in Physik
angefertigt am

Lehrstuhl für Theoretische Festkörperphysik
CeNS und Sektion Physik
Ludwig-Maximilians-Universität München

vorgelegt der

Mathematisch-Naturwissenschaftlichen Fakultät
der Rheinischen Friedrich-Wilhelms-Universität Bonn



im September 2002

BONN-IB-2002-16

Ich versichere, daß ich diese Arbeit selbständig verfaßt und keine anderen als die angegebenen Quellen und Hilfsmittel benutzt, sowie die Zitate kenntlich gemacht habe.

Referent: Prof. Dr. Jan von Delft
Korreferent: Prof. Dr. Hartmut Monien

Contents

Contents	1
1 Introduction	3
1.1 Quantum computation	3
1.2 Realizations of quantum bits	3
1.3 Coupled qubits	4
1.4 Overview	4
2 Modelling the two-qubit Hamiltonian	6
2.1 Josephson effect	6
2.2 Single-qubit Hamiltonian	6
2.3 Two-qubit Hamiltonian	10
2.4 Eigenenergies and eigenstates of the two-qubit Hamiltonian	12
3 Weak symmetric driving in ϵ	16
4 Bloch-Redfield-Formalism	22
4.1 Redfield relaxation tensor	22
4.2 Two qubits coupled to two distinct baths	23
4.3 Two qubits coupled to one common bath	24
4.4 Dynamics of dissipative coupled flux qubits	25
4.5 Temperature dependence of the rates	29
4.6 Discussion of the renormalization effects	31
5 Gate Quality Factors	36
5.1 Implementation of the XOR-operation	37
5.2 Temperature dependence	38
5.3 Dependence on the dissipation strength	41
5.4 Time resolved XOR operation	42
6 Flux transformer	46
6.1 Josephson field-effect transistor (JoFET)	46
6.2 Properties of the Flux Transformer	47
6.2.1 No switch	47
6.2.2 Tunable Josephson junction as a switch	49
6.3 RSJ-model	50

7	Conclusions	52
8	Deutsche Zusammenfassung	54
	Acknowledgements	56
A	Eigenvalues and eigenstates of the two qubit Hamiltonian	57
B	Matrix representation of σ_z	59
C	Calculation of the rates	60
	C.1 Two qubits coupled to two distinct baths	60
	C.2 Two qubits coupled to one common bath	64
D	Calculation of the renormalization effects	65
	List of symbols	69
	List of symbols	69
	List of constants	70
	List of Figures	71
	List of Tables	73
	Bibliography	74

Chapter 1

Introduction

1.1 Quantum computation

It has been shown that several existing algorithmic problems might gain a significant speedup by the use of quantum computation [1, 2, 3]. Different from a classical bit, a quantum bit (in the following called “qubit”) can be prepared in a superposition of states, namely $|\psi\rangle = \alpha|0\rangle + \beta|1\rangle$. Furthermore, systems of at least two qubits can be prepared in an entangled state, e.g. $|\psi\rangle = (1/\sqrt{2})(|0\rangle|0\rangle + |1\rangle|1\rangle)$ [4]. To perform operations with a qubit quantum coherence has to be kept over a sufficiently long timescale.

David DiVincenzo summarized the design requirements for a quantum computer (a device which acts on a scale on which it obeys the laws of quantum mechanics) [5]. He introduced five requirements for such a quantum computer: (i) The degrees of freedom needed to compute and hold the data should be available as dimensions of the Hilbert space of the quantum system. As a consequence the basis states must be exactly enumerable, i.e. it is not sufficient to define basis states as two plus/minus one charge on a quantum dot. (ii) It should be possible to prepare a well-defined initial state, which is for superconducting solid state qubits relatively easily achieved by simply cooling down the system. Qubits based on Nuclear Magnetic Resonance (NMR), where an ensemble of many spins is observed, are operated at room temperature. Therefore, in NMR experiments the initial state is an equally populated state. (iii) Quantum coherence needs to be kept over a sufficiently long time; more precisely, it should be possible to at least perform 10^5 quantum logic operations within the dephasing time. (iv) One must at least have complete control over two independent unitary gates. (v) It should be possible to apply a “strong” (von Neumann-type) measurement to each qubit. However, for example in NMR quantum computation only repeated weak measurements (without a complete collapse of the wavefunction) of an ensemble of many spins are performed. The fact that NMR qubits have already been used to build a small *working* quantum computer [6], shows that not all of these requirements need to be strictly fulfilled in practice.

1.2 Realizations of quantum bits

Today there exist several proposals [7, 8] for the realisation of devices that might be suitable as quantum bits. Examples are atoms trapped in an ion trap or optical realizations of qubits. Today the most advanced experimental realizations are qubits based on Nuclear Magnetic

Resonance [6]. Shortcomings of these NMR qubits are the poor scalability to systems with more than approximately ten useable qubits and the huge experimental setups needed for NMR quantum computation. Solid state realisations such as superconducting loops (“flux qubits”), where the current states define the basis, or quantum dots (either “spin” [9] or “charge” [10, 11] qubit), have the advantage of being easily scalable to large numbers of qubits which might be individually addressed. Drawbacks are relatively short coherence times, due to the high number of degrees of freedom in solid state devices, and usually (similar to the NMR qubits) also the huge experimental setups (e.g. dilution refrigerators). However, superconducting qubits are promising candidates for the realization of a quantum computer [12]. Usually any system of qubits is coupled to a dissipative environment which causes decoherence, i.e. dephasing and relaxation. The dephasing time is the characteristic time scale on which the off-diagonal elements of the density operator describing the dynamics of our system turn to zero, and the relaxation time is the characteristic time scale on which the diagonal elements of the density matrix go towards the value given by the Boltzmann factors.

1.3 Coupled qubits

About decoherence of single solid state qubits quite a lot is known [13, 14, 15]. Not so much is known about coupled qubits [16, 17, 18, 19]. However, only for coupled qubits, the key properties of entanglement can be studied. At least two qubits are needed to perform a CNOT (or XOR) operation. This gate is important because any unitary transformation might be decomposed into (several) single-qubit gates and CNOT gates. Therefore the CNOT (XOR) gate is the most common building block of a universal quantum computer [20].

The goal of this thesis is therefore to study in some detail the decoherence properties of two coupled qubits for a specific model system, in which the decoherence is generated by coupling the qubit to a standard bosonic environment. The properties of two inductively coupled charge qubits, with an inter-qubit coupling of the type $\sigma_y^{(1)} \otimes \sigma_y^{(2)}$ ($\sigma_{x,y,z}$ denote the Pauli-spin-matrices), were investigated in [16]. In contrast, we shall study here a two-qubit Hamiltonian that describes two *flux* qubits coupled inductively by a flux transformer, which gives rise to a $\sigma_z^{(1)} \otimes \sigma_z^{(2)}$ coupling. This type of coupling actually occurs quite often in other pseudo-spin systems, too. It arises, for example, also for capacitively coupled charge qubits, that can be realized by connecting superconducting boxes directly via a capacitor. We shall find that the $\sigma_z^{(1)} \otimes \sigma_z^{(2)}$ coupling leads to results very different from those of the $\sigma_y^{(1)} \otimes \sigma_y^{(2)}$ coupling. We shall also study the differences between coupling both qubits to the same bath, or each to its own bath.

1.4 Overview

This thesis is organized as follows: In chapter 2 we discuss structure and properties, such as eigenenergies and transition frequencies, of the two-qubit system Hamiltonian and provide a convenient representation. In chapter 3 we investigate the effects of weak symmetric driving in the energy bias ϵ . Furthermore we illustrate the behaviour of the transition frequencies of the unperturbed Hamiltonian. In chapter 4 we study the dynamics of the system and evaluate decoherence times by applying the well established Bloch-Redfield formalism [21, 22], which has been shown to be equivalent to path-integral methods [23]. We then use in chapter 5

several standard quantifiers from quantum information theory to provide a convenient way to characterize the two qubit system: to quantify the efficiency of the gate operations which might be performed with the two coupled solid state qubits, we calculate the gate quality factors introduced in [24]. In chapter 6 we investigate the properties of a flux transformer, which is a device to couple two flux qubits inductively. We discuss a JoFET (Josephson field effect transistor) as a switch, which might be inserted into the flux transformer loop surrounding the two qubits to turn on and off the coupling between the two qubits. Since this device introduces a noise source that leads to decoherence, we investigate in chapter 6 the noise properties of the flux transformer.

Chapter 2

Modelling the two-qubit Hamiltonian

2.1 Josephson effect

Cooper pairs on superconducting electrodes separated by a thin insulator may tunnel through the thin non superconducting layer. There will be a phase difference between the wavefunctions in the two electrodes [25]. According to Josephson at zero voltage a supercurrent

$$I_s = I_c \sin \Delta\varphi \quad (2.1)$$

flows. Here I_c is the maximum possible supercurrent passing the junction. In the case of an applied electromagnetic field the phase difference $\Delta\varphi$ is replaced by the gauge invariant phase difference γ which is defined by

$$\gamma \equiv \Delta\varphi - \frac{2\pi}{\Phi_0} \int \mathbf{A} \cdot d\mathbf{s}. \quad (2.2)$$

The integration is from one electrode to the other and effects of a magnetic field are treated by introducing the vector potential \mathbf{A} . The coupling free energy is given by

$$F = -E_J \cos \Delta\varphi, \text{ with } E_J \equiv \frac{\hbar I_c}{2e}, \quad (2.3)$$

where we disregarded a possible constant energy offset.

Figure 2.1 is an equivalent circuit diagram of a Josephson tunnel junction. In figure 2.1 the junction is shunted by a capacitor reflecting the geometric shunting capacitance between the two superconducting electrodes. Thus the two superconducting electrodes effectively behave like a parallel plate capacitor and the junction is characterized by the Josephson energy E_J and the single-electron charging energy $E_C = e^2/2C_t$, where C_t is the total capacitance of the superconducting electrode.

2.2 Single-qubit Hamiltonian

There exist several implementations of superconducting solid state qubits [26, 27, 28]. One implementation of a solid state qubit device is an rf-squid, which consists of a superconducting



Figure 2.1: Left picture is an equivalent circuit diagram of a Josephson junction. The junction itself is depicted by a cross, and might be described as a junction that is shunted by a shunt capacitor C , reflecting the geometric capacitance between the electrodes. E_J is the Josephson energy defined in equation (2.3). The right picture is a SEM image of a Josephson junction (TU Delft). A thin oxide layer is fabricated in-between the aluminium layers.

loop interrupted by a Josephson junction. For a simple single Josephson junction rf-squid the phase difference across the junction is connected to the flux Φ in the loop and the Hamiltonian including contributions from Josephson coupling, charging energy and magnetic contributions reads [14]

$$\mathbf{H} = \frac{Q^2}{2C_J} - E_J \cos\left(2\pi \frac{\Phi}{\Phi_0}\right) + \frac{(\Phi - \Phi_x)^2}{2L}. \quad (2.4)$$

Here $\Phi_0 = h/2e$ is the magnetic flux quantum, Q is the charge on the electrodes, L the self-inductance of the loop and C_J the capacitance of the junction. The charge $Q = -i\hbar\partial/\partial\Phi$ is canonically conjugate to the flux Φ . In the case of a large self-inductance and if the external applied flux is close to $\Phi_x = \frac{1}{2}\Phi_0$ the first two terms of (2.4) form a double-well potential around $\frac{1}{2}\Phi_0$ as depicted in figure 2.3.

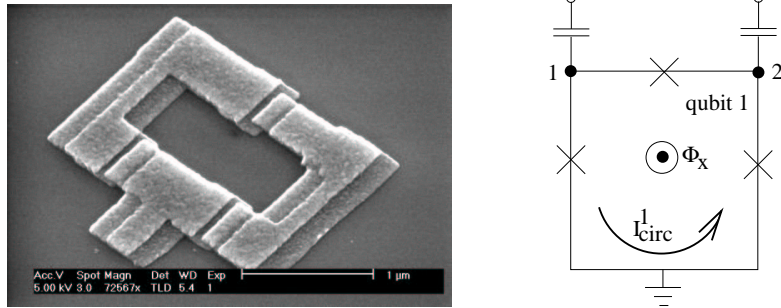


Figure 2.2: The Delft design of a flux qubit: Superconducting loop interrupted by three Josephson junctions. Left figure: SEM picture by A.C. Wallast (TU Delft); right figure: equivalent circuit diagram. The nodes 1 and 2 are superconducting islands. They are connected to capacitors reflecting both the capacitance between the islands and ground and background charges. Usually the nodes are not connected by gate capacitors to gate voltages. The flux Φ_x is taken out of the page.

The device first developed at the TU Delft and MIT [29] depicted in figure 2.2 is a low

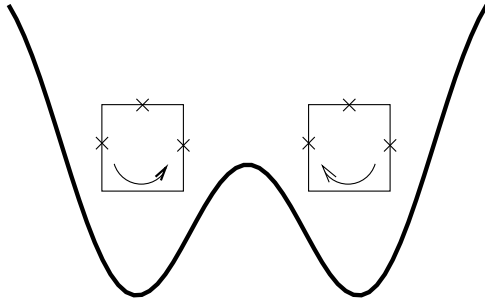


Figure 2.3: Schematic representation of the persistent-current states of a superconducting qubit loop. For large self-inductance of the loop and flux bias near half a flux quantum the two potential terms of (2.4) form a double-well potential.

inductance superconducting loop interrupted by three Josephson tunnel junctions. The loop is biased by an externally applied flux Φ_x which induces a persistent supercurrent in the loop. In this device the third junction has a slightly smaller Josephson energy \tilde{E}_J than the two other junctions, namely for $\tilde{E}_J/E_J > 0.5$ a double-well potential is formed. Then the two states are nearly degenerate, separated by an energy barrier. The phase differences across the three junctions are constrained by fluxoid quantization ($\gamma_1 + \gamma_2 + \gamma_3 = 2\pi(\Phi/\Phi_0)$), and the energy landscape has the following shape [29]

$$U(\gamma_1, \gamma_2) = -E_J \cos \gamma_1 - E_J \cos \gamma_2 - \tilde{E}_J \cos(2\pi\Phi_x/\Phi_0 - \gamma_1 - \gamma_2). \quad (2.5)$$

At low temperatures only the lowest state in the well contributes, and phonons are suppressed. The two states of our two level system then correspond to currents running clockwise and counterclockwise through the loop as depicted in figure 2.3. Here the classical states have well defined flux, therefore these qubits are called ‘flux-qubits’. Flux and charge are quantum mechanical canonical conjugate variables in this system, so a state with well defined flux must have large quantum fluctuations in the charge and vice versa. In our case the Josephson energy E_J is much bigger than the charging energy E_C , so that the phase is well defined and the charge fluctuates. Here the phase barrier originates from extra inductive or Josephson energies and tunneling between the two wells is driven by capacitive quantum fluctuations. A comprehensive review of the work done on flux qubits in Delft can be found in [13].

The resulting two level system might be represented in spin-1/2 notation using the Pauli matrices in standard representation

$$\mathbf{H} = -\frac{1}{2}\epsilon\hat{\sigma}_z - \frac{1}{2}\Delta\hat{\sigma}_x, \quad (2.6)$$

where ϵ is the asymmetry e.g. the energy bias and Δ is the transmission amplitude through the barrier. This provides a convenient representation of the single-qubit Hamiltonian. Here we focus on the behaviour of the system near the degeneracy point at $f = 1/2$ (the externally applied bias flux Φ_x is near $(1/2)\Phi_0$) where only two states are important because all other states have much higher energies and can thus be neglected. However, if the externally applied flux Φ_x is swept away from $(1/2)\Phi_0$, or temperature is increased, also higher energy levels might contribute.

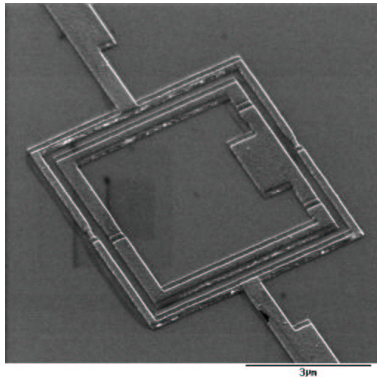


Figure 2.4: Superconducting single qubit loop and the switching SQUID (outer loop). The outer SQUID loop is used as a measurement device to read out the state of the qubit. SEM picture by A.C.J. ter Haar (TU Delft).

Quantum coherent Rabi-oscillations have already been observed in charge qubit devices [30]. Recently Nakamura et al. also reported the observation of quantum coherent Rabi-oscillations in flux qubit devices [31]. However, compared to earlier qubit realizations depicted in figures 2.2 and 2.4, Nakamura et al. used a strongly modified qubit design where sensitivity to noise is greatly reduced. They used a gradiometer type qubit, where no net flux is coupled into the superconducting qubit loop.

The state of the single qubit might be measured for example by fabricating a DC-SQUID around the qubit loop, and measuring the switching current I_{SW} when increasing the bias current [13, 32]. The switching current I_{SW} , at which the DC-SQUID switches from the supercurrent branch to a finite voltage state, is a measure for the magnetic flux in the SQUID. Thus by measuring the flux through the DC-SQUID loop, the state of the qubit can be determined. In other words, when ramping the bias current the system and the meter get entangled, as required for a measurement. But, one should note that the switching current in the measurement is not perfectly correlated with the state of the qubit and strictly speaking no von Neumann measurement is performed [33]. Figure 2.4 depicts both the qubit and the readout device described here.

Coupling of the two level system to a dissipative environment is conveniently modeled by the Spin-Boson model [34] where the qubit is described as a spin-1/2 coupled to a bosonic bath (harmonic oscillator bath). Every Gaussian noise source may be modeled (when introducing a corresponding spectral function) as a harmonic oscillator bath [35]. For example the impedances in our circuit leading to Johnson-Nyquist voltage noise and therefore to flux noise can be described by LC-oscillators. Thus it is possible to model flux noise which is the most important source of decoherence in flux qubits. But, $1/f$ -noise is not Gaussian, and thus $1/f$ -noise can not be modeled by an environmental bath of harmonic oscillators.

2.3 Two-qubit Hamiltonian

To model the two qubit Hamiltonian, we first describe each of the two qubits by the single qubit Hamiltonian (2.6) which is reflected by the sum over the two single qubit Hamiltonians in (2.7). Next, we insert an inter-qubit coupling term that originates either from direct inductive coupling of the qubits, coupling via a flux transformer as investigated in chapter 6, or other equivalent coupling schemes. In our case the inter-qubit coupling term is of the form $\sigma_z^{(1)} \otimes \sigma_z^{(2)}$. The importance of this type of inter-qubit coupling was already emphasized in chapter 1. Here, K is the strength of the inter-qubit coupling. Without taking into account the effects of the dissipative environment, the two qubit Hamiltonian reads

$$\mathbf{H}_{2qb} = \sum_{i=1,2} \left(-\frac{1}{2}\epsilon_i \hat{\sigma}_z^{(i)} - \frac{1}{2}\Delta_i \hat{\sigma}_x^{(i)} \right) - \frac{1}{2}K \hat{\sigma}_z^{(1)} \hat{\sigma}_z^{(2)}. \quad (2.7)$$

We model the dissipative (bosonic) environment as either a common bath or as two distinct baths of harmonic oscillators coupling to the $\hat{\sigma}_z$ -components of the two qubits. For example, long correlation length electromagnetic noise which is irradiated onto the qubit circuit or the flux transformer (the flux transformer will be further elucidated in chapter 6) is a dissipative environment which affects both qubits in the same correlated manner. This dissipative environment might be described by coupling the two qubits to one common bath of harmonic oscillators. Short correlation length irradiation, or the readout of only one of the qubits by electronics might be described as coupling each of the two qubits to one of two uncorrelated baths of harmonic oscillators. This means that each qubit couples exclusively to one of two baths which are uncorrelated. One should note that if the number of qubits is increased to more than two qubits, there might also occur dissipative effects which neither affect all qubits nor only a single qubit, but rather a cluster of qubits thus enhancing the complexity of our considerations [36].

In the first case (2.8) each qubit couples to its own harmonic oscillator bath via the coupling term $\hat{\sigma}_z^{(i)} \hat{X}^{(i)}$, $i = 1, 2$ which bilinearly couples a qubit to the coordinate $\hat{X}^{(i)}$ of the harmonic oscillator

$$\mathbf{H}_{op}^{2b} = \sum_{i=1,2} \left(-\frac{1}{2}\epsilon_i \hat{\sigma}_z^{(i)} - \frac{1}{2}\Delta_i \hat{\sigma}_x^{(i)} + \frac{1}{2}\hat{\sigma}_z^{(i)} \hat{X}^{(i)} \right) - \frac{1}{2}K \hat{\sigma}_z^{(1)} \hat{\sigma}_z^{(2)} + \mathbf{H}_{B_1} + \mathbf{H}_{B_2}, \quad (2.8)$$

where \mathbf{H}_{B_i} , $i = 1, 2$, are two distinct baths of harmonic oscillators. We again sum over the two qubits. In the case of two qubits coupling to one common bath, we model our two qubit system with the Hamiltonian

$$\mathbf{H}_{op}^{1b} = \sum_{i=1,2} \left(-\frac{1}{2}\epsilon_i \hat{\sigma}_z^{(i)} - \frac{1}{2}\Delta_i \hat{\sigma}_x^{(i)} \right) + \frac{1}{2} (\hat{\sigma}_z^{(1)} + \hat{\sigma}_z^{(2)}) \hat{X} - \frac{1}{2}K \hat{\sigma}_z^{(1)} \hat{\sigma}_z^{(2)} + \mathbf{H}_B, \quad (2.9)$$

where \hat{X} is the coordinate of the bath of harmonic oscillators and \mathbf{H}_B denotes one common bath of harmonic oscillators.

The singlet/triplet basis states are defined according to $|\uparrow\uparrow\rangle := (1, 0, 0, 0)^T$, $(1/\sqrt{2})(|\uparrow\downarrow\rangle + |\downarrow\uparrow\rangle) := (0, 1, 0, 0)^T$, $|\downarrow\downarrow\rangle := (0, 0, 1, 0)^T$ and $(1/\sqrt{2})(|\uparrow\downarrow\rangle - |\downarrow\uparrow\rangle) := (0, 0, 0, 1)^T$; here we denote the qubit states by clockwise and counterclockwise flowing currents in the qubit. Sometimes it is also convenient to write $|\uparrow\uparrow\rangle = |11\rangle$, $(1/\sqrt{2})(|\uparrow\downarrow\rangle + |\downarrow\uparrow\rangle) = (1/\sqrt{2})(|10\rangle + |01\rangle)$,

$|\uparrow\uparrow\rangle = |00\rangle$ and $(1/\sqrt{2})(|\uparrow\downarrow\rangle - |\downarrow\uparrow\rangle) = (1/\sqrt{2})(|10\rangle - |01\rangle)$. In singlet/triplet basis the Hamiltonian \mathbf{H}_{2qb} , equation (2.7), of the two qubit system (not including dissipative effects, e.g. neither the coupling to the bath nor the bath itself) assumes the matrix form

$$\mathbf{H}_{2qb} = -\frac{1}{2} \begin{pmatrix} \epsilon + K & \eta & 0 & -\Delta\eta \\ \eta & -K & \eta & \Delta\epsilon \\ 0 & \eta & K - \epsilon & \Delta\eta \\ -\Delta\eta & \Delta\epsilon & \Delta\eta & -K \end{pmatrix} \quad (2.10)$$

with $\epsilon = \epsilon_1 + \epsilon_2$, $\eta = (\Delta_1 + \Delta_2)/\sqrt{2}$, $\Delta\eta = (\Delta_1 - \Delta_2)/\sqrt{2}$ and $\Delta\epsilon = \epsilon_1 - \epsilon_2$. If we now also regard the dissipative environment, we may distinguish the two cases of one common and two distinct baths discussed above. In the case of two qubits coupling to two distinct baths the system is described by the Hamiltonian (2.8), which possesses the following matrix form

$$\mathbf{H}_{op}^{2b} = -\frac{1}{2} \begin{pmatrix} \epsilon - s + K & \eta & 0 & -\Delta\eta \\ \eta & -K & \eta & \Delta\epsilon - \Delta s \\ 0 & \eta & K + s - \epsilon & \Delta\eta \\ -\Delta\eta & \Delta\epsilon - \Delta s & \Delta\eta & -K \end{pmatrix} \quad (2.11)$$

with $s = \hat{X}_1 + \hat{X}_2$ and $\Delta s = \hat{X}_1 - \hat{X}_2$. In the case of two qubits with equal parameters (i.e. both qubits have the same energy bias $\epsilon_1 = \epsilon_2$ and transmission amplitude $\Delta_1 = \Delta_2$), coupling to two uncorrelated distinct baths the Hamiltonian reads in the singlet/triplet basis

$$\mathbf{H}_{op}^{2b} = -\frac{1}{2} \begin{pmatrix} \epsilon - s + K & \eta & 0 & 0 \\ \eta & -K & \eta & -\Delta s \\ 0 & \eta & K - \epsilon + s & 0 \\ 0 & -\Delta s & 0 & -K \end{pmatrix}. \quad (2.12)$$

Here, the bath mediates transitions between the singlet and triplet states, the singlet is not a protected subspace (see below).

In the case of two qubits with equal parameters, coupling to one common bath, the matrix (2.12) simplifies to

$$\mathbf{H}_{op}^{1b} = -\frac{1}{2} \begin{pmatrix} \epsilon - s + K & \eta & 0 & 0 \\ \eta & -K & \eta & 0 \\ 0 & \eta & K - \epsilon + s & 0 \\ 0 & 0 & 0 & -K \end{pmatrix}, \quad (2.13)$$

where $s = 2\hat{X}$ and $\Delta s = 0$. One directly recognizes that compared to (2.12) in this case thermalization to the singlet state is impeded, because (2.13) is block-diagonal in the singlet and triplet states. It splits into a part that is already diagonal (the singlet) and an upper three by three matrix (the triplet part). The singlet and triplet states are completely decoupled from each other and the singlet is in the case of one common bath completely decoupled from the bath and thus from any dissipative effects. Therefore, a system in contact with one common bath that is prepared in the singlet state will never show any decoherence effects. The singlet state is a protected (decoherence free) subspace (DFS) [37]. Obviously ‘‘half’’ a decoherence free qubit is not very useful, but one could imagine to increase the number of qubits (easy especially in solid state systems) to receive a bigger DFS [38]. And it should be

noted that deviations from the ideal case of exactly same qubit parameters for both qubits (needed here to get a DFS) enter the theory of DFS's only in second order [39]. Therefore, scaling up the system to more qubits and taking advantage of the properties of DFS's seems very promising.

2.4 Eigenenergies and eigenstates of the two-qubit Hamiltonian

Eigenvalues and eigenvectors of the unperturbed two-qubit system Hamiltonian are needed to apply Bloch-Redfield theory. The matrix shape of (2.10) is very inconvenient, if one tries to diagonalize this Hamiltonian. For the sake of simplicity (and when regarding DFS's without

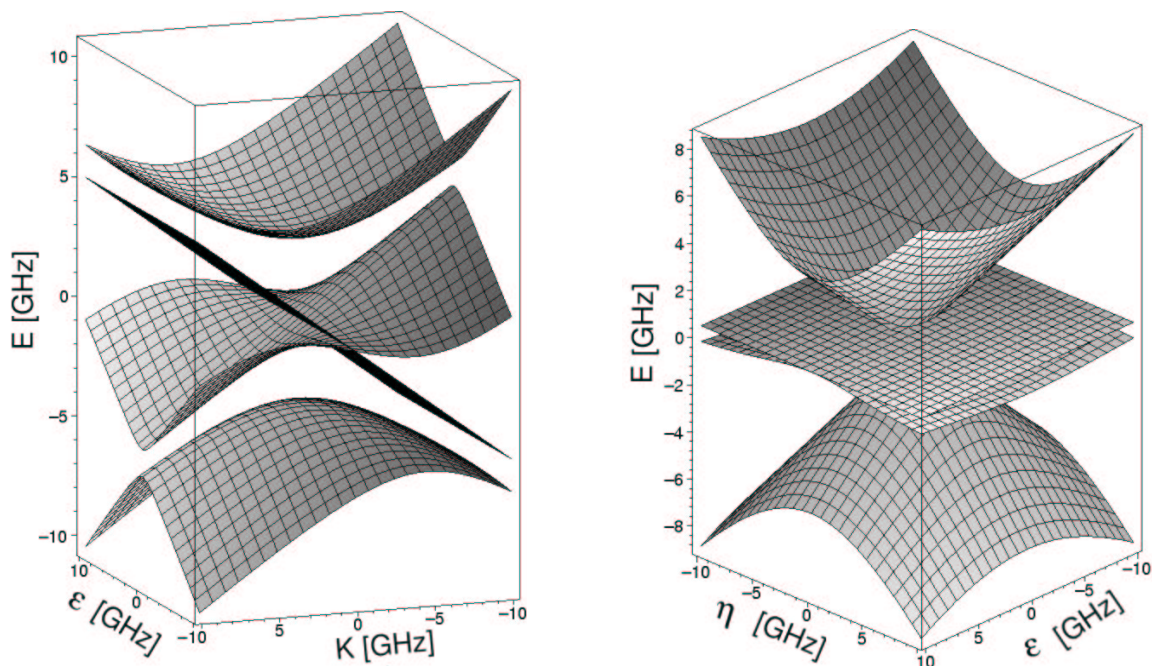


Figure 2.5: Energy spectrum of the coupled two-qubit system. Here the analytical results calculated in appendix A are plotted. In the left plot $\eta = 5$ GHz, ϵ and K are varied. Usually for superconducting flux qubits $\epsilon > \eta$ is assumed [32]. The right plot depicts the eigenenergies for K fixed to 1 GHz, ϵ and η are varied.

loss of generality) we assume two qubits with equal qubit parameters. Thus the Hamiltonian (2.10) is modified to become

$$\mathbf{H}_{2qb} = -\frac{1}{2} \begin{pmatrix} \epsilon + K & \eta & 0 & 0 \\ \eta & -K & \eta & 0 \\ 0 & \eta & K - \epsilon & 0 \\ 0 & 0 & 0 & -K \end{pmatrix}. \quad (2.14)$$

The Hamiltonian (2.14) is diagonalized exactly in appendix A and an analytic result for the eigenenergies and eigenstates of the two qubit system is given. In the following, $|E1\rangle$, $|E2\rangle$,

$|E3\rangle$ and $|E4\rangle$ denote the eigenstates of the two-qubit system.

The eigenenergies of the unperturbed Hamiltonian (2.14) depend on the three parameters K , ϵ and η . For an overview we visualize the energy landscape in the 3D plots of figure 2.5. In figure 2.5 either η (left plot) or K (right plot) is fixed. From the left plot one observes clearly, that the singlet crosses a triplet state indicating that the singlet does not interact with triplet states as was already found from the above analysis of the two qubit Hamiltonian. In the left panel K is tuned from large positive to large negative values corresponding to large ferromagnetic coupling and large anti-ferromagnetic coupling respectively. For several parameter sets, which will be discussed in the following, chapters figure 2.6 displays the eigenenergies in more detail.

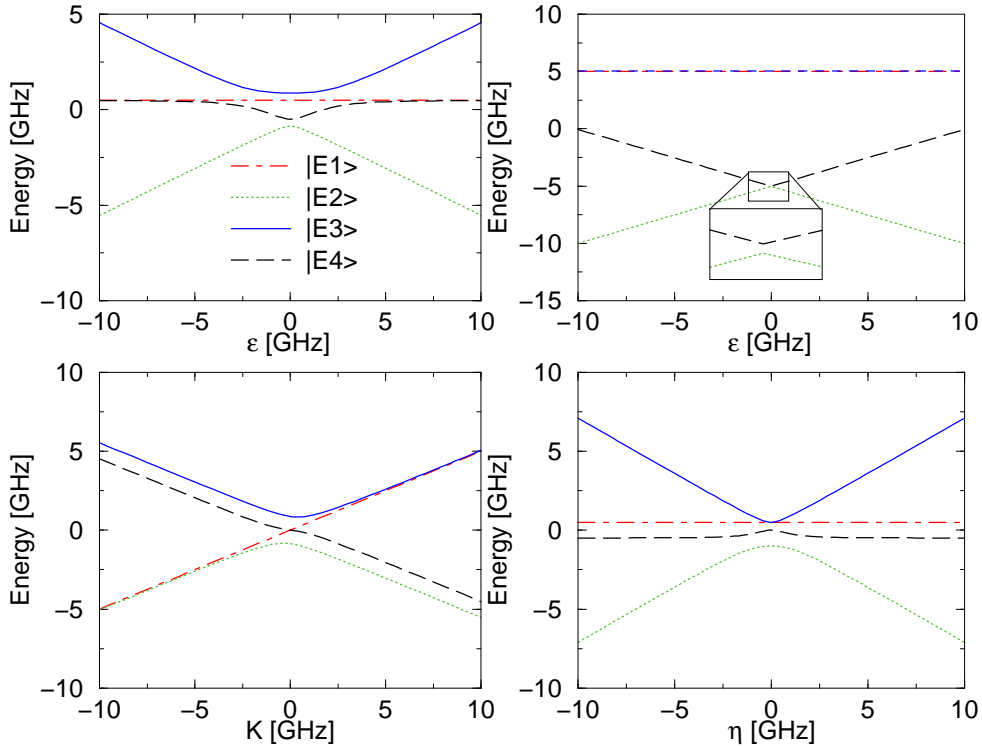


Figure 2.6: Plot of the eigenenergies of the eigenstates $|E1\rangle$, $|E2\rangle$, $|E3\rangle$ and $|E4\rangle$. From upper left to lower right: 1) $K = 1$ GHz, $\eta = 1$ GHz and ϵ is varied, 2) $K = 10$ GHz, $\eta = 1$ GHz and ϵ is varied; the inset resolves the avoided level crossing due to the finite transmission amplitude η , 3) $\eta = 1$ GHz, $\epsilon = 1$ GHz and K is varied, 4) $K = 1$ GHz, $\epsilon = 1$ GHz and η is varied.

The energies that are chosen for the parameters ϵ , η and K in figure 2.6 are all in the typical energy range of a few GHz resembling the parameters of known single- and two-qubit experiments in Delft [13] and at MIT. Panel 1) shows that for large values of ϵ two of the eigenenergies are degenerate (namely for $\epsilon \gg \eta, K$ the states $|E1\rangle$ and $|E4\rangle$ equal $(1/\sqrt{2})(|\uparrow\downarrow\uparrow\downarrow\rangle - |\uparrow\downarrow\downarrow\uparrow\rangle)$ and $(1/\sqrt{2})(|\uparrow\downarrow\uparrow\downarrow\rangle + |\uparrow\downarrow\downarrow\uparrow\rangle)$, hence the eigenenergies are degenerate)

while near zero energy bias (magnetic frustration $f = 1/2$) all four eigenenergies might be observed. Note also that therefore at zero energy bias the transition frequency $\omega_{14} = -\omega_{41}$ has a local maximum.

If K is set to a big positive value corresponding to large ferromagnetic coupling (figure 2.6, panel 2), $K = 10$ GHz) the Hamiltonian (2.14) is nearly diagonal and hence the eigenstates in good approximation are equal to the singlet/triplet basis states. In this case $|E3\rangle$ equals the triplet state $(1/\sqrt{2})(|\uparrow\uparrow\downarrow\rangle + |\uparrow\downarrow\uparrow\rangle)$, $|E2\rangle$ and $|E4\rangle$ equal $|\uparrow\downarrow\downarrow\rangle$ and $|\downarrow\uparrow\downarrow\rangle$ respectively for positive values of ϵ . For large negative values of ϵ the two states $|E2\rangle$ and $|E4\rangle$ become equal $|\downarrow\downarrow\uparrow\rangle$ and $|\downarrow\uparrow\uparrow\rangle$ with a spin-flip at $\epsilon = 0$. In the case of large ferromagnetic coupling the ground state tends towards the superposition $(1/\sqrt{2})(|\uparrow\downarrow\downarrow\rangle + |\downarrow\uparrow\downarrow\rangle)$. Of course panel 2) shows that only for ϵ equal to zero both $|E2\rangle = |\uparrow\downarrow\downarrow\rangle$ ($|E2\rangle = |\downarrow\uparrow\downarrow\rangle$ for negative ϵ) and $|E4\rangle = |\downarrow\uparrow\downarrow\rangle$ ($|E4\rangle = |\uparrow\downarrow\downarrow\rangle$ for negative ϵ) have the same energies (which one would expect if the $-(1/2)K\sigma_z^{(1)}\sigma_z^{(2)}$ term in the Hamiltonian dominates) because if ϵ is increased the $\epsilon_i\hat{\sigma}_z^{(i)}$ ($i=1,2$) terms in the Hamiltonian change the energy.

For negative K and $|K| \gg \epsilon, \Delta$ and hence large antiferromagnetic coupling, the states $|\downarrow\uparrow\downarrow\rangle$ and $|\uparrow\downarrow\downarrow\rangle$ are emphasized. In this case, the ground state tends towards $(1/\sqrt{2})(|\downarrow\uparrow\downarrow\rangle + |\uparrow\downarrow\downarrow\rangle)$. The energies of $(1/\sqrt{2})(|\downarrow\uparrow\downarrow\rangle + |\uparrow\downarrow\downarrow\rangle)$ and $(1/\sqrt{2})(|\downarrow\uparrow\downarrow\rangle - |\uparrow\downarrow\downarrow\rangle)$ are the same, independent of the value of ϵ . If ϵ and η are kept constant and K is negative with $|K| \gg \epsilon, \Delta$ (antiferromagnetic coupling, large positive K describes ferromagnetic coupling) the singlet state and the triplet state $(1/\sqrt{2})(|\uparrow\uparrow\downarrow\rangle + |\uparrow\downarrow\uparrow\rangle)$ are indistinguishable having the same energies. From figure 2.6, panel 3), one directly sees (the singlet eigenenergy crosses the triplet eigenenergies) that regarding only (2.14) (no dissipative environment) the singlet does not interact with any triplet states. At zero energy bias (magnetic frustration $f = 1/2$) none of the eigenstates equal one of the triplet states (e.g. as observed for a large energy bias ϵ). This means that at zero energy bias ϵ three eigenstates (one eigenstate always equals the singlet) are superpositions of triplet states. This is elucidated further in the next paragraph. The inset of panel 2) depicts the level anti-crossing between the eigenenergies of the two states $|E2\rangle$ and $|E4\rangle$ due to quantum tunneling.

Figure 2.7 shows which singlet/triplet states the eigenstates consist of, for different qubit parameters. The first eigenstate $|E1\rangle = (1/\sqrt{2})(|10\rangle - |01\rangle)$ for all times while the other eigenstates $|E2\rangle$, $|E3\rangle$ and $|E4\rangle$ are in general superpositions of the singlet/triplet basis states. For large values of $|\epsilon|$ the eigenstates approach the singlet/triplet basis states. Especially at typical working points, where $\epsilon \approx 5 \cdot \Delta$ [32] the eigenstates already nearly equal the singlet/triplet basis states. However in figure 2.7 the inter-qubit coupling strength K is fixed to a rather high value of 1 GHz. (Usually a value of $K \approx 0.5 \cdot \Delta$ is assumed [24].) This rather high value of K accounts for faster convergence towards the singlet/triplet basis states when $|\epsilon|$ is increased.

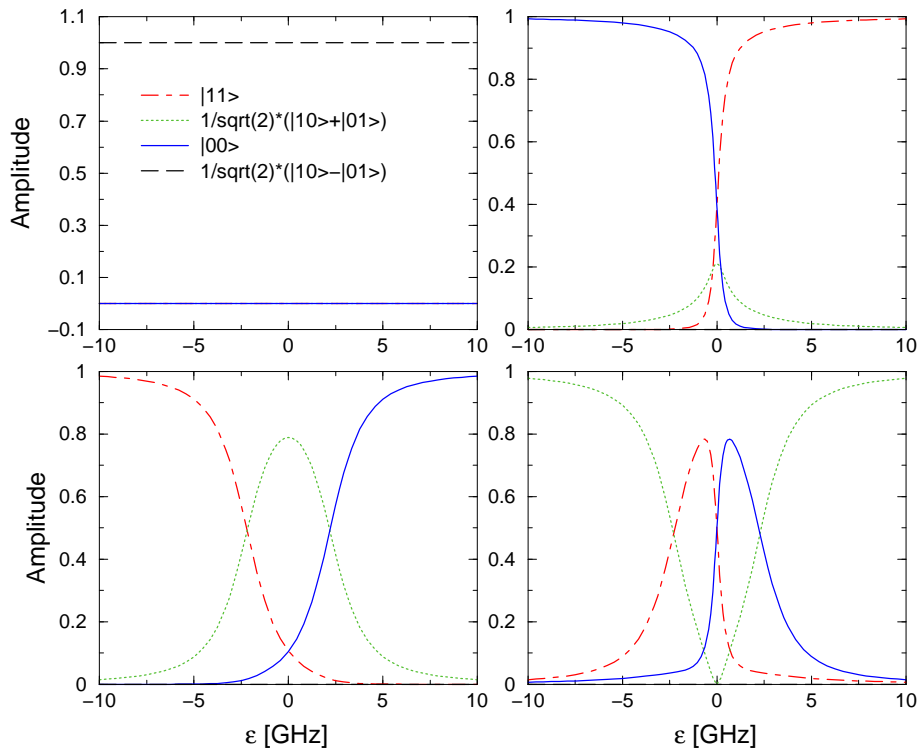


Figure 2.7: Plot of the amplitude of the different singlet/triplet states of which the eigenstates denoted by $|E1\rangle$, $|E2\rangle$, $|E3\rangle$ and $|E4\rangle$ are composed for the four eigenstates. In all plots ϵ is varied and K and η are fixed to 1 GHz.

Chapter 3

Weak symmetric driving in ϵ

To make quantitative predictions that might be compared with experimental results on the spectroscopy of coupled qubits, we consider the case of weak symmetric driving in the energy bias ϵ . We calculate the transitions induced by small perturbations of ϵ using the Hamiltonian (2.10) which describes two coupled flux qubits. Experiments investigating two directly inductively coupled flux qubits are currently done in Delft [40]. We assume a small time dependent periodic perturbation $\kappa(t)$ of ϵ in the Hamiltonian (here given in singlet/triplet basis representation)

$$\mathbf{H}_{op} = -\frac{1}{2} \begin{pmatrix} [\epsilon + \kappa(t)] + K & \eta & 0 & -\Delta\eta \\ \eta & -K & \eta & \Delta\epsilon \\ 0 & \eta & K - [\epsilon + \kappa(t)] & \Delta\eta \\ -\Delta\eta & \Delta\epsilon & \Delta\eta & -K \end{pmatrix}, \quad (3.1)$$

which in the case of two identical qubits (all terms including $\Delta\epsilon$ and $\Delta\eta$ vanish) has the form

$$\mathbf{H}_{op} = -\frac{1}{2} \begin{pmatrix} \epsilon + K & \eta & 0 & 0 \\ \eta & -K & \eta & 0 \\ 0 & \eta & K - \epsilon & 0 \\ 0 & 0 & 0 & -K \end{pmatrix} - \frac{1}{2} \begin{pmatrix} \kappa(t) & 0 & 0 & 0 \\ 0 & 0 & 0 & 0 \\ 0 & 0 & -\kappa(t) & 0 \\ 0 & 0 & 0 & 0 \end{pmatrix}. \quad (3.2)$$

Here we identify the periodic perturbation as

$$\hat{V}(t) = -\frac{1}{2} \begin{pmatrix} \kappa(t) & 0 & 0 & 0 \\ 0 & 0 & 0 & 0 \\ 0 & 0 & -\kappa(t) & 0 \\ 0 & 0 & 0 & 0 \end{pmatrix}. \quad (3.3)$$

For a periodic perturbation we may rewrite $\hat{V}(t)$ as

$$\begin{aligned} \hat{V}(t) &= -\frac{1}{2} \begin{pmatrix} 1 & 0 & 0 & 0 \\ 0 & 0 & 0 & 0 \\ 0 & 0 & -1 & 0 \\ 0 & 0 & 0 & 0 \end{pmatrix} \kappa \exp(\pm i\omega t) \\ &= -\frac{1}{2} \hat{V}_0 \kappa \exp(\pm i\omega t) \end{aligned} \quad (3.4)$$

where κ is the amplitude and ω the frequency of the perturbation. In the eigenbasis of \mathbf{H}_{op} the matrix elements of \widehat{V}_0 read (the constants k_i , $i = 1, \dots, 9$, are defined in appendix A)

$$\langle 1|\widehat{V}_0|2\rangle = \langle 1|\widehat{V}_0|3\rangle = \langle 1|\widehat{V}_0|4\rangle = \langle 2|\widehat{V}_0|1\rangle = \langle 3|\widehat{V}_0|1\rangle = \langle 4|\widehat{V}_0|1\rangle = 0 \quad (3.5)$$

$$\langle 2|\widehat{V}_0|2\rangle = \frac{|\eta|^2}{k_3^2} (k_1^2 - k_2^2) \quad (3.6)$$

$$\langle 2|\widehat{V}_0|3\rangle = 3\frac{|\eta|^3|k_2|}{k_6k_3} \left(9\frac{k_1}{k_2} - \frac{k_5}{\eta^2}\right) \quad (3.7)$$

$$\langle 2|\widehat{V}_0|4\rangle = -3\frac{|\eta|^3|k_2|}{k_9k_3} \left(\frac{k_7k_1}{\eta^2k_2} + 9\right) \quad (3.8)$$

$$\langle 3|\widehat{V}_0|2\rangle = 3\frac{|\eta|^3|k_2|}{k_6k_3} \left(9\frac{k_1}{k_2} - \frac{k_5}{\eta^2}\right) \quad (3.9)$$

$$\langle 3|\widehat{V}_0|3\rangle = \frac{|\eta|^4}{k_6^2} \left(81 - \frac{k_5^2}{\eta^4}\right) \quad (3.10)$$

$$\langle 3|\widehat{V}_0|4\rangle = -9\frac{|\eta|^2}{k_6k_9} (k_7 + k_5) \quad (3.11)$$

$$\langle 4|\widehat{V}_0|2\rangle = -3\frac{|\eta|^3|k_2|}{k_9k_3} \left(\frac{k_7k_1}{\eta^2k_2} + 9\right) \quad (3.12)$$

$$\langle 4|\widehat{V}_0|3\rangle = -9\frac{|\eta|^2}{k_6k_9} (k_7 + k_5) \quad (3.13)$$

$$\langle 4|\widehat{V}_0|4\rangle = \frac{|\eta|^4}{k_9^2} \left(\frac{k_7^2}{\eta^4} - 81\right) \quad (3.14)$$

According to first order perturbation theory, the eigenenergies of the two-qubit system are modified

$$E'_i = E_i + \langle i|\widehat{V}(t)|i\rangle. \quad (3.15)$$

Due to the symmetry of the Hamiltonian, equation (3.2), which is respected by the driving there are still no transitions possible between the singlet state and the triplet states. To calculate the probability to find the system at time t in state $|m\rangle$ if it started in state $|n\rangle$ (with $m \neq n$; first order perturbation theory)

$$P_{mn} = |c_m^{(1)}(t)|^2 \quad (3.16)$$

we need to evaluate the coefficient [41]

$$c_m^{(1)}(t) = -\frac{i}{\hbar} \langle m|\widehat{V}_0|n\rangle \int_0^t dt' \exp(i\Omega t'), \quad (3.17)$$

with $\Omega = \omega_{mn} \pm \omega$, where ω denotes the frequency of the perturbation. The integral on the right hand side of (3.17) can easily be calculated

$$\left| \int_0^t dt' \exp(i\Omega t') \right|^2 = \left| \frac{\exp(i\Omega t) - 1}{i\Omega} \right|^2 = \frac{4 \sin^2(\Omega t/2)}{\Omega^2}. \quad (3.18)$$

Gathering all the previous results we get [41]

$$P_{nm} = |c_m^{(1)}(t)|^2 = \frac{1}{\hbar^2} |\langle m|\widehat{V}_0|n\rangle|^2 \frac{4 \sin^2(\Omega t/2)}{\Omega^2}. \quad (3.19)$$

From the matrix elements of \widehat{V}_0 and the plots in figure 3.1 one concludes that the perturbation does not induce transitions between the singlet and triplet states. And figure 3.1 shows that within the triplet the transitions $2 \rightarrow 4$ ($4 \rightarrow 2$) and $3 \rightarrow 4$ ($4 \rightarrow 3$) are favored compared to the transition $3 \rightarrow 2$ ($2 \rightarrow 3$) which is always suppressed.

In experiments with flux qubits usually the transition frequencies between certain energy levels are probed. Therefore, figures 3.2 and 3.3 depict the transition frequencies between the four eigenstates. The transition frequencies are defined as $\omega_{nm} = (E_n - E_m)/\hbar$. Note that $\omega_{nm} = -\omega_{mn}$. Here, we either fixed $K = 0.2$ GHz, $\eta = 0.2$ GHz and varied ϵ or fixed $K = 0.2$ GHz, $\epsilon = 1$ GHz and varied η . The transitions between the singlet state $|E1\rangle$ and the triplet states are forbidden in the case of one common bath, due to the special symmetries of the Hamiltonian (2.9). (The transition frequencies corresponding to transitions to and from the singlet states are $\omega_{21} = -\omega_{12}$, $\omega_{31} = -\omega_{13}$ and $\omega_{41} = -\omega_{14}$.) However, in the case of two distinct baths the environment can mediate transitions between the singlet state and the triplet states.

Not all transition frequencies have local minima at $\epsilon = 0$. The frequencies ω_{41} and ω_{34} have local maxima at zero bias ϵ . This, one can understand when looking at figure 2.6, panel 1), (despite the fact that there larger values of η and K have been used; the overall behaviour stays the same): the energy of the eigenstate $|E4\rangle$ has a local minimum at $\epsilon = 0$. Also the substructure of ω_{34} can be understood from figure 2.6: the frequency ω_{34} has a local maximum at $\epsilon = 0$, because of the local minimum of the eigenenergy of the state $|E4\rangle$. First, if ϵ is increased, the level spacing of $|E4\rangle$ and $|E3\rangle$ decreases. Then, for larger values of ϵ the level spacing of $|E4\rangle$ and $|E3\rangle$ increases again. Thus, the structure observed for ω_{34} around $\epsilon = 0$ emerges in figure 3.3.

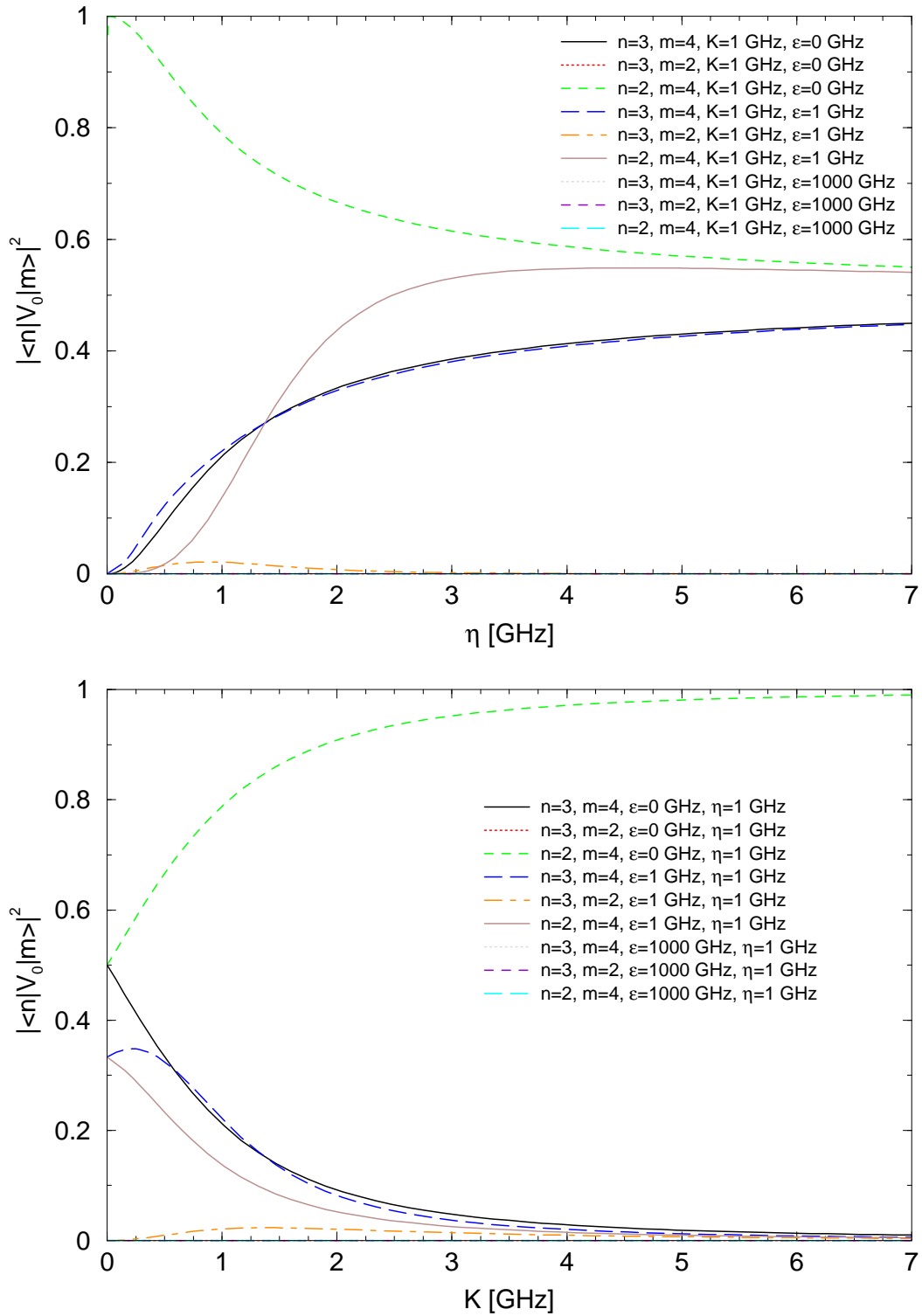


Figure 3.1: Plot of the squared absolute value of the matrix elements (3.5)-(3.14) for different values of K , ϵ , η . Parameters for the upper panel are $K = 1$ GHz, $\epsilon = 0, 1, 10^3$ GHz and for the lower panel $\eta = 1$ GHz, $\epsilon = 0, 1, 10^3$ GHz.

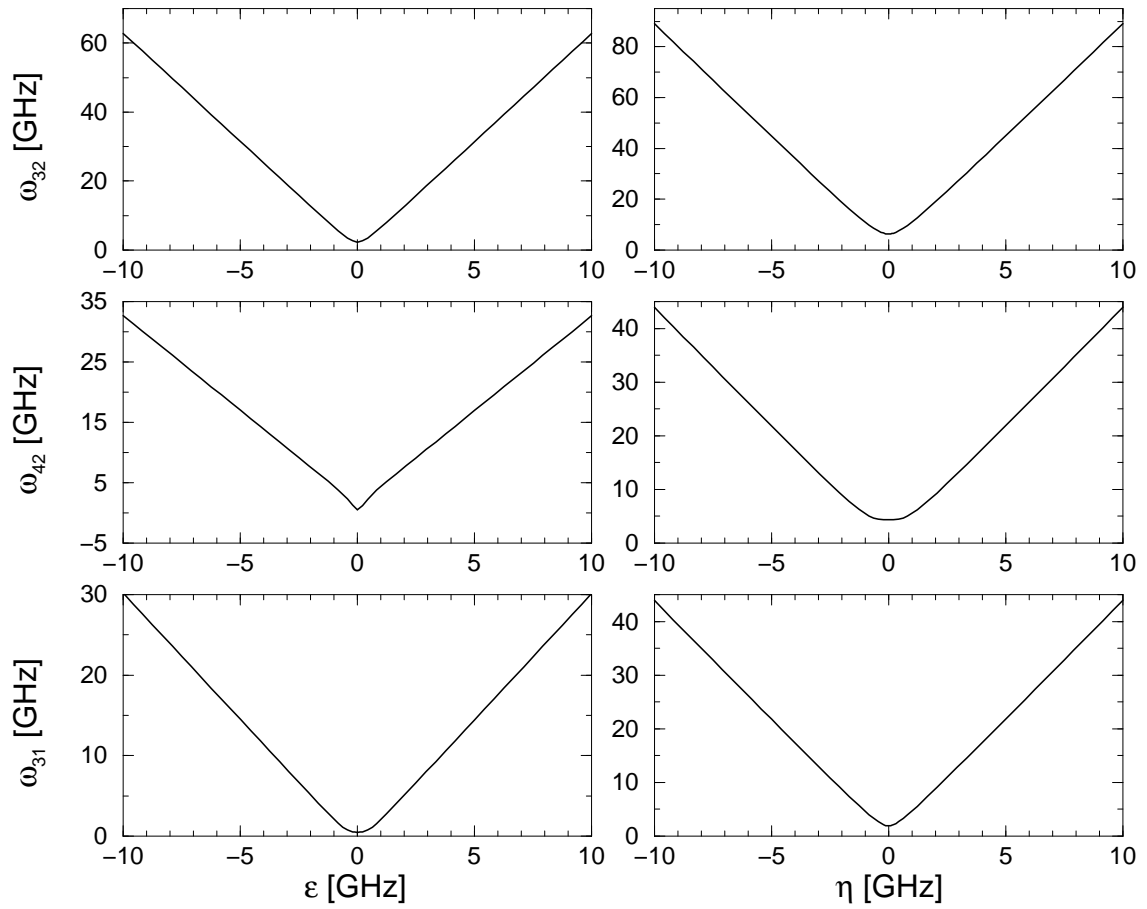


Figure 3.2: Plot of the transition frequencies ω_{32} , ω_{42} and ω_{31} . In the left column $K = 0.2$ GHz, $\eta = 0.2$ GHz and ϵ is varied. Right column $K = 0.2$ GHz, $\epsilon = 1$ GHz and η is varied.

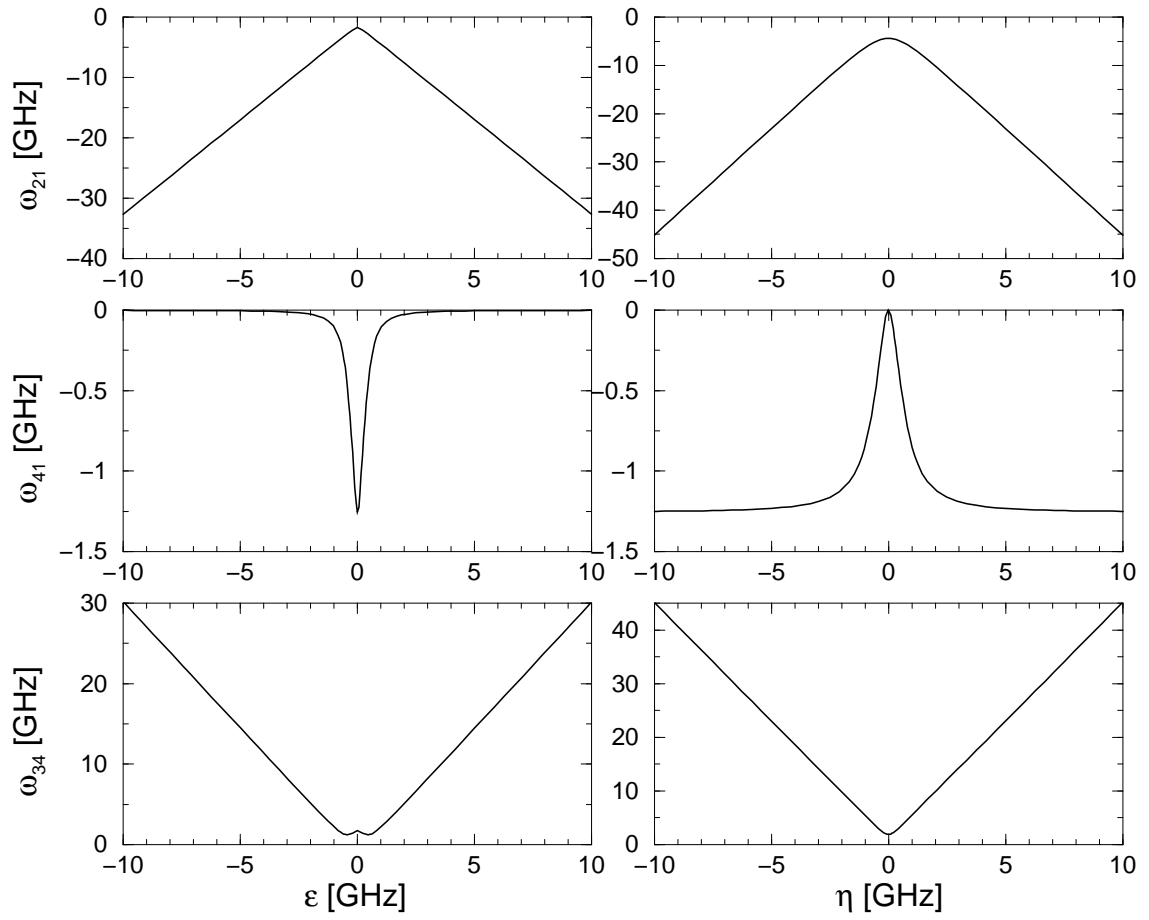


Figure 3.3: Plot of the transition frequencies ω_{21} , ω_{41} and ω_{34} . In the left column $K = 0.2$ GHz, $\eta = 0.2$ GHz and ϵ is varied. Right column $K = 0.2$ GHz, $\epsilon = 1$ GHz and η is varied.

Chapter 4

Bloch-Redfield-Formalism

The so called Bloch-Redfield-Formalism provides an important tool for finding a set of coupled master equations which describes the dynamics of the reduced (i.e. the reservoir coordinates are traced out) density matrix for a given system in contact with a dissipative environment. As we discussed in chapter 2, we model the dissipative (bosonic) environment as either a common bath or two distinct baths of harmonic oscillators coupling to the $\hat{\sigma}_z$ -components of the two qubits. The Hamiltonian of our two qubit system including the bath of harmonic oscillators, the coupling to the bath and a driving field reads [21]

$$\mathbf{H}_{op}(t) = \mathbf{H}_{2qb} + \mathbf{H}_B + \mathbf{H}_{int} + \mathbf{H}_1(t), \quad (4.1)$$

where $\mathbf{H}_1(t)$ is the interaction energy with a weak driving field, \mathbf{H}_B a bath of harmonic oscillators and \mathbf{H}_{int} inherits the coupling to a dissipative environment. In our case the effects of driving are not investigated. The Liouville equation for the density operator ρ_T of the whole system is

$$i\hbar \frac{d}{dt} \rho_T(t) = [\mathbf{H}_{op}(t), \rho_T(t)]. \quad (4.2)$$

Then Bloch-Redfield formalism is derived from a projector approach. It bestows an equation of motion for the reduced density matrix by separating the density operator into two parts, the part we are interested in and the remainder. Then a set of coupled master equations is derived [21]. The Bloch-Redfield approach is valid for a weak coupling to the environment. In Born approximation it provides the following set of equations for the reduced density matrix ρ describing the dynamics of the system [22, 42]

$$\dot{\rho}_{nm}(t) = -i\omega_{nm}\rho_{nm}(t) - \sum_{kl} R_{nmkl}\rho_{kl}(t), \quad (4.3)$$

where $\omega_{nm} = (E_n - E_m)/\hbar$, and $\max_{n,m,k,\ell} |\text{Re}(R_{nmkl})| < \min_{n \neq m} |\omega_{nm}|$ must hold. The tensor R_{nmkl} is called Redfield relaxation tensor and comprises the dissipative effects of the coupling of the system to the environment.

4.1 Redfield relaxation tensor

The elements of the Redfield relaxation tensor read [42]

$$R_{nmkl} = \delta_{\ell m} \sum_r \Gamma_{nrrk}^{(+)} + \delta_{nk} \sum_r \Gamma_{\ell rrm}^{(-)} - \Gamma_{\ell mnk}^{(+)} - \Gamma_{\ell mnk}^{(-)}. \quad (4.4)$$

The rates are given by the Golden Rule expressions

$$\Gamma_{\ell mnk}^{(+)} = \hbar^{-2} \int_0^\infty dt e^{-i\omega_{nk}t} \langle \tilde{H}_{I,\ell m}(t) \tilde{H}_{I,nk}(0) \rangle, \quad (4.5)$$

$$\Gamma_{\ell mnk}^{(-)} = \hbar^{-2} \int_0^\infty dt e^{-i\omega_{\ell m}t} \langle \tilde{H}_{I,\ell m}(0) \tilde{H}_{I,nk}(t) \rangle. \quad (4.6)$$

Where $\tilde{H}_I(t) = \exp(iH_B t/\hbar) H_I \exp(-iH_B t/\hbar)$ denotes the interaction in the interaction picture, and the bracket denotes thermal average of the bath degrees of freedom. One can recognize that the Bloch-Redfield approach leads to equations of Markovian shape. However, by the time integrals in (4.5) and (4.6) we take account of the bath correlations.

4.2 Two qubits coupled to two distinct baths

We evaluate the expressions (4.5) and (4.6) in the case of two qubits, each coupled to a distinct bath. The coupling to the bath is described by the coupling term $\sigma_z^{(i)} \otimes \hat{X}^{(i)}$, where $\hat{X} = \zeta \sum_\nu \lambda_\nu x_\nu$ is the coordinate of the bath of harmonic oscillators. First we evaluate (4.5). The calculation is done in more detail in appendix C. Writing down the coupling to the bath as the interaction in the interaction picture and inserting this expression into (4.5) gives

$$\begin{aligned} \Gamma_{\ell mnk}^{(+)} &= \hbar^{-2} \int_0^\infty dt e^{-i\omega_{nk}t} \langle e^{i(H_{B_1} + H_{B_2})t/\hbar} \times \\ &\quad \times \left(\sigma_{z,\ell m}^{(1)} \otimes \sum_i \lambda_i x_i^{(1)} + \sigma_{z,\ell m}^{(2)} \otimes \sum_j \mu_j x_j^{(2)} \right) e^{-i(H_{B_1} + H_{B_2})t/\hbar} \times \\ &\quad \times \left(\sigma_{z,nk}^{(1)} \otimes \sum_\alpha \lambda_\alpha x_\alpha^{(1)} + \sigma_{z,nk}^{(2)} \otimes \sum_\beta \mu_\beta x_\beta^{(2)} \right) \rangle, \end{aligned} \quad (4.7)$$

where $\sigma_{z,nm}^{(i)}$ ($i = 1, 2$) are the matrix elements of $\hat{\sigma}_z^{(i)}$ with respect to the eigenbasis of the unperturbed Hamiltonian (2.14). The explicit shape of the matrix elements $\sigma_{z,nm}^{(i)}$ is given in appendix B. We assume ohmic spectral densities with a Drude-cutoff. This is a realistic assumption [13] and leads to integrals in the rates which are tractable by the residue theorem (see for example chapter 4.6). The cutoff frequency ω_c for the spectral functions of the two qubits should be the largest frequency in the problem, this is discussed further in chapter 4.6

$$J_1(\omega) = \frac{\alpha_1 \hbar \omega}{1 + \frac{\omega^2}{\omega_c^2}} \quad \text{and} \quad J_2(\omega) = \frac{\alpha_2 \hbar \omega}{1 + \frac{\omega^2}{\omega_c^2}}. \quad (4.8)$$

The dimensionless parameter α describes the strength of the dissipative effects that enter the Hamiltonian via the coupling to the environment, described by s and Δs . After tracing out over the bath degrees of freedom (explicitly calculated in appendix B1), the rates read

$$\begin{aligned} \Gamma_{\ell mnk}^{(+)} &= \frac{1}{8\hbar} \left[\sigma_{z,\ell m}^{(1)} \sigma_{z,nk}^{(1)} J_1(\omega_{nk}) + \sigma_{z,\ell m}^{(2)} \sigma_{z,nk}^{(2)} J_2(\omega_{nk}) \right] (\coth(\beta \hbar \omega_{nk}/2) - 1) + \\ &\quad + \frac{i}{4\pi \hbar} \left[\sigma_{z,\ell m}^{(2)} \sigma_{z,nk}^{(2)} \int_0^\infty d\omega \frac{J_2(\omega)}{\omega^2 - \omega_{nk}^2} (\coth(\beta \hbar \omega/2) \omega_{nk} - \omega) + \right. \\ &\quad \left. + \sigma_{z,\ell m}^{(1)} \sigma_{z,nk}^{(1)} \int_0^\infty d\omega \frac{J_1(\omega)}{\omega^2 - \omega_{nk}^2} (\coth(\beta \hbar \omega/2) \omega_{nk} - \omega) \right] \end{aligned} \quad (4.9)$$

and

$$\begin{aligned}
\Gamma_{\ell mnk}^{(-)} &= \frac{1}{8\hbar} \left[\sigma_{z,\ell m}^{(1)} \sigma_{z,nk}^{(1)} J_1(\omega_{\ell m}) + \sigma_{z,\ell m}^{(2)} \sigma_{z,nk}^{(2)} J_2(\omega_{\ell m}) \right] (\coth(\beta\hbar\omega_{\ell m}/2) + 1) + \\
&+ \frac{i}{4\pi\hbar} \left[\sigma_{z,\ell m}^{(2)} \sigma_{z,nk}^{(2)} \int_0^\infty d\omega \frac{J_2(\omega)}{\omega^2 - \omega_{\ell m}^2} (\coth(\beta\hbar\omega/2)\omega_{\ell m} + \omega) + \right. \\
&\left. + \sigma_{z,\ell m}^{(1)} \sigma_{z,nk}^{(1)} \int_0^\infty d\omega \frac{J_1(\omega)}{\omega^2 - \omega_{\ell m}^2} (\coth(\beta\hbar\omega/2)\omega_{\ell m} + \omega) \right]. \tag{4.10}
\end{aligned}$$

The rates $\Gamma_{\ell mnk}^{(+)}$ and $\Gamma_{\ell mnk}^{(-)}$ might be inserted into (4.4) to build the Redfield tensor. Note here that for $\omega_{nk} \rightarrow 0$ and $\omega_{\ell m} \rightarrow 0$ respectively the real part of the rates (which is responsible for relaxation and dephasing) is of value

$$\Gamma_{\ell mnk}^{(+)} = \Gamma_{\ell mnk}^{(-)} = \frac{1}{4\beta\hbar} \left[\sigma_{z,\ell m}^{(1)} \sigma_{z,nk}^{(1)} \alpha_1 + \sigma_{z,\ell m}^{(2)} \sigma_{z,nk}^{(2)} \alpha_2 \right] \tag{4.11}$$

as evaluated in appendix C. To solve the set of differential equations (4.3), it is convenient not to use the superoperator notation were $\rho(t_{op}) = \nu_{op}\rho(0)$ but either write ρ as a vector. In general the Redfield equations (4.3) without driving are solved by an ansatz of the type $\rho(t) = B \exp(\tilde{R}_i) B^{-1} \rho(0)$, where \tilde{R}_i is a diagonal matrix. The entries of this diagonal matrix are the eigenvalues of the Redfield tensor (4.4), written in matrix form, including the contribution from the term $i\omega_{nm}$ (cf. equation 4.3). Here, the reduced density matrix $\rho = (\rho_{11}, \dots, \rho_{44})^T$ is written as a vector. The matrix B describes the basis change to the eigenbasis of \tilde{R}_i , in which \tilde{R}_i has diagonal shape.

4.3 Two qubits coupled to one common bath

For the case of two qubits coupled to one common bath we perform the same calculation as in the last section, which leads to expressions for the rates

$$\begin{aligned}
\Gamma_{\ell mnk}^{(+)} &= \frac{1}{8\hbar} \left[\sigma_{z,\ell m}^{(1)} \sigma_{z,nk}^{(1)} + \sigma_{z,\ell m}^{(1)} \sigma_{z,nk}^{(2)} + \sigma_{z,\ell m}^{(2)} \sigma_{z,nk}^{(1)} + \sigma_{z,\ell m}^{(2)} \sigma_{z,nk}^{(2)} \right] J(\omega_{nk}) \times \\
&\times (\coth(\beta\hbar\omega_{nk}/2) - 1) + \frac{i}{4\pi\hbar} \left[\sigma_{z,\ell m}^{(1)} \sigma_{z,nk}^{(1)} + \sigma_{z,\ell m}^{(1)} \sigma_{z,nk}^{(2)} + \right. \\
&\left. + \sigma_{z,\ell m}^{(2)} \sigma_{z,nk}^{(1)} + \sigma_{z,\ell m}^{(2)} \sigma_{z,nk}^{(2)} \right] \int_0^\infty d\omega \frac{J(\omega)}{\omega^2 - \omega_{nk}^2} (\coth(\beta\hbar\omega/2)\omega_{nk} - \omega) \tag{4.12}
\end{aligned}$$

and

$$\begin{aligned}
\Gamma_{\ell mnk}^{(-)} &= \frac{1}{8\hbar} \left[\sigma_{z,\ell m}^{(1)} \sigma_{z,nk}^{(1)} + \sigma_{z,\ell m}^{(1)} \sigma_{z,nk}^{(2)} + \sigma_{z,\ell m}^{(2)} \sigma_{z,nk}^{(1)} + \sigma_{z,\ell m}^{(2)} \sigma_{z,nk}^{(2)} \right] J(\omega_{\ell m}) \times \\
&\times (\coth(\beta\hbar\omega_{\ell m}/2) + 1) + \frac{i}{4\pi\hbar} \left[\sigma_{z,\ell m}^{(1)} \sigma_{z,nk}^{(1)} + \sigma_{z,\ell m}^{(1)} \sigma_{z,nk}^{(2)} + \right. \\
&\left. + \sigma_{z,\ell m}^{(2)} \sigma_{z,nk}^{(1)} + \sigma_{z,\ell m}^{(2)} \sigma_{z,nk}^{(2)} \right] \int_0^\infty d\omega \frac{J(\omega)}{\omega^2 - \omega_{\ell m}^2} (\coth(\beta\hbar\omega/2)\omega_{\ell m} + \omega). \tag{4.13}
\end{aligned}$$

The difference between the rates for the case of two distinct baths (4.9), (4.10) are the two extra terms $\sigma_{z,lm}^{(1)}\sigma_{z,nk}^{(2)}$ and $\sigma_{z,lm}^{(2)}\sigma_{z,nk}^{(1)}$. They originate from the process of tracing out over the bath, because in the case of one common bath all creation and annihilation operators (harmonic oscillator coordinate \hat{X} written in terms of creation and annihilation operators) in the interaction Hamiltonian $\mathbf{H}_{int} \propto \hat{\sigma}_z^i \otimes \hat{X}$ ($i=1,2$) act on the same bath and therefore also the mixed terms $a^{(1)\dagger}a^{(2)}$ and $a^{(2)\dagger}a^{(1)}$ contribute to the rates. In the case of one common bath there is only one spectral function $J(\omega) = (\alpha\hbar\omega)/(1 + \frac{\omega^2}{\omega_c^2})$ which we also assume to be ohmic. For $\omega_{nk} \rightarrow 0$ and $\omega_{lm} \rightarrow 0$ respectively the real part of the rates is of the value

$$\Gamma_{\ell mnk}^{(+)} = \Gamma_{\ell mnk}^{(-)} = \frac{\alpha}{4\beta\hbar} \left[\sigma_{z,\ell m}^{(1)}\sigma_{z,nk}^{(1)} + \sigma_{z,\ell m}^{(1)}\sigma_{z,nk}^{(2)} + \sigma_{z,\ell m}^{(2)}\sigma_{z,nk}^{(1)} + \sigma_{z,\ell m}^{(2)}\sigma_{z,nk}^{(2)} \right]. \quad (4.14)$$

4.4 Dynamics of dissipative coupled flux qubits

The dissipative effects affecting the two qubit system lead to decoherence. The system relaxes due to energy relaxation on a timescale $\tau_R = \Gamma_R^{-1}$ (Γ_R is the sum of the relaxation rates for the four diagonal elements), called relaxation time, into a thermal mixture of the system's energy eigenstates. Therefore the diagonal elements of the reduced density matrix decay to the factors given by the Boltzmann factors. The quantum coherent dynamics of the system are superimposed on the relaxation and decay on a shorter time scale $\tau_{\varphi_{ij}} = \Gamma_{\varphi_{ij}}^{-1}$ ($i, j = 1, \dots, 4; i \neq j$) termed dephasing time. Thus dephasing causes the off diagonal terms (coherences) of the reduced density matrix to tend towards zero.

First, we investigate the relaxation of the two qubit system which was prepared in an eigenstate. If the system is prepared in an eigenstate, no phase coherence and thus no dephasing is present. In thermal equilibrium we receive $\rho = (1/Z)e^{-\beta H}$. Special cases are $T = 0$ K where ρ equals the projector on the ground state and $T \rightarrow \infty$ where we receive an equal distribution of all basis states. Figure 4.1 and 4.2 illustrate the relaxation of the system prepared in one of the four eigenstates for temperatures $T = 0$ K and $T = 100$ mK respectively. The qubit energies K , ϵ and η are all set to 1 GHz and α is set to $\alpha = 10^{-3}$. From figure 2.6 one recognizes that the eigenstate $|E2\rangle$ is the ground state for this set of parameters.

At low temperatures ($T = 0$ K), we observe that for the case of two distinct uncorrelated baths a system prepared in one of the four eigenstates always relaxes into the ground state. Of course in the case of two qubits coupling to one common bath the singlet is a protected subspace and there never will be any transitions between the eigenstate $|E1\rangle$ (singlet) and the eigenstates $|E2\rangle$, $|E3\rangle$ and $|E4\rangle$. Thus the cases of one common and two distinct baths show the same behaviour, the only difference is that a system prepared in the singlet eigenstate $|E1\rangle$ will not show any transitions in the case of one common bath. This is nicely observed in figures 4.1 and 4.2. Relaxation to the ground state happens by populating intermediate eigenstates with a lower energy than the initial state the system was prepared in at $t = 0$ s (cf. figure 2.6).

For high temperatures ($T \approx 10$ K) the system thermalizes into thermal equilibrium, where all four eigenstates have equal occupation probabilities. However, in the case of one common bath thermalization of the singlet state again is impeded because no transitions between the singlet and triplet states are possible, as one can see from the Hamiltonian (2.13). Therefore, in the case of both qubits coupling to one common bath the three eigenstates $|E2\rangle$, $|E3\rangle$ and

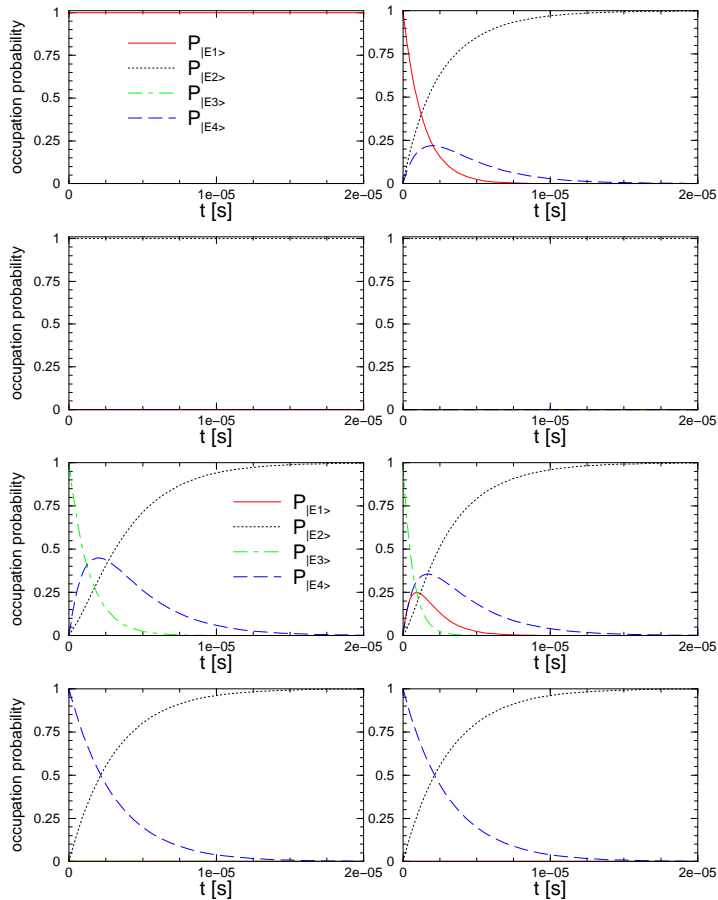


Figure 4.1: Plot of the occupation probability of the four eigenstates $|E1\rangle$, $|E2\rangle$, $|E3\rangle$ and $|E4\rangle$ for initially starting in one of the eigenstates at $T = 0$ K. The left column illustrates the case of two qubits coupling to one common bath and the right column the case of two qubits coupling to two distinct baths. The energies K , ϵ and η are all fixed to 1 GHz.

$|E4\rangle$ have equal occupation probabilities of $1/3$ after the relaxation time.

Figure 4.3 displays the dynamics of the system of two qubits prepared in an off-diagonal pure state, namely $|11\rangle = |\uparrow\uparrow\rangle = 0 \cdot |E1\rangle + 0.94 \cdot |E2\rangle + 0.22 \cdot |E3\rangle - 0.27 \cdot |E4\rangle$ at time $t = 0$ s ($\epsilon = \eta = K = 1$ GHz). Temperature is set to $T = 0$ K. In figure 4.3 the left column displays the case where $\alpha = 10^{-2}$ (the time scale on which decoherence happens is $t \approx 2 \cdot 10^{-7}$ s for this choice of parameters), while the right column illustrates the case where $\alpha = 10^{-3}$. For the latter case the dissipative effects are smaller. The occupation probability shows coherent oscillations which are damped due to dephasing and finally, at $T \approx 0$ K, the system relaxes into the ground state of the system. Here the superposition of basis states, in which the system was prepared, did not contain the singlet state. For low temperatures the timescale on which dephasing and relaxation happen is somewhat shorter for the case of one common bath (approximately $1.5 \cdot 10^{-7}$ s compared to $2 \cdot 10^{-7}$ s for $\alpha = 10^{-2}$). This can be explained by observing the temperature dependence of the rates shown in figure 4.5. Though for the case

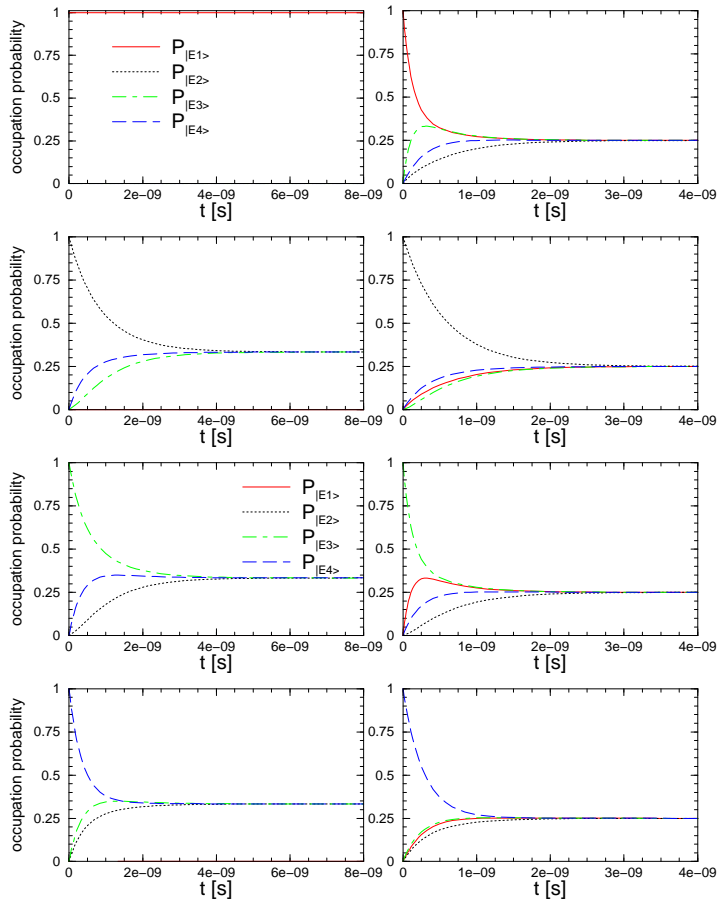


Figure 4.2: Plot of the occupation probability of the four eigenstates $|E1\rangle$, $|E2\rangle$, $|E3\rangle$ and $|E4\rangle$ for initially starting in one of the eigenstates at $T = 100$ mK. The left column illustrates the case of two qubits coupling to one common bath and the right column the case of two qubits coupling to two distinct baths. The energies K , ϵ and η are all fixed to 1 GHz.

of one common bath two of the dephasing rates are zero at $T = 0$ K, the remaining rates are always slightly bigger for the case of one common bath compared to the case of two distinct baths. If the system is prepared in a superposition of three of the eigenstates, namely $|E2\rangle$, $|E3\rangle$ and $|E4\rangle$, nearly all rates become important thus compensating the effect of the two rates which are approximately zero at zero temperature and leading to faster decoherence. If α and therefore the strength of the dissipative effects is increased from $\alpha = 10^{-3}$ to $\alpha = 10^{-2}$ (left plot in 4.3) the observed coherent motion is significantly damped. Variation of α leads to a phase shift of the coherent oscillations, due to renormalization of the frequencies [16]. However, in our case the effects of renormalization are very small, as discussed in chapter 4.6, and can not be observed in our plots.

If the system is prepared in a superposition of eigenstates $|E3\rangle$ and $|E4\rangle$ which are neither protected subspaces (of course, only in the case of one common bath the singlet is a protected subspace) nor the ground state, we observe coherent oscillations between the eigen-

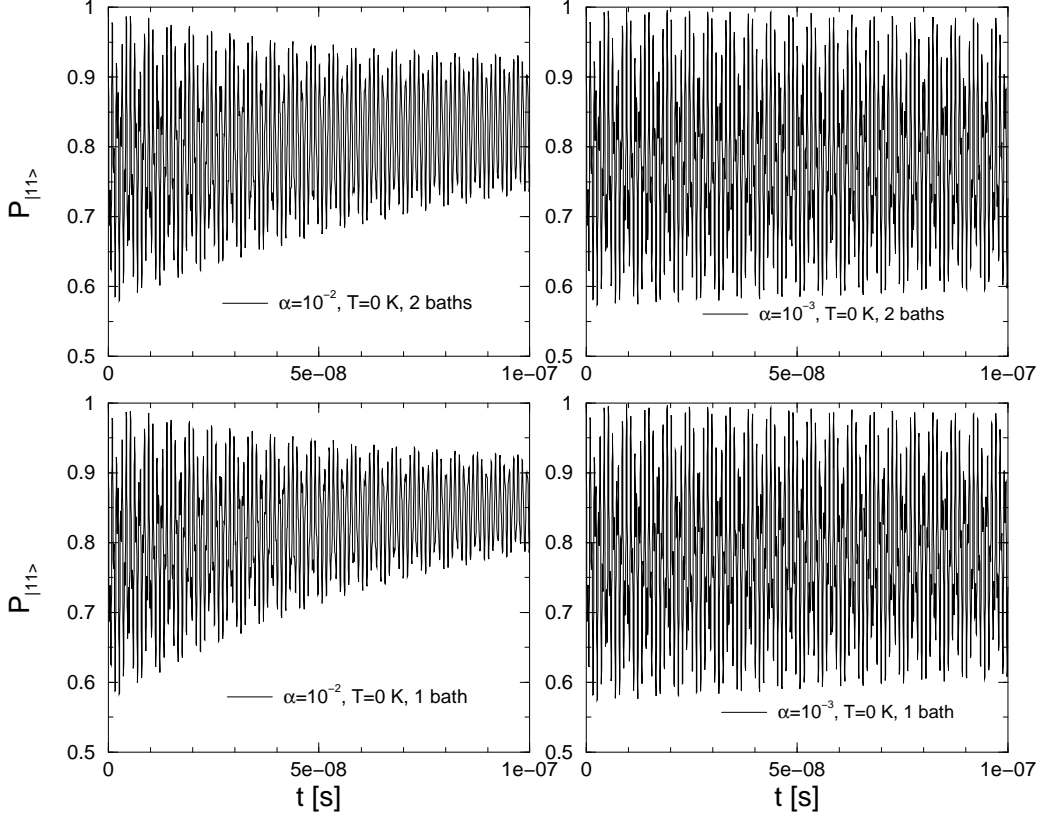


Figure 4.3: Plot of the occupation probability $P_{|11\rangle}(t) = P_{|\uparrow\uparrow\rangle}(t) = \langle 11|\rho(t)|11\rangle$ for starting in the initial state $|11\rangle$ at $t = 0$ s. Temperature is set to $T = 0$ K. First row shows the behaviour for two qubits coupling to two uncorrelated baths both for $\alpha = 10^{-3}$ and $\alpha = 10^{-2}$. The lower two plots show the behaviour for two qubits coupled to one common bath. The qubit parameters ϵ , η and K are all set to 1 GHz.

states and after the decoherence time the occupation probability of the eigenstates is given by the Boltzmann factors. This behaviour is depicted in figure 4.4. Here for $\alpha = 10^{-3}$ the cases of $T = 0$ K and $T = 100$ mK are compared. When the temperature is low enough the system will relax into the ground state, as illustrated by the right column of figure 4.4. Thus the occupation probability of the state $(1/\sqrt{2})(|E3\rangle + |E4\rangle)$ goes to zero because $|E2\rangle$ is the ground state. Here, in the case of zero temperature, the decoherence times for the case of one common or two distinct baths are of the same order of magnitude. The left column illustrates the behaviour when the temperature is increased. At $T = 100$ mK the system relaxes not yet (temperature is not high enough) into an equally populated state but tends towards it.

When calculating the elements of the Redfield tensor and evaluating the reduced density matrix it is instructive to demonstrate that at zero temperature the general relation holds [16]

$$\Gamma_R^{1b,2b} = \frac{2}{N_{lev} - 1} \sum_{n>m} \Gamma_{nm}^{1b,2b}, \text{ at } T = 0 \text{ K}, \quad (4.15)$$

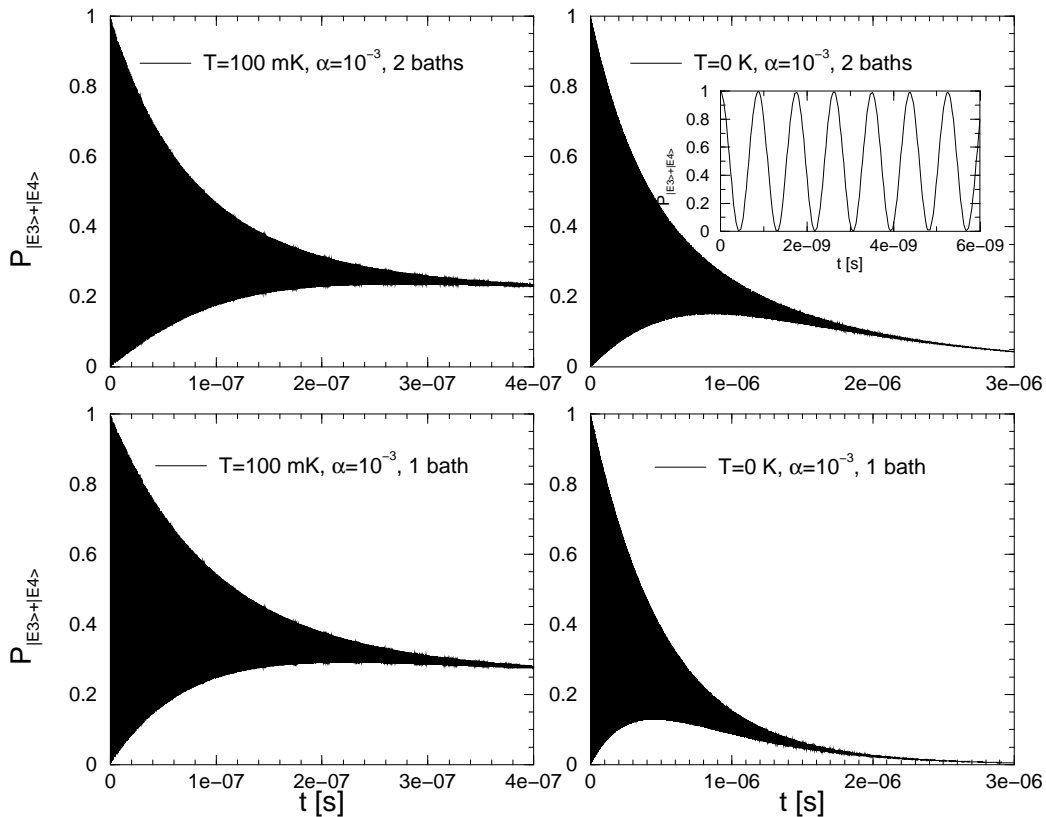


Figure 4.4: Plot of the occupation probability $P_{(1/\sqrt{2})(|E3\rangle+|E4\rangle)}(t)$ when starting in the initial state $(1/\sqrt{2})(|E3\rangle+|E4\rangle)$, which is a superposition of eigenstates $|E3\rangle$ and $|E4\rangle$ at $T = 0.1$ K. First row shows the behaviour for two qubits coupling to two uncorrelated baths. The lower row shows the behaviour for two qubits coupled to one common bath. The qubit parameters ϵ , η and K are set to 1 GHz, α is set to $\alpha = 10^{-3}$. The inset resolves the time scale of the coherent oscillations.

where $N_{lev} = 4$ for coupled qubits and Γ_R is the relaxation rate, defined as the sum of the four relaxation rates for the diagonal elements of the reduced density matrix $\Gamma_R = -\sum_n \Lambda_n$, where Λ_n are the four eigenvalues of the matrix $R_{n,m,n,m}$ with $n, m = 1 \dots 4$. The dephasing rates are defined as

$$\Gamma_{\varphi_{nm}}^{1b,2b} = -\text{Re}R_{n,m,n,m}^{1b,2b}, \quad (4.16)$$

with $n, m = 1 \dots 4, n \neq m$. From this follows that the dephasing rates are always smaller than the relaxation rate $\Gamma_R^{1b,2b}$. However one should be aware that in the case of a two qubit system there exist six dephasing and only four (three non-zero) relaxation channels.

4.5 Temperature dependence of the rates

Figure 4.5 displays the dependence of selected dephasing rates and the relaxation rate Γ_R (defined as the sum of the relaxation rates of the individual diagonal elements of the reduced density matrix) on temperature. The decoherence rates are the inverse decoherence times.

The rates are of the same magnitude for the case of one common bath and two distinct baths, but in the case of one common bath the dephasing rates $\Gamma_{\varphi_{21}} = \Gamma_{\varphi_{12}}$ go to zero when the temperature is decreased while all other rates saturate for $T \rightarrow 0$. If the temperature is increased from $T \approx 5 \cdot 10^{-2}$ K = 1 GHz the increase of the dephasing and relaxation rates follows a power law dependence. In the case of one common bath the slope b assumes values between $1.2 \cdot 10^8$ and $3.8 \cdot 10^8$ for the different rates. If the two qubits couple to two distinct baths b reaches values between $1.3 \cdot 10^8$ and $3.6 \cdot 10^8$. At temperature $T \approx 10^{-2}$ K the rates show a sharp increase for both cases. This roll off point is set by the characteristic energy scale of the problem which in turn is set by the energy bias ϵ , the transmission amplitude η and the coupling strength K . For the choice of parameters in figure 4.5 the characteristic energy scale expressed in temperature is $T \approx 0.5 \cdot 10^{-2}$ K. Note that there is also dephasing

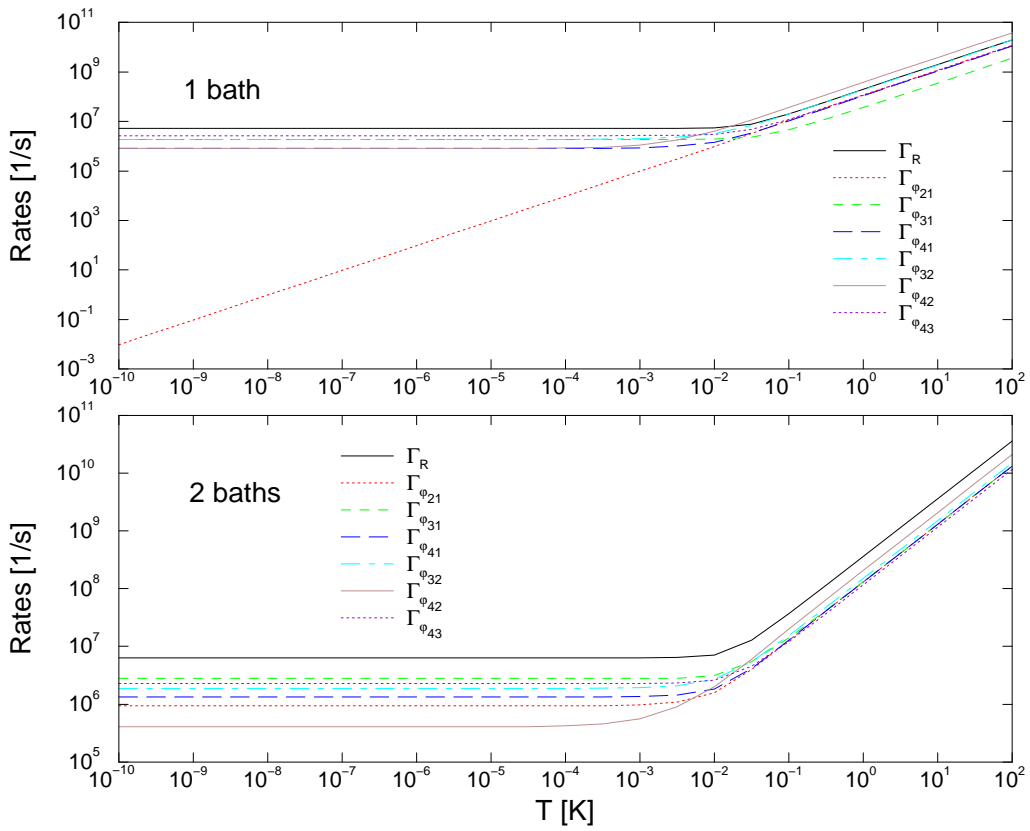


Figure 4.5: Log-log plot of the temperature dependence of the sum of the four relaxation rates and selected dephasing rates. Qubit parameters K , ϵ and η are all set to 1 GHz and $\alpha = 10^{-3}$. The upper panel shows the case of one common bath, the lower panel the case of two distinct baths. At the characteristic temperature of approximately $5 \cdot 10^{-2}$ K (set by the characteristic energy scale of the system; here $1 \text{ GHz} = (k_B/h) \cdot 5 \cdot 10^{-2}$ K) the rates increase very steeply.

between the singlet and the triplet states. When the system is prepared (by application of a suitable interaction) in a coherent superposition of singlet and triplet states the phase evolves coherently. Then two possible decoherence mechanisms can destroy phase coherence. First

there exist “flipless” processes, which can easily be explained when referring to the Bloch sphere, where the $\hat{\sigma}_z$ eigenstates $|\uparrow\rangle$ and $|\downarrow\rangle$ are the poles [43, 44]. If a spin-vector moves on a great circle which lies in a plane parallel to the plane spanned by the $\hat{\sigma}_x$ - and $\hat{\sigma}_y$ -axis, only the expectation value of the $\hat{\sigma}_z$ component will not change. Thus the processes where the spin-vector gets random kicks on a great circle in a plane parallel to the plane spanned by the $\hat{\sigma}_x$ and $\hat{\sigma}_y$ components are called “flipless” processes. These flipless processes are described by the terms (4.11) and (4.14) in the rates respectively. Obviously these terms vanish for $T \rightarrow 0$. This and the fact that for $T \rightarrow 0$ there are no transitions of the triplet part $|E2\rangle$ (ground state) to other triplet states possible (this will be explained below), explains why the rate $\Gamma_{\varphi_{21}}$ vanishes. Secondly, if the system is prepared in a superposition of a singlet and a triplet state, transitions between the triplet state (if the triplet state is *not* the ground state) and other triplet states (with lower energies) are possible. Therefore the triplet component is unstable and the other dephasing rates which involve the singlet state and a triplet state do not vanish. For our choice of parameters $|E2\rangle$ is the ground state and thus no transitions between the triplet state $|E2\rangle$ and other triplet states are possible at $T = 0$ K. If the system is prepared in a superposition of the singlet state and the states $|E3\rangle$ or $|E4\rangle$ (not the ground states), there might be transitions between the triplet state the system was prepared in and a triplet state with lower energy. These transitions will not vanish for $T \rightarrow 0$ and thus the dephasing rates $\Gamma_{\varphi_{31}}$ and $\Gamma_{\varphi_{41}}$ will not vanish for $T \rightarrow 0$. The described behaviour can be observed in figure 4.5.

If the parameters ϵ and η are tuned to zero, thus K being the only non-vanishing parameter in the two qubit operation (this is exactly the case for the two qubit operation needed when performing the XOR as described in the next chapter), all dephasing and relaxation rates will vanish for $T = 0$ K in the case of one common bath. This behaviour is depicted in figure 4.6. It originates from the special symmetries of the Hamiltonian in this case and the fact that for this particular two qubit operation the system Hamiltonian and the coupling to the bath are both diagonal. Therefore all rates vanish in the case of one common bath for $T \rightarrow 0$. This behaviour is also observed in the two gate quality factors fidelity and purity (figure 5.2) that are described in chapter 5.

Interestingly enough, for $\sigma_z^{(1)} \otimes \sigma_z^{(2)}$ type of inter-qubit coupling and $\sigma_z^{(i)} \otimes \hat{X}$ type of qubit-bath coupling, in the case of the two-qubit operation depicted in figure 4.6, the system Hamiltonian and the coupling to the bath do commute. (In this case $\epsilon = 0$ and $\eta = 0$.) Therefore the effects of decoherence are weaker compared to other types of inter-qubit coupling and coupling to the bath.

4.6 Discussion of the renormalization effects

Renormalization of the oscillation frequencies ω_{nm} is controlled by the imaginary part of the Redfield tensor [16]

$$\omega_{nm} \rightarrow \tilde{\omega}_{nm} := \omega_{nm} - \text{Im}R_{nmnm}. \quad (4.17)$$

Thus the real part of the Redfield tensor yields the relaxation and dephasing rates while the imaginary part causes an environment induced shift of the oscillation frequencies ω_{nm} . The

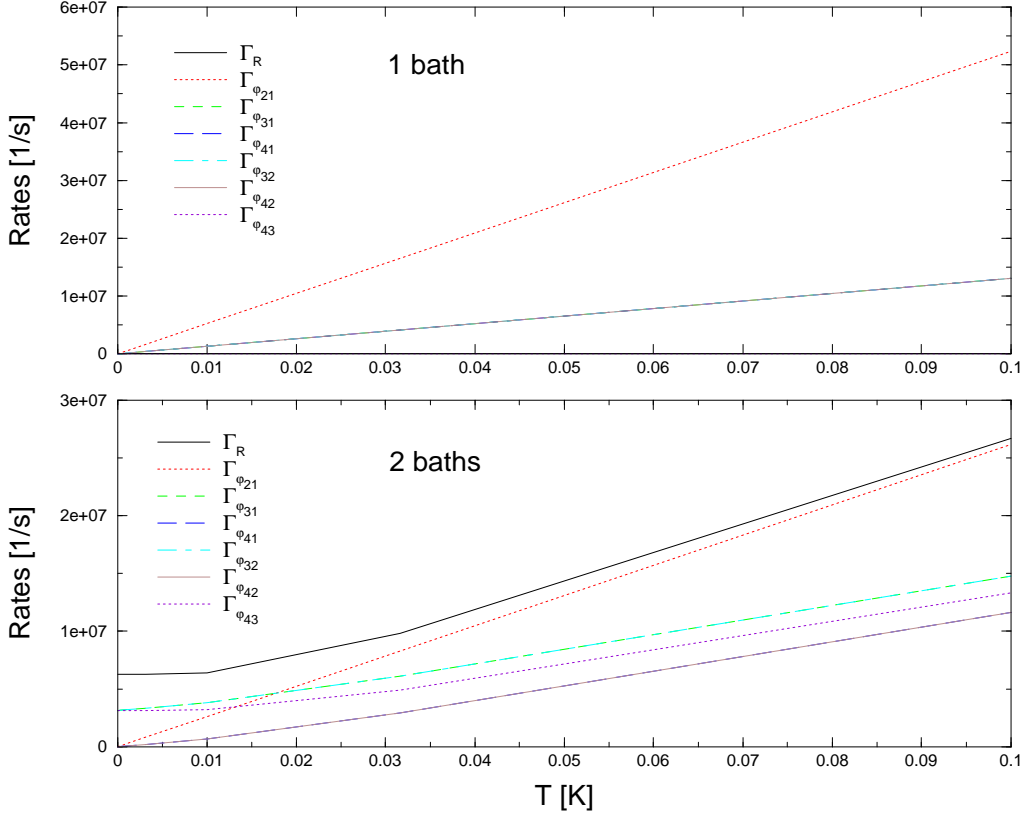


Figure 4.6: Plot of the temperature dependence of the sum of the four relaxation rates and selected dephasing rates. Qubit parameters ϵ and η are set to 0, K is set to 1 GHz, $\alpha = 10^{-3}$ corresponding to the choice of parameters used for the XOR operation. The upper panel shows the case of one common bath, the lower panel the case of two distinct baths. In the case of one common bath the system will experience no dissipative effects at $T = 0$ K.

imaginary part of the Redfield tensor is given by the imaginary part of the rates

$$\text{Im } \Gamma_{\ell mnk}^{(+)} = C_{1b,2b} \frac{1}{\pi \hbar} \int_0^{\infty} d\omega J(\omega) P \left(\frac{1}{\omega^2 - \omega_{nk}^2} \right) [\coth(\beta \hbar \omega / 2) \omega_{nk} - \omega] \quad (4.18)$$

and

$$\text{Im } \Gamma_{\ell mnk}^{(-)} = C_{1b,2b} \frac{1}{\pi \hbar} \int_0^{\infty} d\omega J(\omega) P \left(\frac{1}{\omega^2 - \omega_{lm}^2} \right) [\coth(\beta \hbar \omega / 2) \omega_{lm} + \omega], \quad (4.19)$$

where P denotes the principal value and $C_{1b,2b}$ are defined in equations (4.25) and (4.26). Therefore one has to evaluate the integral (the corresponding term for $\Gamma_{\ell mnk}^{(-)}$ is not explicitly discussed here because the calculation is completely analogous; the result is given below)

$$\hbar^{-1} \int_0^{\infty} d\omega J(\omega) P \left(\frac{1}{\omega^2 - \omega_{nk}^2} \right) [\coth(\beta \hbar \omega / 2) \omega_{nk} - \omega], \quad (4.20)$$

with an ohmic spectral density $J(\omega) = (\hbar\alpha\omega)/(1+\omega^2/\omega_c^2)$. This integral (4.20) might be split into two parts

$$I_1 = \int_0^\infty d\omega f_1(\omega) = \int_0^\infty d\omega \frac{\alpha\omega}{1 + \frac{\omega^2}{\omega_c^2}} \frac{1}{\omega - \omega_{nk}} \frac{1}{\omega + \omega_{nk}} \coth(\beta\hbar\omega/2)\omega_{nk} \quad (4.21)$$

$$-I_2 = \int_0^\infty d\omega f_2(\omega) = \int_0^\infty d\omega \frac{\alpha\omega}{1 + \frac{\omega^2}{\omega_c^2}} \frac{1}{\omega - \omega_{nk}} \frac{1}{\omega + \omega_{nk}} \omega. \quad (4.22)$$

After a lengthy calculation (see appendix C) we receive for $\Gamma_{\ell mnk}^{(+)}$

$$\text{Im } \Gamma_{\ell mnk}^{(+)} = C_{1b,2b} \frac{\alpha\omega_c^2\omega_{nk}}{2\pi(\omega_c^2 + \omega_{nk}^2)} \left[\psi(1 + c_2) + \psi(c_2) - 2\text{Re}[\psi(ic_1)] - \pi \frac{\omega_c}{\omega_{nk}} \right], \quad (4.23)$$

with $c_1 := (\omega_{nk}\beta\hbar)/(2\pi)$, $c_2 := (\beta\hbar\omega_c)/(2\pi)$. In the case of $\Gamma_{\ell mnk}^{(-)}$ the expression is

$$\text{Im } \Gamma_{\ell mnk}^{(-)} = C_{1b,2b} \frac{\alpha\omega_c^2\omega_{\ell m}}{2\pi(\omega_c^2 + \omega_{\ell m}^2)} \left[\psi(1 + c_2) + \psi(c_2) - 2\text{Re}[\psi(ic_1)] + \pi \frac{\omega_c}{\omega_{\ell m}} \right], \quad (4.24)$$

with $c_1 := (\omega_{\ell m}\beta\hbar)/(2\pi)$. Here $C_{1b,2b}$ denotes a pre-factor, which reads in the case of two distinct baths

$$C_{2b} = \frac{1}{4} \left[\sigma_{z,\ell m}^{(1)} \sigma_{z,nk}^{(1)} + \sigma_{z,\ell m}^{(2)} \sigma_{z,nk}^{(2)} \right] \quad (4.25)$$

and in the case of one common bath

$$C_{1b} = \frac{1}{4} \left[\sigma_{z,\ell m}^{(1)} \sigma_{z,nk}^{(1)} + \sigma_{z,\ell m}^{(1)} \sigma_{z,nk}^{(2)} + \sigma_{z,\ell m}^{(2)} \sigma_{z,nk}^{(1)} + \sigma_{z,\ell m}^{(2)} \sigma_{z,nk}^{(2)} \right]. \quad (4.26)$$

The terms in (4.23) and (4.24) which are linear in ω_c give no net contribution to the imaginary part of the Redfield tensor [16]. To illustrate the size of the renormalization effects, the ratio of the renormalization effects to the frequencies which are renormalized is depicted in figure 4.7.

If c_1 and c_2 are big and the Ψ -functions can be approximated by a logarithm the resulting expression for the renormalization effects will be independent of temperature. Therefore it only makes sense to plot the temperature dependence of (4.23) and (4.24) for high temperatures, where c_1 and c_2 are small and the renormalization effects are very weak. For the case of small c_1 and c_2 , the temperature dependence of the renormalization effects is depicted in figure 4.7.

The rates (4.23) and (4.24) diverge logarithmically with ω_c . When comparing the upper left ($T = 0$ K) and upper right ($T = 100$ mK) panel, one recognizes that for the first case one common bath gives smaller renormalization effects than two distinct baths, while in the second case for $T = 100$ mK the renormalization effects deviate only slightly (see the behaviour for ω_{23}) and the renormalization effects are smaller for the case of two distinct baths. (This temperature dependence can also be observed in the gate quality factors. These are discussed in chapter 5.) The effects of renormalization are always very small (below 1% for our choice of parameters) and are therefore neglected in our calculations. The case of large

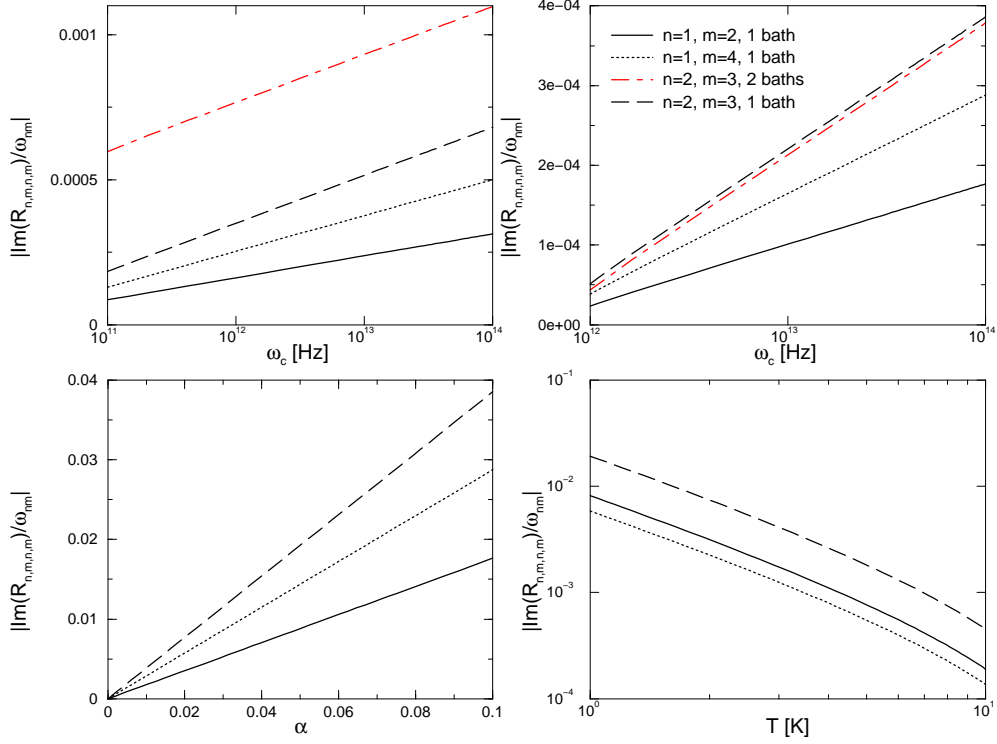


Figure 4.7: From upper left to lower right: 1) Plot of the ratio of the renormalization effects and the corresponding transition frequencies. Parameters: $\alpha = 10^{-3}$, $T = 0$ K and ω_c is varied between 10^{11} and 10^{14} for several frequencies (ω_{12} , ω_{14} and ω_{23}) for the case of two baths and in the case of ω_{23} also for the case of one common bath, 2) The parameters for the upper right plot are $\alpha = 10^{-3}$, $T = 100$ mK and ω_c is varied between 10^{12} and 10^{14} , 3) Plot of the the dissipation strength dependence of the renormalization effects. The parameters are $T = 0.1$ K, $\omega_c = 10^{13}$ and α is varied between 10^{-7} and 10^{-1} , 4) Log-log plot of the temperature dependence of the renormalization effects. Here $\alpha = 10^{-3}$ and $\omega_c = 10^{13}$. Note that for small temperatures the renormalization effects do *not* depend on temperature. (This is elucidated further in chapter 4.6.) Plot 1) and 2) are scaled logarithmically to emphasize the logarithmic divergence of the renormalization effects with ω_c .

renormalization effects is discussed in [45]. However, having calculated (4.23) and (4.24) these are easily incorporated in our calculation. We only plotted the size of the renormalization effects for ω_{12} , ω_{14} and ω_{34} , because in general all values of ω_{nk} are of the same magnitude and give similar plots. Figure 4.7 also shows the dependence on α . Here the temperature T is fixed to $T = 0.1$ K. From figure 4.7 we can conclude that the size of the renormalization effects diverges linearly with α , the dimensionless parameter which describes the strength of the dissipative effects.

The cutoff frequency ω_c is given by the circuit properties. For a typical first order low-pass LR filter in a qubit circuit [13] one can insert $R = 50 \Omega$ (typical impedance of coaxial cables) and $L \approx 1$ nH (depends on the length of the circuit lines) into $\omega_{LR} = R/L$ and gets that $\omega_{LR} \approx 5 \cdot 10^{10}$ Hz. ω_{LR} is the largest frequency in the problem (see again [13], chapter 4.5) and $\omega_c \gg \omega_{LR}$ should hold. Then $\omega_c \approx 10^{13}$ Hz as cutoff frequency seems to be a reasonable assumption.

Chapter 5

Gate Quality Factors

In the last chapter 4 we evaluated the dephasing and relaxation rates (and thus the dephasing and relaxation times) of the two qubit system that is affected by a dissipative environment. Furthermore we visualized the dynamics of the two qubit system. However, qubits are thought to perform gate operations and with these measures one can not judge how well quantum gate operations might be performed with the two qubit system. Therefore, to get a quantitative measure of how our two qubit system behaves when performing a quantum logic gate operation, one can evaluate the gate quality factors proposed by Poyatos, Cirac and Zoller [24]. They define four quantities which quantify a quantum logic operation: the fidelity, purity, quantum degree and entanglement capability. The fidelity is defined as

$$\mathcal{F} = \frac{1}{16} \sum_{j=1}^{16} \langle \Psi_{in}^j | U_{XOR}^+ \rho_{XOR}^j U_{XOR} | \Psi_{in}^j \rangle, \quad (5.1)$$

where $\rho_{XOR}^j = \rho(t_{XOR})$ with initial condition $\rho(0) = |\Psi_{in}^j\rangle \langle \Psi_{in}^j|$. The fidelity is a measure of how well a quantum logic operation was performed. Without dissipation the reduced density matrix ρ_{XOR}^j after performing the quantum XOR operation, applying U_{XOR} and the inverse U_{XOR}^+ would equal $\rho(0)$. Therefore the fidelity for the ideal quantum gate operation should be 1. The second quantifier is the purity

$$\mathcal{P} = \frac{1}{16} \sum_{j=1}^{16} \text{tr} \left((\rho_{XOR}^j)^2 \right), \quad (5.2)$$

which should be 1 for the ideal quantum gate operation without dissipation. The purity characterizes the effects of decoherence. The third quantifier, the quantum degree, is defined as the maximum overlap of the resulting density matrix after the XOR-operation with the maximum entangled Bell-states

$$\mathcal{Q} = \max_{j,k} \langle \Psi_{me}^k | \rho_{XOR}^j | \Psi_{me}^k \rangle, \quad (5.3)$$

where the Bell-states Ψ_{me}^k are defined according to

$$|\Psi_{me}^{00}\rangle = \frac{|\uparrow\uparrow\rangle + |\downarrow\downarrow\rangle}{\sqrt{2}}, \quad |\Psi_{me}^{01}\rangle = \frac{|\uparrow\downarrow\rangle + |\downarrow\uparrow\rangle}{\sqrt{2}}, \quad (5.4)$$

$$|\Psi_{me}^{10}\rangle = \frac{|\uparrow\uparrow\rangle - |\downarrow\downarrow\rangle}{\sqrt{2}}, \quad |\Psi_{me}^{11}\rangle = \frac{|\uparrow\downarrow\rangle - |\downarrow\uparrow\rangle}{\sqrt{2}}. \quad (5.5)$$

For the ideal operation the quantum degree should be 1. The quantum degree characterizes nonlocality. It has been shown [46] that all density operators that have an overlap with a maximally entangled state that is larger than the value $(2 + 3\sqrt{2})/8 \approx 0.78$ [47] violate the Clauser-Horne-Shimony-Holt inequality. Thus these density operators are non-local. The fourth quantifier, the entanglement capability \mathcal{C} , is the smallest eigenvalue of the partial transposed density matrix for all possible unentangled input states $|\Psi_{in}^j\rangle$. (See below for the definition of all possible input states needed to build all possible initial density matrices.) It has been shown [48] to be negative for an entangled state. Ideally this quantifier should be -0.5 for the ideal operation thus characterizing a maximally entangled state. Two of the gate quality factors, namely the fidelity and purity might also be calculated for single qubit gates [44]. However, entanglement can only be observed in a system of at least two qubits. Therefore the quantum degree and entanglement capability can not be evaluated for single qubit gates.

To form all possible initial density matrices, needed to calculate the gate quality factors, we use the 16 unentangled product states $|\Psi_{in}^j\rangle$, $j = 1, \dots, 16$ defined [47] according to $|\Psi_a\rangle_1 |\Psi_b\rangle_2$, ($a, b = 1, \dots, 4$), with $|\Psi_1\rangle = |0\rangle$, $|\Psi_2\rangle = |1\rangle$, $|\Psi_3\rangle = (1/\sqrt{2})(|0\rangle + |1\rangle)$, and $|\Psi_4\rangle = (1/\sqrt{2})(|0\rangle + i|1\rangle)$. They form one possible basis set for the superoperator ν_{XOR} with $\rho(t_{XOR}) = \nu_{XOR}\rho(0)$ [24, 47]. The states are chosen to be unentangled to avoid the preceding application of a two qubit gate to prepare the initial state of the system.

5.1 Implementation of the XOR-operation

Due to the fact that the XOR (or CNOT) gate, together with the set of all one-qubit rotations, is complete for quantum computation [49], the XOR gate is the most important two-qubit gate operation. Therefore we further investigate the behaviour of the four gate quality factors when performing a XOR operation. The classical XOR operation switches the second bit, depending on the value of the first bit of a two bit system. In the computational basis ($|00\rangle, |01\rangle, |10\rangle, |11\rangle$) this operation has the following matrix form

$$U_{XOR} = \begin{pmatrix} 1 & 0 & 0 & 0 \\ 0 & 1 & 0 & 0 \\ 0 & 0 & 0 & 1 \\ 0 & 0 & 1 & 0 \end{pmatrix}. \quad (5.6)$$

Up to a phase factor the two qubit XOR (or CNOT) operation is given by the following sequence of five single-qubit and one two-qubit quantum logic operation. Each of these six operations has to be modeled by an appropriate Hamiltonian undergoing free unitary time evolution $\exp(-i/\hbar)\mathbf{H}_{op}t$. The single-qubit operations are handled with Bloch-Redfield formalism, like the two-qubit operations. We assume dc pulses (instantaneous on and off switching of the Hamiltonian with zero rise time of the signal) or rectangular pulses

$$U_{XOR} = \exp\left(-i\frac{\pi}{2}\left(\frac{\sigma_x^{(2)} + \sigma_z^{(2)}}{\sqrt{2}}\right)\right) \exp\left(i\frac{\pi}{4}\sigma_z^{(1)}\right) \exp\left(i\frac{\pi}{4}\sigma_z^{(2)}\right) \times \\ \times \exp\left(i\frac{\pi}{4}\sigma_z^{(1)}\sigma_z^{(2)}\right) \exp\left(i\frac{\pi}{2}\sigma_z^{(1)}\right) \exp\left(-i\frac{\pi}{2}\left(\frac{\sigma_x^{(2)} + \sigma_z^{(2)}}{\sqrt{2}}\right)\right). \quad (5.7)$$

No.	operation	parameters [GHz]	time [s]
1	$\exp\left(-i\frac{\pi}{2}\left(\frac{\sigma_x^2+\sigma_z^2}{\sqrt{2}}\right)\right)$	$\epsilon_2 = -2\xi, \Delta_2 = -\sqrt{2}\xi$	$\tau_1 = \frac{\sqrt{2}}{8\xi}$
2	$\exp\left(i\frac{\pi}{2}\sigma_z^1\right)$	$\epsilon_1 = -\xi$	$\tau_2 = \frac{1}{2\xi}$
3	$\exp\left(i\frac{\pi}{4}\sigma_z^1\sigma_z^2\right)$	$K = -\xi$	$\tau_3 = \frac{1}{4\xi}$
4	$\exp\left(i\frac{\pi}{4}\sigma_z^2\right)$	$\epsilon_2 = \xi$	$\tau_4 = \frac{1}{4\xi}$
5	$\exp\left(i\frac{\pi}{4}\sigma_z^1\right)$	$\epsilon_1 = \xi$	$\tau_5 = \frac{1}{4\xi}$
6	$\exp\left(-i\frac{\pi}{2}\left(\frac{\sigma_x^2+\sigma_z^2}{\sqrt{2}}\right)\right)$	$\epsilon_2 = -2\xi, \Delta_2 = -\sqrt{2}\xi$	$\tau_6 = \frac{\sqrt{2}}{8\xi}$

Table 5.1: Parameters of the Hamiltonians, only the non-zero parameters are listed; $\xi = 1$ GHz in our case.

Table 5.1 shows the parameters we inserted into the one- and two-qubit Hamiltonian to receive the XOR operation. In our case we assumed $\xi = 1$ GHz. However, there is no restriction in the usage of other values for ξ . As one can see from table 5.1 the times of unitary evolution which are approximately the inverse of the corresponding energies in GHz are in the nanosecond range.

To better visualize the pulse sequence, needed to perform the quantum XOR operation that was already given in table 5.1, figure 5.1 depicts the values of the elements of the Hamiltonians. Interestingly enough we find that for the only two-qubit operation included in the whole XOR operation ϵ and η are zero. Thus K is the only non-zero parameter and \mathbf{H}_{2qb} assumes diagonal form. Negative and positive values of the energies can be accomplished by tuning the magnetic frustration through the qubit loop below $f = 1/2$ or above $f = 1/2$.

To obtain the final reduced density matrix after performing the six unitary operations (5.7), we iteratively determine the density matrix after each operation with Bloch-Redfield theory and insert the attained resulting density matrix as initial density matrix into the next operation. This procedure is repeated for all possible unentangled initial states given in the last section. We inserted no additional time intervals between the operations. This is usually needed, if one applies Bloch-Redfield formalism, because Bloch-Redfield formalism is known to violate positivity on short timescales. However, we circumvent this problem in our calculations by dropping the memory after each operation, when we iteratively calculate the reduced density matrix.

5.2 Temperature dependence

The dependence of the four gate quality factors on temperature is depicted in figure 5.2. At temperatures below $T = 2.5 \cdot 10^{-2}$ K = 0.5 GHz the purity and fidelity are clearly higher for the case of one common bath, but if temperature is increased above this characteristic threshold, fidelity and purity are higher for the case of two baths.

In the case of one common bath the fidelity and purity are approaching their ideal value 1, when temperature goes to zero. This is related with the fact that in the case of one common bath all relaxation and dephasing rates vanish, due to the special symmetries of the

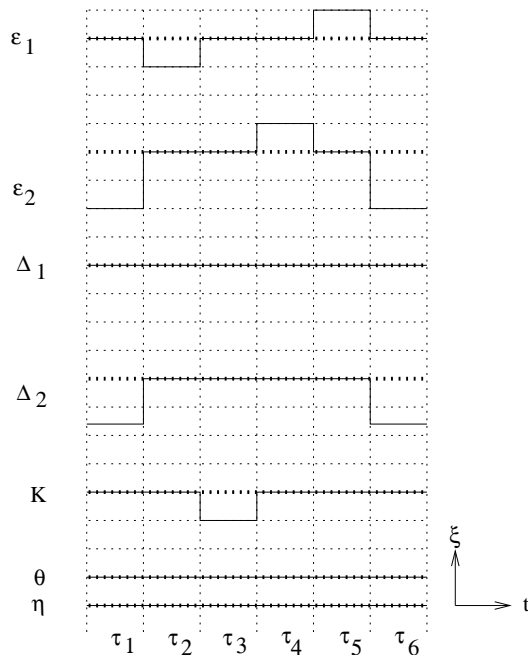


Figure 5.1: *Pulse sequence needed to perform the quantum XOR operation. Here the elements of the unperturbed single- and two-qubit Hamiltonian needed to perform a certain operation undergoing free unitary time evolution are shown. The arrow denotes $\xi = 0$ and the horizontal lines are spaced by $|\xi| = 1$ GHz. The durations of each pulse are not equal in general $\tau_j \neq \tau_i$, $i, j = 1, \dots, 6$ (cf. table 5.1)*

Hamiltonian, when temperature goes to zero as depicted in figure 4.6. However, the quantum degree and the entanglement capability tend towards their ideal values for both the case of one common and two distinct baths. This is due to the fact that both quantum degree and entanglement capability are, different than fidelity and purity, not defined as mean values but rather characterize the “best” possible case of all given input states. Figure 4.6 shows that also for the case of two distinct baths there are only 3 non-vanishing rates for $T \rightarrow 0$. The system, being prepared in one of the 16 initial states, might relax into one of the eigenstates that is an entangled state. Because of this, both the entanglement capability and the quantum degree tend towards their ideal values for $T \rightarrow 0$.

From comparison of the value of the quantum degree for the case of one common and two distinct baths, we see that the quantum degree is always bigger for the case of two qubits coupling to one common bath. This is due to the fact, that the decoherence rates are always slightly bigger for the case of one common bath. Thus, even if only the state of all 16 input states is selected, which gives the maximal possible overlap, also this state will experience bigger decoherence effects for the case of one common bath. However, when looking at the entanglement capability, we observe that the case of two distinct baths always leads to a better value, thus meaning that the two qubits are higher entangled.

Compared to a recent work by Thorwart and Hänggi [47] where the authors stated that

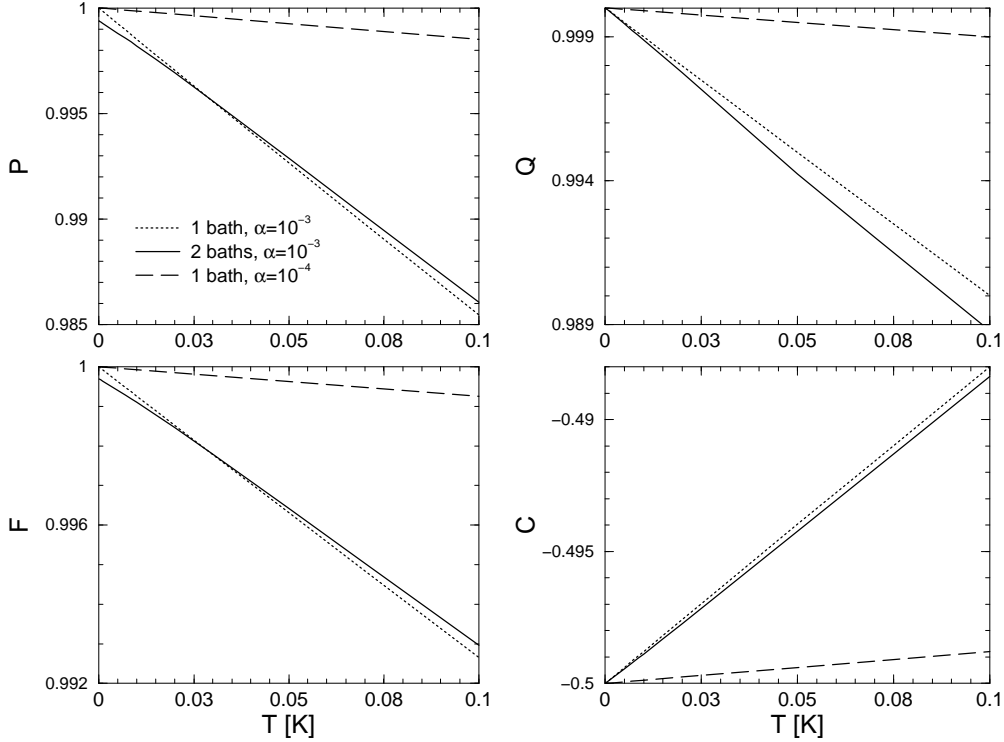


Figure 5.2: Temperature dependence of the four gate quantifiers. Here the temperature is varied from 10^{-10} K to 0.1 K. Here $\alpha = \alpha_1 = \alpha_2 = 10^{-3}$ and for the case of one common bath also $\alpha = 10^{-4}$ is shown. All other parameters are given by table 5.1.

for the case of one common bath the gate quality factors depend only very weakly on temperature we find similar results. They set the strength of the dissipative effects to $\alpha = 10^{-4}$. Their choice of parameters was $\epsilon = 10$ GHz, $\Delta = 1$ GHz and $K = 0.5$ GHz which is on the same order of magnitude as the values given in table 5.1. In figure 5.2 we observe a linear decrease of the gate quality factors for the case of one common bath in the same temperature range discussed by Thorwart and Hänggi, both for $\alpha = 10^{-3}$ and $\alpha = 10^{-4}$, but in the latter case the slope is much smaller and the gate quality factors exhibit a weaker temperature dependence.

In figure 5.3 the deviations of the gate quality factors from their ideal values are depicted as a log-log plot. Here, we can observe the saturation of the deviation for the case of two baths much more clearly than in figure 5.2. For given α the fidelity and purity can not be increased anymore by lowering the temperature in the case of two distinct baths. Interestingly enough, we observe that for the quantum degree and entanglement capability the two cases of one and two baths exchange their roles. This behaviour was already explained in the last paragraph. The quantum degree is always bigger for the case of one common bath whereas the entanglement capability is always closer to its ideal value for the case of two distinct baths. Above a temperature of 10^{-2} K the decrease of the gate quality factors shows a power law dependence for both cases. We observe finite decoherence effects in the fidelity and the purity

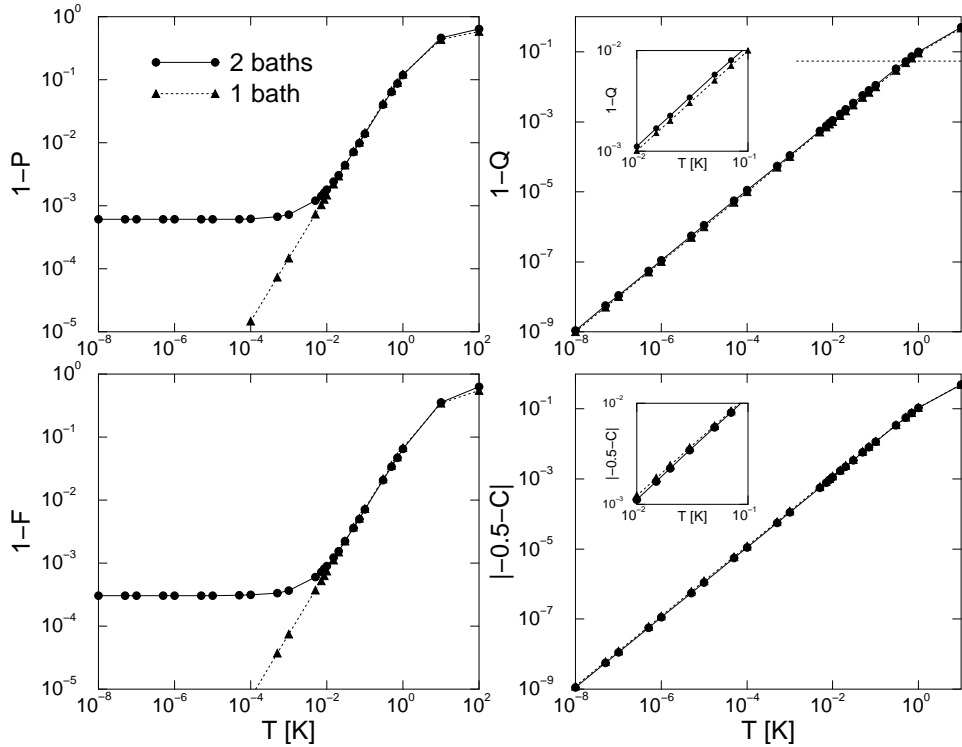


Figure 5.3: Log-log plot of the temperature dependence of the deviations of the four gate quantifiers from their ideal values. Here the temperature is varied from 10^{-10} K to 0.1 K. In all cases $\alpha = \alpha_1 = \alpha_2 = 10^{-3}$. The dotted line indicates the upper bound set by the Clauser-Horne-Shimony-Holt inequality.

also at $T = 0$ for the case of two distinct baths, resulting from the coupling of the system to the environment of harmonic oscillators which (at $T = 0$ K) are all in their ground states. But for the case of one common bath, the deviation from the ideal fidelity goes to zero when temperature goes to zero. This is due to the special symmetries (K is the only *nonvanishing* parameter in the two-qubit operation) of the Hamiltonian. This symmetries are also reflected in the temperature dependence of the rates, figure 4.6. There, for one common bath, all rates vanish for $T \rightarrow 0$.

The dotted line in figure 5.3 shows that the temperature has to be less than about $T = 1$ K in order to obtain values of the quantum degree being larger than $Q \approx 0.78$. Only then, the Clauser-Horne-Shimony-Holt inequality is violated and non-local correlations between the qubits occur as described in [47].

5.3 Dependence on the dissipation strength

To improve the gate quality factors one could try to lower the temperature of the environment. However, generally (if no special symmetries of the Hamiltonian are present) there are always finite decoherence effects also at $T = 0$ K, at least for the case of two distinct baths. Therefore

we can not improve the gate quality factors, for the case of two distinct baths, below a certain saturation value when lowering the temperature. By better isolating the system from the environment one can decrease the strength of the dissipative effects characterized by α . Figure 5.4 illustrates the α -dependence of the deviation of the gate quality factors from their ideal values. The deviations from the ideal values of the gate quantifiers possess a powerlaw

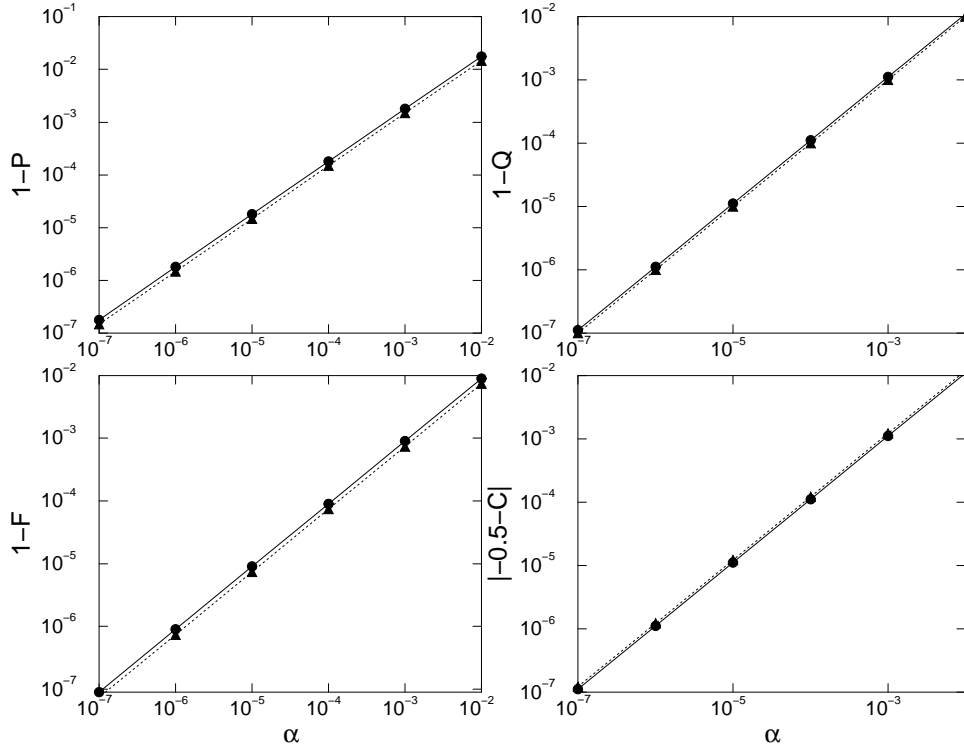


Figure 5.4: Dissipation strength dependence of the deviations from the ideal values in log-log representation. The dimensionless parameter α (here both the single- and the two-qubit α have the same value) which describes the strength of the dissipative effects is varied from 10^{-7} to 10^{-2} . The temperature is fixed to 10 mK.

dependence. We observe that the dependence of the gate quality factors on α is linear as expected. In order to obtain the desired value of 0.999 99 for \mathcal{F} , \mathcal{P} and \mathcal{Q} [47] α needs to be below $\alpha = 10^{-6}$ at $T = 10$ mK.

5.4 Time resolved XOR operation

To investigate the anatomy of the XOR quantum logic operation we calculated the occupation probabilities of the singlet/triplet states after each of the six operations, of which the XOR consists. This time resolved picture of the dynamics of the two-qubit system, when performing a gate operation, gives insight into details of our implementation of the XOR operation and the dissipative effects occurring during the operation. Thus we are able to completely characterize the physical process which maps the input density matrix ρ_0 to ρ_{out} in an open quantum system [24]. When the system is prepared in the state $|\uparrow\uparrow\rangle = |00\rangle$ the XOR oper-

ation (5.6) does not alter the initial state and after performing the XOR operation the final state should equal the initial state $|\uparrow\uparrow\rangle = |00\rangle$. This can clearly be observed in figure 5.5.

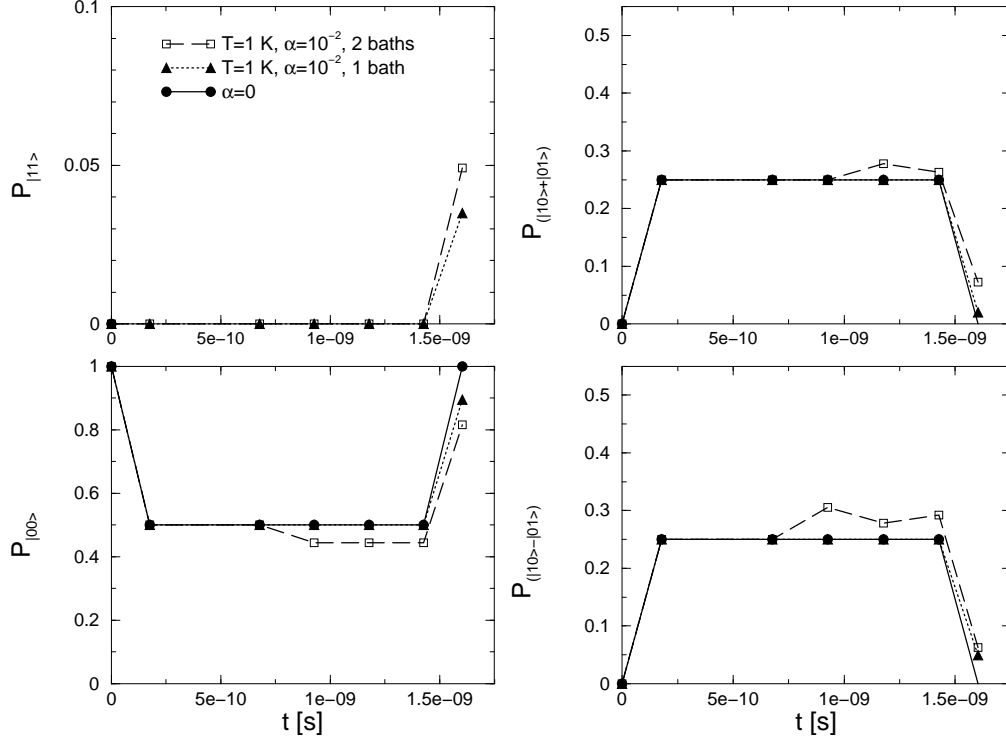


Figure 5.5: Time resolved XOR operation. Occupation probabilities of the singlet/triplet states are shown after completion of a time step τ_i ($i = 1, \dots, 6$). The system is initially prepared in the state $|00\rangle$. For $\alpha = \alpha_1 = \alpha_2 = 10^{-2}$ and $T = 1$ K clearly deviations from the ideal case can be observed. Qubit parameters are set according to table 5.1.

During the XOR operation occupation probabilities of the four states change according to the individual operations given in (5.7). At $T = 1$ K, the case of 2 baths differs significantly from the case of one common bath. After the third operation (the two-qubit operation; only there the distinction between one common or two distinct baths makes sense) occupation probabilities are different for both environments resulting in a less ideal result for the case of two baths. This is also reflected in figure 5.2 where compared to the case of one common bath at $T = 1$ K the purity is much smaller for the case of two baths and hence the resulting state $|\uparrow\uparrow\rangle = |00\rangle$ is less pure for two distinct baths.

In figure 5.5 the resulting state after performing the XOR operation always deviates more from the ideal value (for $\alpha = 0$, i.e. no dissipation) for the case of two distinct baths if all other parameters are fixed and set to the same values for the both cases. The state $P_{|00\rangle}$ is less close to the ideal occupation probability 1 and the other singlet/triplet states are also less close to their ideal value for the case of two distinct baths. The case of two distinct baths also shows bigger deviations from the ideal case ($\alpha = 0$) *during* the XOR operation (see figure 5.5). But, if the system is initially prepared in the state $|\uparrow\uparrow\rangle = |11\rangle$ the case of two dis-

tinct baths shows bigger deviations from the ideal case during the XOR operation, while the resulting state is closer to the ideal case for two distinct baths compared to one common bath.

Gazing at figure 5.6 we recognize that when preparing the system in the state $|\uparrow\uparrow\rangle = |11\rangle$ we do receive the state $|\uparrow\downarrow\rangle = |10\rangle$ after performing the XOR operation, which flips the state of the second bit iff the state of the first bit is $|\uparrow\rangle = |1\rangle$. In figures 5.5 and 5.6 it looks

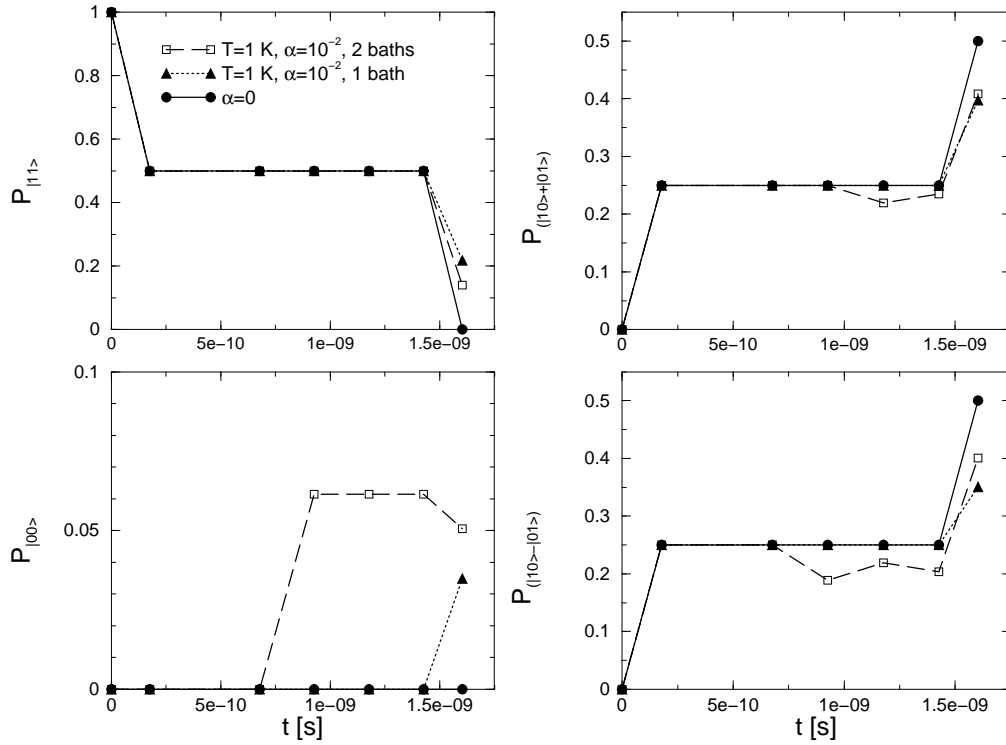


Figure 5.6: Time resolved XOR operation. Occupation probabilities of the singlet/triplet states are shown after completion of a time step τ_i ($i = 1, \dots, 6$). The system is initially prepared in the state $|11\rangle$. For $\alpha = \alpha_1 = \alpha_2 = 10^{-2}$ and $T = 1$ K deviations from the ideal case can be observed. Qubit parameters are set according to table 5.1.

like there would be no decoherence effects (or at least much weaker decoherence effects) after performing the (first two) single-qubit operations. However, not all input states are affected by the decoherence effects the same way and when regarding all possible input states there are finite decoherence effects. This can be explained with figure 5.7. Figure 5.7 depicts the time resolved purity when performing the XOR operation. We clearly observe that there are finite decoherence effects for the first single-qubit operations in 5.7. The difference between the single-qubit and two-qubit operations is the steeper decrease of the purity due to stronger decoherence in the case of the two-qubit operation. The upper panel in figure 5.7 depicts the behaviour of the purity for $T \rightarrow 0$. We still observe relatively strong decoherence in the case of two distinct baths, but single-qubit decoherence is very small and will vanish for $T \rightarrow 0$. This can be seen from the inset where the case of one common bath is enlarged.

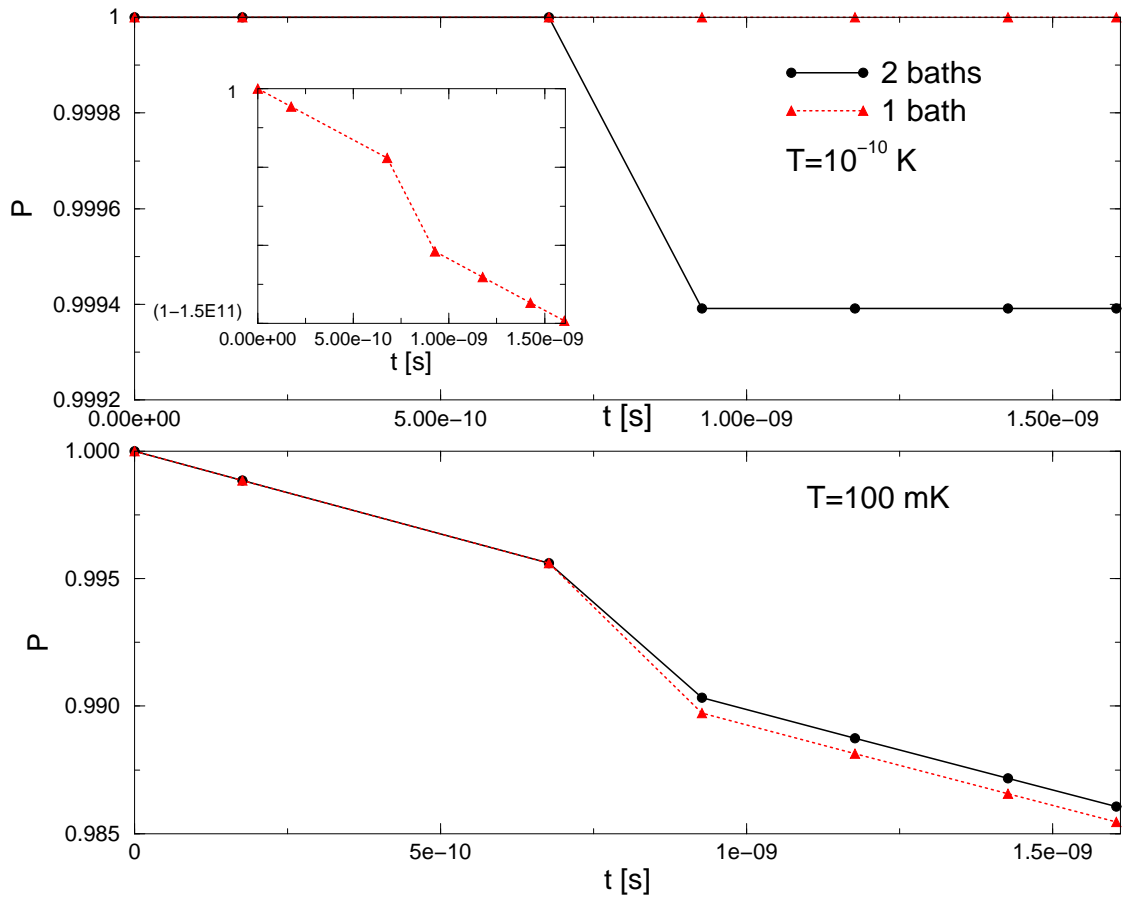


Figure 5.7: Time resolved Purity for the XOR operation. The value of the purity after each time step τ_i ($i = 1, \dots, 6$) is shown. Here $\alpha = \alpha_1 = \alpha_2 = 10^{-2}$ and $T = 100$ mK or $T \approx 0$ K. Qubit parameters are set according to table 5.1.

Chapter 6

Flux transformer

6.1 Josephson field-effect transistor (JoFET)

A Josephson field-effect transistor is assembled much like a metal-oxide-semiconductor field-effect transistor (MOSFET). Here, the source and drain contacts are superconducting niobium pads [50]. Under the channel defined by the SiO_2 in between the Nb contacts, the

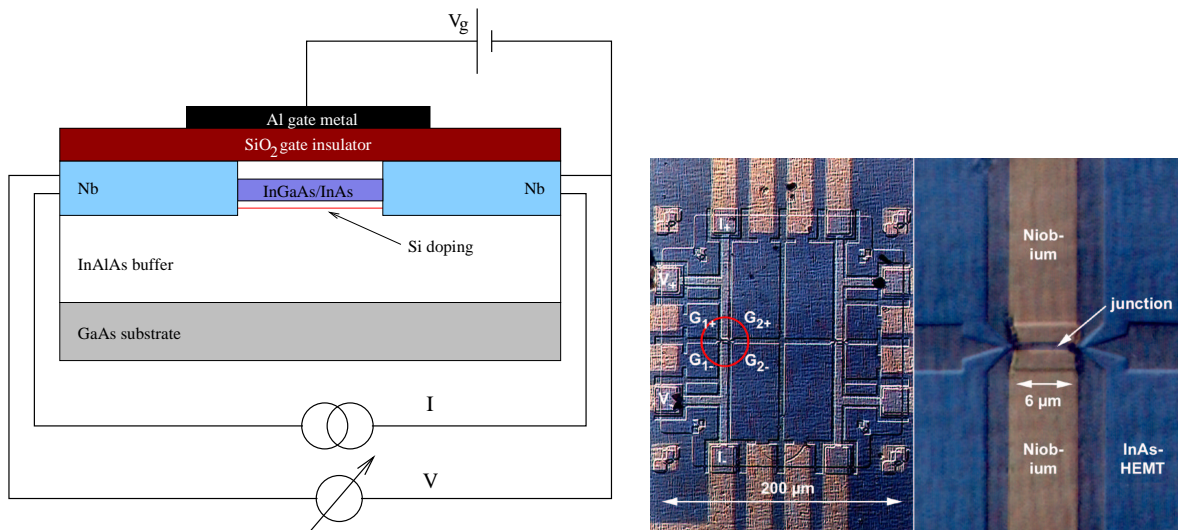


Figure 6.1: Left picture is a schematic sketch of a Josephson field-effect transistor. An oxide layer separates the aluminium gate and the SNS contact. A typical width of the contact is $w = 20 \mu\text{m}$ and length $l = 600 \text{ nm}$ [50]. Right picture is a micrograph of a SNS transistor. Different from a JoFET, there is no gate fabricated on top of the junction and contacts are fabricated on both sides of the SNS transistor [50].

inversion layer constitutes a quasi two-dimensional electron gas (2DEG). By applying a gate voltage it is possible to tune the electron density of the 2DEG which may be considered as a weak link between the two superconductors. Critical current for the devices depicted in figure 6.1 increases with the gate voltage up to a typical value of approximately $50 \mu\text{A}$ at $V_g = 20 \text{ V}$.

For $T \rightarrow 0$, in short clean SNS junctions the critical supercurrent carried by a single conducting channel depends only on the superconducting energy gap Δ which is the smallest energy scale. Here the formula of Kulik and Omel'yanchuk [25, 51, 52]

$$I_c = \frac{\pi\Delta}{R_N e} \quad (6.1)$$

for the critical current I_c holds. $R_N = h/(2e^2M)$ is the point-contact resistance of the region N containing M . Here, the backgate changes M .

6.2 Properties of the Flux Transformer

As a possible scheme to couple two qubits we investigate a flux transformer consisting of a SQUID loop around the two qubits with a JoFET whose circuit diagram is an overdamped Josephson junction as an on/off switch (cf. fig. 6.2). The two flux qubits are both coupled

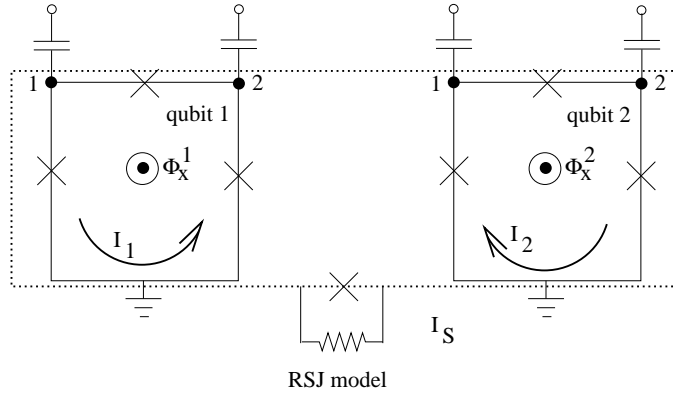


Figure 6.2: The flux transformer couples two flux qubits inductively. The JoFET is modeled as an overdamped Josephson junction.

inductively to the flux transformer loop that mediates the coupling.

In the following two sections we calculate the strength K of the coupling between the two qubits for the two cases of no switch, to turn the coupling on and off, and a tunable Josephson junction as a switch.

6.2.1 No switch

The change of the flux through qubit 1 (2) can be calculated by multiplying the circulating currents in each device (the two qubits and the flux transformer) by the mutual inductance between qubit 1 (2) and the device. With picture 6.2 we note the following equations for the flux through qubit 1 and 2 induced by currents in the qubits and the flux transformer

$$\Delta\Phi_1 = I_1 M_{Q_1 Q_1} + I_T M_{Q_1 T} + I_2 M_{Q_1 Q_2} \quad (6.2)$$

$$\Delta\Phi_2 = I_2 M_{Q_2 Q_2} + I_T M_{Q_2 T} + I_1 M_{Q_2 Q_1}, \quad (6.3)$$

where the inductances are explained in table 6.1.

$M_{Q_1Q_1} = M_{Q_2Q_2} = M_{QQ}$:	self-inductance of the qubit
$M_{Q_1T} = M_{Q_2T} = M_{QT} = M_{TQ}$:	mutual inductance transformer-qubit
$M_{Q_1Q_2} \approx 0$:	mutual inductance between qubit 1 and qubit 2 (assumed to be small: no direct inductive coupling between the two qubits)

Table 6.1: Explanation of the several inductances introduced the circuit depicted in figure 6.2.

Introducing the screening flux $\Phi_S = \Delta\Phi_T$ and writing it in a similar form like equations (6.2) and (6.3) yields together with the equations for $\Delta\Phi_1 = \Phi_1$ and $\Delta\Phi_2 = \Phi_2$ (we introduced the abbreviations just for the sake of simplicity) the system of equations

$$\Phi_S = M_{TT}I_S + M_{TQ}I_1 + M_{TQ}I_2 \quad (6.4)$$

$$\Phi_1 = M_{QT}I_S + M_{QQ}I_1 \quad (6.5)$$

$$\Phi_2 = M_{QT}I_S + M_{QQ}I_2 \quad (6.6)$$

or in matrix form

$$\vec{\Phi} = \mathbf{M}\vec{I}$$

$$\begin{pmatrix} \Phi_S \\ \Phi_1 \\ \Phi_2 \end{pmatrix} = \begin{pmatrix} M_{TT} & M_{TQ} & M_{TQ} \\ M_{TQ} & M_{QQ} & 0 \\ M_{TQ} & 0 & M_{QQ} \end{pmatrix} \begin{pmatrix} I_S \\ I_1 \\ I_2 \end{pmatrix} \quad (6.7)$$

If no net flux is coupled into the transformer the superconducting loop will only respond to spatial variations of the magnetic field. This kind of configuration is called ‘‘gradiometer’’ [25]. We first evaluate the gradiometer case where $\Phi_S = 0$. Then equation (6.4) gives us an expression for I_S

$$I_S = -\frac{M_{TQ}}{M_{TT}}(I_1 + I_2) \quad (6.8)$$

which we might insert into (6.7) to reduce (6.7) to

$$\vec{\Phi}' = \mathbf{M}'\vec{I}'$$

$$\begin{pmatrix} \Phi_1 \\ \Phi_2 \end{pmatrix} = \begin{pmatrix} \left(M_{QQ} - \frac{M_{TQ}^2}{M_{TT}}\right) & -\frac{M_{TQ}^2}{M_{TT}} \\ -\frac{M_{TQ}^2}{M_{TT}} & \left(M_{QQ} - \frac{M_{TQ}^2}{M_{TT}}\right) \end{pmatrix} \begin{pmatrix} I_1 \\ I_2 \end{pmatrix} \quad (6.9)$$

$$E_{ind} = \vec{I}'^T \mathbf{M}' \vec{I}' \quad (6.10)$$

$$= \left(M_{QQ} - \frac{M_{TQ}^2}{M_{TT}}\right) (I_1^2 + I_2^2) - 2\frac{M_{TQ}^2}{M_{TT}} I_1 I_2. \quad (6.11)$$

The terms resulting from the off-diagonal elements of (6.9) can directly be identified as the interqubit coupling strength K

$$K = -2\frac{M_{TQ}^2}{M_{TT}} I_1 I_2 \quad (6.12)$$

which is symmetric regarding the circulating currents I_1 and I_2 in the qubits.

6.2.2 Tunable Josephson junction as a switch

The gauge invariant phase in fluxoid quantization is given by

$$\sum_i \gamma_i = \gamma = -2\pi \frac{\Phi_S}{\Phi_0} + 2n\pi, \quad (6.13)$$

where $\Phi_0 = h/(2e)$ is the magnetic flux quantum. If we insert γ into the Josephson relation [25] we get

$$I_S = I_c \sin \gamma = I_c \sin \left(-2\pi \frac{\Phi_S}{\Phi_0} \right). \quad (6.14)$$

Generally Φ_S is of the form

$$\Phi_S = -\frac{\Phi_0}{2\pi} \arcsin \frac{I_S}{I_c} \quad (6.15)$$

We now explicitly evaluate K for two different cases. **1)** If $|I_S/I_c| \ll 1$ then $\sin(x) \approx x \approx \arcsin(x)$ and similar to (6.8) the first equation of (6.7) gives us

$$I_S = -\frac{M_{TQ}}{M_{TT}^*} (I_1 + I_2), \text{ with } M_{TT}^* := M_{TT} + \frac{\Phi_0}{2\pi} \frac{1}{I_c} = M_{TT} + L_{kin}(0). \quad (6.16)$$

Then the same calculation as for $\Phi_S = 0$ yields

$$K = -2 \frac{M_{TQ}^2}{M_{TT}^*} I_1 I_2. \quad (6.17)$$

K is compared to the gradiometer case decreased because the self inductance M_{TT} of the flux transformer is increased by the kinetic inductance. **2)** The other case is determined by $|I_S/I_c| \gg 1$. If $z \in \mathbf{R}$ and $|z| \approx 1$ then $\arcsin z = -i \ln(iz + \sqrt{1-z^2})$ gives us ($\ln z = \ln \rho + i\varphi$)

$$\arcsin z = -i \ln(iz) \approx \frac{\pi}{2} + i \ln(z) \approx \frac{\pi}{2}. \quad (6.18)$$

From this simple analysis follows that we may express the screening flux as

$$\Phi_S = -\frac{\Phi_0}{2\pi} \arcsin \frac{I_S}{I_c} \approx -\frac{\Phi_0}{2\pi} \frac{\pi}{2} \frac{I_S}{|I_S|} = -\frac{\Phi_0}{2\pi} \frac{\pi}{2} \frac{I_S}{|I_c|}. \quad (6.19)$$

Overall we get

$$I_S = -\frac{M_{TQ}}{M_{TT} + \frac{\Phi_0}{4|I_c|}} (I_1 + I_2). \quad (6.20)$$

From this follows

$$K = -2 \frac{M_{TQ}^2}{M'_{TT}} I_1 I_2, \text{ with } M'_{TT} = M_{TT} + \frac{\Phi_0}{4|I_c|}. \quad (6.21)$$

By comparison of the two limits **1)** and **2)** we observe that for a given critical current of the junction the “renormalized” self inductance M'_{TT} of the flux transformer is slightly larger than M_{TT}^* . Therefore the coupling strength K between the two qubits is slightly larger if $I_S \ll I_c$. For typical values of I_c the term added to the self-inductance M_{TT} of the transformer loop is only slightly modified.

6.3 RSJ-model

We use the RSJ-model (resistively shunted Josephson junction) to calculate the fluctuations of the current between two points of the flux transformer loop sketched in figure 6.2. L is the geometric inductance of the loop, L_J is the Josephson inductance characterizing the Josephson contact and R is the shunt resistance. The correlation is given [53] by the fluctuation-

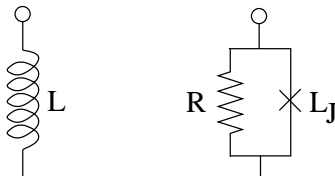


Figure 6.3: Equivalent circuit diagram of the flux transformer. The JoFET is modeled by a resistively shunted Josephson junction. We evaluate the current fluctuations between the two contacts.

dissipation theorem

$$\langle \delta I \delta I \rangle_\omega = \coth \left(\frac{\beta \hbar \omega}{c} \right) \hbar \omega \chi(\omega), \quad (6.22)$$

where $\chi(\omega)$ denotes the real part of the admittance which can easily be calculated from figure 6.3:

$$Y^{-1} = i\omega L + Z_{RSJ} \quad (6.23)$$

The total resistance and admittance of the shunt circuit evaluates to

$$Z_{RSJ} = \frac{i\omega L_J R}{R + i\omega L_J} \Rightarrow Y = \frac{R + i\omega L_J}{i\omega L(R + i\omega L_J) + i\omega L_J R}. \quad (6.24)$$

Multiplying with the complex conjugate and simplifying gives the real part:

$$\chi(\omega) = \text{Re } Y = \frac{L_J^2 R}{\omega^2 L^2 L_J^2 + R^2 (L + L_J)^2}. \quad (6.25)$$

With $\delta \Phi_q = M_{TQ} \delta I$

$$\langle \delta \Phi_q \delta \Phi_q \rangle_\omega = M_{TQ}^2 \frac{L_J^2 R}{\omega^2 L^2 L_J^2 + R^2 (L + L_J)^2} \omega \hbar \coth \left(\frac{1}{2} \beta \hbar \omega \right) \quad (6.26)$$

From $\epsilon = (\Phi_q - \frac{1}{2} \Phi_0) I_{circ}$ follows that $\delta \epsilon = 2 \delta \Phi_q I_{circ}$ (see [13]) which we can use to express the fluctuations of the energy levels of a qubit

$$\langle \delta \epsilon \delta \epsilon \rangle_\omega = \frac{4 I_{circ}^2 M_{TQ}^2 L_J^2 R}{\omega^2 L^2 L_J^2 + R^2 (L + L_J)^2} \omega \hbar \coth \left(\frac{1}{2} \beta \hbar \omega \right). \quad (6.27)$$

Here we define $J(\omega)$ for our environment

$$J(\omega) := \frac{\omega}{\hbar} \frac{4 I_{circ}^2 M_{TQ}^2 L_J^2 R}{\omega^2 L^2 L_J^2 + R^2 (L + L_J)^2}, \quad (6.28)$$

where

$$L_J = \frac{\Phi_0}{2\pi} \frac{1}{I_c} \quad (6.29)$$

is the Josephson inductance. One can immediately recognize that $J(\omega)$ resembles an ohmic spectral function with an intrinsic Drude cutoff. Therefore there is no need to introduce an artificial cutoff. Now we evaluate the typical size of the dimensionless parameter α which characterizes the strength of the dissipative effects [34] for a JoFET by inserting typical parameters. The normal resistance of a JoFET is around $R \approx 10 \Omega$, which we use as an estimate for the size of the shunt resistance in the RSJ model. The geometric inductance of the loop is $L \approx 1$ nH, the circulating current in the qubit is $I_{circ} \approx 100$ nA, the mutual inductance between the flux transformer and the qubit is $M_{TQ} \approx 100$ pH, the critical current of the Josephson junction is $I_c \approx 30 \mu\text{A}$ and the Josephson inductance is $L_J \approx 100$ nH. The dimensionless dissipation parameter α is determined by the slope of the spectral function $J(\omega)$ at low frequencies [13]

$$\alpha = \lim_{\omega \rightarrow 0} \frac{J(\omega)}{2\pi\omega}, \quad (6.30)$$

which can be taken as

$$\alpha = \frac{1}{2\pi} \frac{\partial J(\omega)}{\partial \omega} \quad (6.31)$$

at $\omega \approx 0$. Using this knowledge we may calculate α from (6.28):

$$\alpha = \frac{1}{2\pi} \frac{\partial J(\omega)}{\partial \omega} \Big|_{\omega \approx 0} \approx \frac{2I_{circ}^2 M_{TQ}^2 L_J^2}{\hbar\pi R(L + L_J)^2}. \quad (6.32)$$

Inserting the estimates which were given above we get

$$\alpha \approx 7 \cdot 10^{-6}. \quad (6.33)$$

This means that the dissipative effects should be weak and a JoFET might be a reasonable switch, e.g. for the flux transformer. From chapter 5.3 and figure 5.4 we found that $\alpha \approx 10^{-6}$ poses an upper bound for gate operations to be useful. Then errors occurring during the gate operation are small enough to be corrected. Therefore using a JoFET with (6.33) as a switch should introduce no new constraints to the design of coupled qubits. However the technical effort to build such a device is huge [54]. One drawback of JoFETs is that due to wide junctions with dimensions of around $w = 500$ nm vortices are possibly trapped [40]. If vortices are hopping between different pinning sites they cause 1/f noise [55]. One solution might be to employ stronger pinning so that vortices can be regarded as quasi static and therefore the effect of 1/f noise is reduced.

A different approach would be to construct another SQUID loop around the Josephson junction of the transformer loop to tune E_J and therefore switch the coupling on and off. This extra loop is easily fabricated and was proposed in [56]. Drawbacks of this type of switch are that even more fluxes are introduced and one might imagine that tuning the flux through a qubit might also modify the flux through the steering loop and vice versa. Another problem poses that the flux through the steering loop must exactly equal half a flux quantum while the JoFET is simply steered by a gate voltage.

Chapter 7

Conclusions

We presented a full analysis of the dynamics and decoherence properties of two solid state qubits coupled to each other via a generic type of Ising coupling and coupled, moreover, either to a common bath, or two independent baths.

In chapter 2 we exactly diagonalized the unperturbed Hamiltonian \mathbf{H}_{2qb} , depicted the behaviour of the transition frequencies (figures 3.2 and 3.3) between the energy levels, and in chapter 3 we investigated the effects of a weak symmetric driving in the energy bias ϵ . This work is directly related to experiments currently done in Delft [40] considering spectroscopy of inductively coupled flux qubits. In the case of two qubits with identical qubit parameters, (such as energy bias and transmission amplitude) coupling to one common bath, one can easily observe that in the singlet/triplet basis representation, the singlet part of the Hilbert space is a protected subspace where no transitions between singlet and triplet states can be mediated. (In chapter 2 the close and promising connection of this protected subspace with the theory of decoherence free subspaces (DFS) was already discussed.)

In chapter 4 we calculated the dynamics of the system and evaluate decoherence times. From the temperature dependence of the decoherence rates (figure 4.5), we conclude that both types of environments show a similar behaviour; however, in the case of one common bath two of the decoherence rates are zero, and the remaining ones are slightly larger than in the case of two distinct baths. This temperature dependence is also reflected in the characteristics of the so-called gate quality factors from quantum information theory, which are, in chapter 5, introduced as robust measures of the quality of a quantum logic operation. We illustrate that the gate quality factors depend linearly on α , as expected. The time resolved XOR operation (figures 5.5 and 5.6) again illustrates the difference between one common and two distinct baths, and moreover we observe that single-qubit decoherence effects during the XOR operation are weak.

We showed in chapter 5 that generally by decreasing the temperature of the environment, the decoherence effects can not be arbitrarily suppressed. (However, in the special case of the two-qubit operation needed when performing the XOR gate, due to the symmetries of the Hamiltonian, decoherence effects vanish when temperature is decreased. See figure 4.6 for reference.) Rather, to suppress them more, the system needs to be better decoupled from the dissipative environment. The time scales of the dynamics of the coupled two qubit system

are comparable to the time scales which were already observed in experiments and discussed in the literature [13]. Quantum coherent evolution and decoherence effects can nicely be illustrated by displaying the dynamics of the system. The question whether one common bath or two distinct baths are less destructive regarding quantum coherence can not be clearly answered. For low enough temperatures clearly coupling to one common bath yields better results. However, when the temperature is increased two distinct baths do better; in both temperature regimes, though, the gate quantifiers are only slightly different for both cases.

In chapter 6 the noise properties of a flux transformer with a tunable coupling are discussed. Therefore a Josephson field-effect transistor is inserted as a switch to turn on and off the inductive coupling between two flux qubits. It is shown that the noise properties of a JoFET which is fabricated by present day technology allow for using it as such a switch.

As a next step one should consider driving, to be able to observe and discuss Rabi oscillations in systems of two coupled qubits. It should be investigated, how the decoherence properties are modified if one adds more qubits to the system, and the theory of decoherence free subspaces should be applied to $\sigma_z^{(1)} \otimes \sigma_z^{(2)}$ type of coupling.

Chapter 8

Deutsche Zusammenfassung

Die Lösung einiger Probleme der klassischen Informationstheorie (z.B. Faktorisierung eines Produktes zweier Primzahlen, Suchalgorithmen) wird durch Algorithmen, die auf Quanten-Bits (“Qubits”) arbeiten, stark (exponentiell im Falle des Faktorisierungsalgorithmus) beschleunigt. Durch diesen enormen Zeitgewinn, z.B. bei Faktorisierungsalgorithmen, die für kryptographische Anwendungen von sehr großem Interesse sind, ist die physikalische Realisierung von “Quanten-Computern” zu einem sich extrem schnell entwickelnden Feld der Physik geworden. Die Erkenntnisse über die Manipulation und Dekohärenz offener Quantensysteme aber, die beim Studium von Qubits gewonnen wird, ist von grundsätzlichem Interesse für viele physikalische Fragestellungen.

Es wurden bereits verschiedene Implementierungen dieser Bits, die quantenmechanischen Effekten gehorchen, vorgeschlagen. Dazu zählen z.B. Atome in Ionenfallen oder Moleküle in einem Kernspinresonanz-Aufbau (NMR). Mit NMR-Qubits wurden bereits einfache Algorithmen implementiert [6, 57], allerdings sind Systeme mit mehr als etwa zehn Qubits praktisch nicht realisierbar, da sehr komplizierte Molekülstrukturen benötigt würden. Der Vorteil von Quantenbits, die in Festkörpern realisiert sind ist, daß sich die Anzahl der Quantenbits sehr leicht hochskalieren läßt. Als Nachteil wird allerdings die kurze Dekohärenzzeit, aufgrund der vielen internen Freiheitsgrade eines Festkörpersystems, angesehen.

Die vorliegende Arbeit quantifiziert die Dekohärenzzeiten gekoppelter Festkörper-Quantenbits mit Ising-Kopplung. Dazu wird in Kapitel 4 mittels des Bloch-Redfield Formalismus die Dynamik gekoppelter Festkörper-Quantenbits untersucht. Verschiedene dissipative Umgebungen werden durch Kopplung der beiden Quantenbits an ein gemeinsames oder eines von zwei unkorrelierten harmonischen Oszillator-Bädern modelliert. Die Dekohärenzzeiten liegen für typische Parameter, in Übereinstimmung mit experimentellen Ergebnissen, im Bereich weniger μs . Die aus dem Bloch-Redfield Formalismus gewonnenen Informationen über die Dynamik des Systems werden ausführlich diskutiert und beide Dekohärenzmechanismen, Dephasierung und Relaxation werden demonstriert.

Die Quanten-Informationstheorie liefert mit den Gatter-Qualitätsfaktoren [24] ein Maß, mit dem die Qualität einer Quanten-Logik Operation bzw. eines Gatters bewertet werden kann. Für supraleitende Fluß-Qubits [13] ergibt sich, daß bei einer Temperatur von $T = 10$ mK der Parameter α , welcher die Stärke der dissipativen Effekte charakterisiert, nicht größer als

$\alpha \approx 10^{-6}$ werden darf, um einen Grad der Fehlerfreiheit zu erreichen, der es erlaubt unter Berücksichtigung von Fehlerkorrektur-Schemata eine große Anzahl von Quanten-Logik Operationen auszuführen.

Durch den Vergleich der Gatter-Qualitätsfaktoren für den Fall eines gemeinsamen oder zweier unkorrelierter Bäder lässt sich beurteilen, welche dissipativen Umgebungen die Eigenschaften eines Systems am stärksten (negativ) beeinflussen. Für niedrige Temperaturen ($T < 0.05$ K, Parameter aus Abbildung 5.2) führt eindeutig der Fall eines gemeinsamen Bades zu besseren Gatter-Qualitätsfaktoren, während für höhere Temperaturen ($T = 1$ K) der Fall zweier Bäder im Bezug auf die Gatter-Qualitätsfaktoren vorteilhafter ist. Die Vorteile eines Kopplungsterms zwischen den beiden Qubits, der die Form $\sigma_z^{(1)} \otimes \sigma_z^{(2)}$ hat, wurden in Kapitel 4 aufgezeigt.

Mittels eines Fluß-Transformators können supraleitende Fluß-Qubits induktiv gekoppelt werden. Um die Kopplung der beiden Fluß-Qubits, die jeweils induktiv an den Fluß-Transformator aber nicht aneinander koppeln, an- und abschalten zu können, wird ein Schalter benötigt. Die Eignung eines Josephson Feldeffekt-Transistors als Schalter wird durch Untersuchung der Rauscheigenschaften eines JoFETs in Kapitel 6 nachgewiesen.

Acknowledgements

At the end of the diploma thesis, I would like to thank a lot of people for making all this possible.

Prof. Dr. Jan von Delft for giving me the opportunity to join his group in Munich and for interesting discussions.

Dr. Frank K. Wilhelm for his advice and support in the last year; it was a great pleasure to work for and with you.

Prof. Dr. Peter Herzog and Prof. Dr. Hartmut Monien from the University of Bonn for their official support.

All people at the Chair for Theoretical Condensed Matter Physics (at LMU in Munich): Rong, Laszlo, Silvia, Dominique, Corinna, Henryk, Michael, Udo and Stéphane; especially the discussions with Laszlo, Michael, Dominique, Henryk and Udo have been very helpful for me.

The superconducting circuits group of Prof. Terry Orlando at MIT in Cambridge: David Berns, Bill Kaminsky, Lin Tian, Bhuwan Singh and all others for a lot of insight into qubit experiments, stimulating discussions and a great stay at MIT.

H. Majer (TU Delft), P. Baars (U Hamburg) for experimental data and a lot of information about experimental realized coupled flux qubits and JoFET's.

Dr. Ulrich Zülicke, Dr. Achim Rosch (all TU Karlsruhe) and Dr. Igor Goychuk (University of Augsburg) for fruitful and helpful discussions.

Silvia for her constant support and understanding. My parents for their support during my studies; Udo Hartmann for a lot of stimulating discussions and fun.

My friends Uwe (RWTH Aachen), Oliver, Gregor, Ralf, Florian, Teresa (Uni Bonn), Oliver (FH Köln), Guido, Thomas (Uni Köln) and all the others for not forgetting me in Bavaria.

The Center for NanoScience (CeNS) for the organizational help and the posters; the Army Research Office (ARO) for financial support (Contract-No. P-43385-PH-QC: *Realistic theory of solid-state qubits*) and DAAD for financing my stay at the Massachusetts Institute of Technology (supported through contract-No. DAAD/NSF D/0104619).

Appendix A

Eigenvalues and eigenstates of the two qubit Hamiltonian

We diagonalize the unperturbed Hamiltonian (2.14) to get the eigenenergies and eigenstates. Because the singlet part of the Hamiltonian is already diagonal we only have to diagonalize the upper three by three matrix. In this case one can simply apply Cardano's formula

$$y = \left(-q + \sqrt{q^2 + p^3}\right)^{\frac{1}{3}} + \left(-q - \sqrt{q^2 + p^3}\right)^{\frac{1}{3}} \quad (\text{A.1})$$

to find the solutions of $y^3 + 3py + 2q = 0$, with

$$2q = \frac{2b^3}{27a^3} - \frac{bc}{3a^2} + \frac{d}{a} \text{ and } 3p = \frac{3ac - b^2}{3a^2}. \quad (\text{A.2})$$

And therefore after applying the simple transformation $y = x + b/(3a)$ one finds the solutions of the general third order equation $ax^3 + bx^2 + cx + d = 0$. The eigenenergies of (2.14) read

$$E_1 = \frac{1}{2}K \quad (\text{A.3})$$

$$E_2 = \rho^{\frac{1}{3}} \left(-\cos\left(\frac{1}{3}\Phi\right) - \sqrt{3}\sin\left(\frac{1}{3}\Phi\right) \right) - \frac{1}{6}K \quad (\text{A.4})$$

$$E_3 = 2\rho^{\frac{1}{3}} \cos\left(\frac{1}{3}\Phi\right) - \frac{1}{6}K \quad (\text{A.5})$$

$$E_4 = \rho^{\frac{1}{3}} \left(-\cos\left(\frac{1}{3}\Phi\right) + \sqrt{3}\sin\left(\frac{1}{3}\Phi\right) \right) - \frac{1}{6}K \quad (\text{A.6})$$

and the corresponding eigenstates in the singlet/triplet basis read

$$\begin{aligned} |E1\rangle &= \begin{pmatrix} 0 \\ 0 \\ 0 \\ 1 \end{pmatrix} & |E2\rangle &= \frac{|k_2||\eta|}{k_3} \begin{pmatrix} \frac{3k_1}{k_2} \\ \frac{k_1}{\eta} \\ 3 \\ 0 \end{pmatrix} \\ |E3\rangle &= \frac{|\eta|^2}{k_6} \begin{pmatrix} 9 \\ -3\frac{k_4}{\eta} \\ \frac{k_5}{\eta^2} \\ 0 \end{pmatrix} & |E4\rangle &= \frac{|\eta|^2}{k_9} \begin{pmatrix} -\frac{k_7}{\eta^2} \\ 3\frac{k_8}{\eta} \\ 9 \\ 0 \end{pmatrix}. \end{aligned} \quad (\text{A.7})$$

Where we introduced the following abbreviations:

$$q = -\frac{1}{27}K^3 + \frac{1}{12}K\epsilon^2 - \frac{1}{12}K\eta^2 \quad (\text{A.8})$$

$$p = -\frac{3\epsilon^2 - 6\eta^2 - 4K^2}{36} \quad (\text{A.9})$$

$$\rho = \sqrt{q^2 + \left| q^2 + \left(-\frac{1}{12}\epsilon^2 - \frac{1}{9}K^2 - \frac{1}{6}\eta^2 \right) \right|} \quad (\text{A.10})$$

$$\Phi = \arccos\left(-\frac{q}{\rho}\right) \quad (\text{A.11})$$

$$k_1 = -2K + 3\epsilon + 6\rho^{\frac{1}{3}} \cos\left(\frac{1}{3}\Phi\right) + 6\rho^{\frac{1}{3}} \sin\left(\frac{1}{3}\Phi\right) \sqrt{3} \quad (\text{A.12})$$

$$k_2 = -2K - 3\epsilon + 6\rho^{\frac{1}{3}} \cos\left(\frac{1}{3}\Phi\right) + 6\rho^{\frac{1}{3}} \sin\left(\frac{1}{3}\Phi\right) \sqrt{3} \quad (\text{A.13})$$

$$k_3 = \sqrt{9|k_1|^2|\eta|^2 + |k_1|^2|k_2|^2 + 9|k_2|^2|\eta|^2} \quad (\text{A.14})$$

$$k_4 = 3\epsilon + 2K + 12\rho^{\frac{1}{3}} \cos\left(\frac{1}{3}\Phi\right) \quad (\text{A.15})$$

$$k_5 = -9\eta^2 - 12K\epsilon - 8K^2 - 24K\rho^{\frac{1}{3}} \cos\left(\frac{1}{3}\Phi\right) + 36\rho^{\frac{1}{3}} \cos\left(\frac{1}{3}\Phi\right) \epsilon + 144\rho^{\frac{2}{3}} \cos^2\left(\frac{1}{3}\Phi\right) \quad (\text{A.16})$$

$$k_6 = \sqrt{81|\eta|^4 + 9|k_4|^2|\eta|^2 + |k_5|^2} \quad (\text{A.17})$$

$$k_7 = 8K^2 - 12K\epsilon - 12K\rho^{\frac{1}{3}} \cos\left(\frac{1}{3}\Phi\right) + 12K\rho^{\frac{1}{3}} \sin\left(\frac{1}{3}\Phi\right) \sqrt{3} - 18\rho^{\frac{1}{3}} \cos\left(\frac{1}{3}\Phi\right) \epsilon - 36\rho^{\frac{2}{3}} - 72\rho^{\frac{2}{3}} \sin^2\left(\frac{1}{3}\Phi\right) + 72\rho^{\frac{2}{3}} \cos\left(\frac{1}{3}\Phi\right) \sin\left(\frac{1}{3}\Phi\right) \sqrt{3} + 18\rho^{\frac{1}{3}} \sin\left(\frac{1}{3}\Phi\right) \epsilon + 9\eta^2 \quad (\text{A.18})$$

$$k_8 = -2K + 3\epsilon + 6\rho^{\frac{1}{3}} \cos\left(\frac{1}{3}\Phi\right) - 6\rho^{\frac{1}{3}} \sqrt{3} \sin\left(\frac{1}{3}\Phi\right) \quad (\text{A.19})$$

$$k_9 = \sqrt{|k_7|^2 + 9|k_8|^2|\eta|^2 + 81|\eta|^4}. \quad (\text{A.20})$$

Figure 2.6 depicts the eigenenergies of (2.13) for several parameter sets. Figure 2.7 illustrates of which singlet/triplet states the eigenstates consist for different qubit parameters.

Appendix B

Matrix representation of σ_z

In Bloch Redfield formalism the matrix elements of σ_z with respect to the eigenbasis of the unperturbed Hamiltonian are used. For convenience, here the analytic results for the matrix elements are given. For $\sigma_z^{(1)}$ we receive

$$\sigma_{z,11}^{(1)} = 0, \sigma_{z,12}^{(1)} = \frac{|k_2||\eta|k_1}{k_3\eta}, \sigma_{z,13}^{(1)} = -\frac{|\eta|^2 3k_4}{k_6\eta}, \sigma_{z,14}^{(1)} = \frac{3|\eta|^2 k_8}{k_9\eta}, \quad (\text{B.1})$$

$$\sigma_{z,21}^{(1)} = \frac{|k_2||\eta|k_1}{k_3\eta}, \sigma_{z,22}^{(1)} = \frac{|k_2|^2|\eta|^2}{k_3^2} \left(9\frac{k_1^2}{k_2^2} - 9 \right), \sigma_{z,23}^{(1)} = \frac{|k_2||\eta|^3}{k_3k_6} \left(27\frac{k_1}{k_2} - 3\frac{k_5}{\eta^2} \right), \quad (\text{B.2})$$

$$\sigma_{z,24}^{(1)} = \frac{|k_2||\eta|^3}{k_3k_9} \left(-\frac{3k_1k_7}{k_2\eta^2} - 27 \right), \sigma_{z,31}^{(1)} = -\frac{3|\eta|^2 k_4}{k_6\eta}, \sigma_{z,32}^{(1)} = \frac{|k_2||\eta|^3}{k_6k_3} \left(27\frac{k_1}{k_2} - 3\frac{k_5}{\eta^2} \right), \quad (\text{B.3})$$

$$\sigma_{z,33}^{(1)} = \frac{|\eta|^4}{k_6^2} \left(81 - \frac{k_5^2}{\eta^4} \right), \sigma_{z,34}^{(1)} = \frac{|\eta|^4}{k_6k_9} \left(-9\frac{k_7}{\eta^2} - 9\frac{k_5}{\eta^2} \right), \sigma_{z,41}^{(1)} = \frac{3|\eta|^2 k_8}{k_9\eta} \quad (\text{B.4})$$

$$\sigma_{z,42}^{(1)} = \frac{|\eta|^3|k_2|}{k_9k_3} \left(-3\frac{k_1k_7}{k_2\eta^2} - 27 \right), \sigma_{z,43}^{(1)} = \frac{|\eta|^4}{k_6k_9} \left(-9\frac{k_7}{\eta^2} - 9\frac{k_5}{\eta^2} \right), \quad (\text{B.5})$$

$$\sigma_{z,44}^{(1)} = \frac{|\eta|^4}{k_9^2} \left(\frac{k_7^2}{\eta^4} - 81 \right) \quad (\text{B.6})$$

and for $\sigma_z^{(2)}$

$$\sigma_{z,11}^{(2)} = 0, \sigma_{z,12}^{(2)} = -\frac{k_1|k_2||\eta|}{\eta k_3}, \sigma_{z,13}^{(2)} = \frac{3|\eta|^2 k_4}{k_6\eta}, \sigma_{z,14}^{(2)} = -\frac{3|\eta|^2 k_8}{k_9\eta}, \sigma_{z,21}^{(2)} = -\frac{|k_2||\eta|k_1}{k_3\eta}, \quad (\text{B.7})$$

$$\sigma_{z,22}^{(2)} = \frac{|k_2|^2|\eta|^2}{k_3^2} \left(9\frac{k_1^2}{k_2^2} - 9 \right), \sigma_{z,23}^{(2)} = \frac{|k_2||\eta|^3}{k_3k_6} \left(27\frac{k_1}{k_2} - 3\frac{k_5}{\eta^2} \right), \quad (\text{B.8})$$

$$\sigma_{z,24}^{(2)} = \frac{|k_2||\eta|^3}{k_3k_9} \left(-\frac{3k_1k_7}{k_2\eta^2} - 27 \right), \sigma_{z,31}^{(2)} = \frac{3|\eta|^2 k_4}{k_6\eta}, \sigma_{z,32}^{(2)} = \frac{|k_2||\eta|^3}{k_6k_3} \left(27\frac{k_1}{k_2} - 3\frac{k_5}{\eta^2} \right), \quad (\text{B.9})$$

$$\sigma_{z,33}^{(2)} = \frac{|\eta|^4}{k_6^2} \left(81 - \frac{k_5^2}{\eta^4} \right), \sigma_{z,34}^{(2)} = \frac{|\eta|^4}{k_6k_9} \left(-9\frac{k_7}{\eta^2} - 9\frac{k_5}{\eta^2} \right), \sigma_{z,41}^{(2)} = -\frac{3|\eta|^2 k_8}{k_9\eta}, \quad (\text{B.10})$$

$$\sigma_{z,42}^{(2)} = \frac{|\eta|^3|k_2|}{k_9k_3} \left(-3\frac{k_1k_7}{k_2\eta^2} - 27 \right), \sigma_{z,43}^{(2)} = \frac{|\eta|^4}{k_6k_9} \left(-9\frac{k_7}{\eta^2} - 9\frac{k_5}{\eta^2} \right), \quad (\text{B.11})$$

$$\sigma_{z,44}^{(2)} = \frac{|\eta|^4}{k_9^2} \left(\frac{k_7^2}{\eta^4} - 81 \right). \quad (\text{B.12})$$

Appendix C

Calculation of the rates

C.1 Two qubits coupled to two distinct baths

Here we evaluate the Golden Rule expressions for the rates $\Gamma_{\ell mnk}^{(+)}$ and $\Gamma_{\ell mnk}^{(-)}$ defined in (4.5)

$$\Gamma_{\ell mnk}^{(+)} = \hbar^{-2} \int_0^\infty dt e^{-i\omega_{nk}t} \langle \tilde{H}_{I,\ell m}(t) \tilde{H}_{I,nk}(0) \rangle \quad (\text{C.1})$$

and (4.6). Here $\tilde{H}_I(t) = \exp(iH_B t/\hbar) H_I \exp(-iH_B t/\hbar)$ denotes the interaction in the interaction picture. The interaction part of the Hamiltonian (2.8) is

$$H_I = \frac{1}{2} \hat{\sigma}_z^{(1)} \otimes \hat{X}^{(1)} + \frac{1}{2} \hat{\sigma}_z^{(2)} \otimes \hat{X}^{(2)}, \quad (\text{C.2})$$

where $X_j = \zeta \sum_i \lambda_i x_i$ ($j = 1, 2$) describes the coupling to the bath via position coordinate of the harmonic oscillator bath. In the case of two qubits each coupling to a distinct uncorrelated bath, the resulting bath Hamiltonian is the sum of the two Hamiltonians

$$H_B = H_{B_1} + H_{B_2}. \quad (\text{C.3})$$

We explicitly calculate only the rates $\Gamma_{\ell mnk}^{(+)}$ because calculation of $\Gamma_{\ell mnk}^{(-)}$ is easily done in a completely analogous manner. Inserting (C.2) into (C.1) we receive

$$\begin{aligned} \Gamma_{\ell mnk}^{(+)} &= \frac{1}{4\hbar^2} \int_0^\infty dt e^{-i\omega_{nk}t} \langle e^{i(H_{B_1} + H_{B_2})t/\hbar} \times \\ &\quad \times \left(\sigma_{z,\ell m}^{(1)} \otimes \sum_j \lambda_j x_j^{(1)} + \sigma_{z,\ell m}^{(2)} \otimes \sum_s \mu_s x_s^{(2)} \right) e^{-i(H_{B_1} + H_{B_2})t/\hbar} \times \\ &\quad \times \left(\sigma_{z,nk}^{(1)} \otimes \sum_\alpha \lambda_\alpha x_\alpha^{(1)} + \sigma_{z,nk}^{(2)} \otimes \sum_\beta \mu_\beta x_\beta^{(2)} \right) \rangle. \end{aligned} \quad (\text{C.4})$$

In the following, we sum over the indices j , s , α and β .

$$\begin{aligned} \Gamma_{\ell mnk}^{(+)} &= \frac{1}{4\hbar^2} \int_0^\infty dt e^{-i\omega_{nk}t} \left[\sigma_{z,\ell m}^{(1)} \sigma_{z,nk}^{(1)} \langle e^{i(H_{B_1} + H_{B_2})t/\hbar} \lambda_j x_j^{(1)} e^{-i(H_{B_1} + H_{B_2})t/\hbar} \lambda_\alpha x_\alpha^{(1)} \rangle + \right. \\ &\quad + \sigma_{z,\ell m}^{(1)} \sigma_{z,nk}^{(2)} \langle e^{i(H_{B_1} + H_{B_2})t/\hbar} \lambda_j x_j^{(1)} e^{-i(H_{B_1} + H_{B_2})t/\hbar} \lambda_\beta x_\beta^{(2)} \rangle + \\ &\quad + \sigma_{z,\ell m}^{(2)} \sigma_{z,nk}^{(1)} \langle e^{i(H_{B_1} + H_{B_2})t/\hbar} \mu_s x_s^{(2)} e^{-i(H_{B_1} + H_{B_2})t/\hbar} \lambda_\alpha x_\alpha^{(1)} \rangle + \\ &\quad \left. + \sigma_{z,\ell m}^{(2)} \sigma_{z,nk}^{(2)} \langle e^{iH_{B_2}t/\hbar} \mu_s x_s^{(2)} e^{-iH_{B_2}t/\hbar} \mu_\beta x_\beta^{(2)} \rangle \right] \end{aligned} \quad (\text{C.5})$$

Now we rewrite the harmonic oscillator Hamiltonian as $\mathbf{H}_{B_j} = \sum_i (\hat{n}_i + 1/2)\hbar\omega^{(j)}$ ($j = 1, 2$) in terms of annihilation and creation operators, express the position operator as $\hat{X} = \sqrt{\hbar/(2m\omega)}(\hat{a} + \hat{a}^\dagger)$ and trace out over the bath degrees of freedom. Then only the terms acting on the same bath survive, because if we denote the oscillator states of the two distinct baths with f_1 and f_2 then clearly $\langle f_1 \otimes f_2 | \hat{a}_j^{(1)\dagger} \hat{a}_j^{(2)} | f_1 \otimes f_2 \rangle = 0$ holds. Moreover we can deduce that $\langle f_1 \otimes f_2 | \hat{a}_j^{(1)\dagger} \hat{a}_\alpha^{(1)} | f_1 \otimes f_2 \rangle = 1$ only holds for $j = \alpha$. Therefore C.5 simplifies to

$$\Gamma_{\ell mnk}^{(+)} = \frac{1}{4\hbar^2} \int_0^\infty dt e^{-i\omega_{nk}t} \left[\sigma_{z,\ell m}^{(1)} \sigma_{z,nk}^{(1)} \langle e^{iH_{B_1}t/\hbar} \lambda_j x_j^{(1)} e^{-iH_{B_1}t/\hbar} \lambda_\alpha x_\alpha^{(1)} \rangle + \sigma_{z,\ell m}^{(2)} \sigma_{z,nk}^{(2)} \langle e^{iH_{B_2}t/\hbar} \mu_s x_s^{(2)} e^{-iH_{B_2}t/\hbar} \mu_\beta x_\beta^{(2)} \rangle \right] \quad (\text{C.6})$$

$$= \frac{1}{4\hbar^2} \int_0^\infty dt e^{-i\omega_{nk}t} \left(\sigma_{z,\ell m}^{(1)} \sigma_{z,nk}^{(1)} \frac{1}{Z} \sum_{f_1} \left[(f_1 + 1) e^{-\beta(f_1 + \frac{1}{2})\hbar\omega^{(1)}} e^{-i\omega^{(1)}t} + f_1 e^{-\beta(f_1 + \frac{1}{2})\hbar\omega^{(1)}} e^{i\omega^{(1)}t} \right] e^{-\beta[(f_1 + \frac{1}{2})\hbar\omega^{(1)} + (f_2 + \frac{1}{2})\hbar\omega^{(2)}]} + \sigma_{z,\ell m}^{(2)} \sigma_{z,nk}^{(2)} \frac{1}{Z} \sum_{f_2} \left[(f_2 + 1) e^{-\beta(f_2 + \frac{1}{2})\hbar\omega^{(2)}} e^{-i\omega^{(2)}t} + f_2 e^{-\beta(f_2 + \frac{1}{2})\hbar\omega^{(2)}} e^{i\omega^{(2)}t} \right] e^{-\beta[(f_1 + \frac{1}{2})\hbar\omega^{(1)} + (f_2 + \frac{1}{2})\hbar\omega^{(2)}]} \right) \quad (\text{C.7})$$

To trace out the bath degrees of freedom we need to evaluate the partition function

$$Z = \text{tr} \left[e^{-\beta(H_{B_1} + H_{B_2})} \right] \quad (\text{C.8})$$

$$= \sum_{f_1, f_2} \langle f_1 \otimes f_2 | e^{-\beta((\hat{n}_{f_1} + \frac{1}{2})\hbar\omega^{(1)} + (\hat{n}_{f_2} + \frac{1}{2})\hbar\omega^{(2)})} | f_1 \otimes f_2 \rangle \quad (\text{C.9})$$

$$= \sum_{f_1, f_2} e^{-\beta(n_{f_1} + \frac{1}{2})\hbar\omega^{(1)}} e^{-\beta(n_{f_2} + \frac{1}{2})\hbar\omega^{(2)}} = \sum_{f_1, f_2} \frac{e^{-\frac{1}{2}\beta\hbar\omega^{(1)}}}{1 - e^{-\beta\hbar\omega^{(1)}}} \frac{e^{-\frac{1}{2}\beta\hbar\omega^{(2)}}}{1 - e^{-\beta\hbar\omega^{(2)}}}. \quad (\text{C.10})$$

We may treat $J(\omega)$ as a continuous function because of the dense spectrum of the environmental degrees of freedom in the solid state device [32]. Therefore we might replace the sum over the eigenfrequencies by an integral. Inserting this and the partition function into (C.7) we get

$$\Gamma_{\ell mnk}^{(+)} = \frac{1}{4\hbar^2} \int_0^\infty dt e^{-i\omega_{nk}t} \left[\sigma_{z,\ell m}^{(1)} \sigma_{z,nk}^{(1)} \int_0^\infty d\omega^{(1)} J_1(\omega^{(1)}) (\cos(\omega^{(1)}t)) \left[\frac{2e^{-\beta\hbar\omega^{(1)}}}{1 - e^{-\beta\hbar\omega^{(1)}}} \right] + \cos(\omega^{(1)}t) - i \sin(\omega^{(1)}t) \right] + \sigma_{z,\ell m}^{(2)} \sigma_{z,nk}^{(2)} \int_0^\infty d\omega^{(2)} J_2(\omega^{(2)}) (\cos(\omega^{(2)}t)) \times \left[\frac{2e^{-\beta\hbar\omega^{(2)}}}{1 - e^{-\beta\hbar\omega^{(2)}}} \right] + \cos(\omega^{(2)}t) - i \sin(\omega^{(2)}t) \right]. \quad (\text{C.11})$$

With some simple calculus this can be expressed as

$$\Gamma_{\ell mnk}^{(+)} = \frac{1}{4\hbar^2} \int_0^\infty dt e^{-i\omega_{nk}t} \left[\sigma_{z,\ell m}^{(1)} \sigma_{z,nk}^{(1)} \frac{\hbar}{\pi} \int_0^\infty d\omega J_1(\omega) \left(\coth \left(\frac{\hbar\omega}{2k_B T} \right) \cos(\omega t) - i \sin(\omega t) \right) + \right.$$

$$+ \sigma_{z,lm}^{(2)} \sigma_{z,nk}^{(2)} \frac{\hbar}{\pi} \int_0^\infty d\omega J_2(\omega) \left(\coth\left(\frac{\hbar\omega}{2k_B T}\right) \cos(\omega t) - i \sin(\omega t) \right) \Big]. \quad (\text{C.12})$$

One might now swap the t and ω integration

$$\begin{aligned} \Gamma_{\ell mnk}^{(+)} &= \frac{1}{4\pi\hbar^2} \sigma_{z,lm}^{(1)} \sigma_{z,nk}^{(1)} \int_0^\infty d\omega \hbar J_1(\omega) \left[\int_0^\infty dt e^{-i\omega_{nk}t} (\coth(\beta\hbar\omega/2) \cos(\omega t) - i \sin(\omega t)) \right] + \\ &+ \sigma_{z,lm}^{(2)} \sigma_{z,nk}^{(2)} \frac{1}{4\pi\hbar^2} \int_0^\infty d\omega \hbar J_2(\omega) \left[\int_0^\infty dt e^{-i\omega_{nk}t} (\coth(\beta\hbar\omega/2) \cos(\omega t) - i \sin(\omega t)) \right] \end{aligned} \quad (\text{C.13})$$

and evaluate the time integrals

$$\begin{aligned} \int_0^\infty dt e^{-i\omega_{nk}t} \cos(\omega t) &= \frac{1}{2} \int_0^\infty dt e^{-i(\omega_{nk}-\omega)t} + \frac{1}{2} \int_0^\infty dt e^{-i(\omega_{nk}+\omega)t} \\ &= \lim_{\epsilon \rightarrow 0} \frac{1}{2} \int_0^\infty dt \left[e^{-i(\omega_{nk}-\omega)t} e^{-\epsilon t} + e^{-i(\omega_{nk}+\omega)t} e^{-\epsilon t} \right] \end{aligned} \quad (\text{C.14})$$

$$= \frac{1}{2} \lim_{\epsilon \rightarrow 0} \left[\frac{e^{-i(\omega_{nk}-\omega)t} e^{-\epsilon t}}{-i(\omega_{nk}-\omega) - \epsilon} + \frac{e^{-i(\omega_{nk}+\omega)t} e^{-\epsilon t}}{-i(\omega_{nk}+\omega) - \epsilon} \right]_0^\infty \quad (\text{C.15})$$

$$= iP \left(\frac{\omega_{nk}}{\omega^2 - \omega_{nk}^2} \right) + \frac{\pi}{2} (\delta(\omega - \omega_{nk}) + \delta(\omega + \omega_{nk})) \quad (\text{C.16})$$

correspondingly the second term gives

$$i \int_0^\infty dt e^{-i\omega_{nk}t} \sin(\omega t) = iP \left(\frac{\omega_{nk}}{\omega^2 - \omega_{nk}^2} \right) + \frac{\pi}{2} (\delta(\omega - \omega_{nk}) - \delta(\omega + \omega_{nk})). \quad (\text{C.17})$$

Note that the fact that we integrated over the upper half of the complex plane also affects the frequency integrals, because we interchanged the t and ω integration in equation (C.13). This is important when calculating the renormalization effects. Thus we may rewrite (C.13) as

$$\begin{aligned} \Gamma_{\ell mnk}^{(+)} &= i \frac{1}{4\hbar\pi} \sigma_{z,lm}^{(1)} \sigma_{z,nk}^{(1)} \int_0^\infty d\omega J_1(\omega) \coth(\beta\hbar\omega/2) \frac{\omega_{nk}}{\omega^2 - \omega_{nk}^2} + \\ &+ \frac{1}{8\hbar} \sigma_{z,lm}^{(1)} \sigma_{z,nk}^{(1)} \int_0^\infty J_1(\omega) \coth(\beta\hbar\omega/2) \delta(\omega - \omega_{nk}) - \\ &- \frac{i}{4\hbar\pi} \sigma_{z,lm}^{(1)} \sigma_{z,nk}^{(1)} \int_0^\infty d\omega J_1(\omega) \frac{\omega}{\omega^2 - \omega_{nk}^2} - \\ &- \frac{1}{8\hbar} \sigma_{z,lm}^{(1)} \sigma_{z,nk}^{(1)} \int_0^\infty J_1(\omega) d\omega \delta(\omega - \omega_{nk}) + \\ &+ (1 \leftrightarrow 2). \end{aligned} \quad (\text{C.18})$$

The second term needs special treatment if $\omega_{nk} = 0$. In this case we may write

$$I_2 = \int_{-\infty}^{\infty} J(\omega) \coth(\beta\hbar\omega/2) \delta(\omega - \omega_{nk}) d\omega \quad (\text{C.19})$$

and the first term of the Taylor-series for \coth gives (only first order, all other terms vanish fast for $\omega_{nk} \rightarrow 0$)

$$I_2 = \lim_{\omega_{nk} \rightarrow 0} J(\omega_{nk}) \frac{1}{\frac{1}{2}\beta\hbar\omega_{nk}}. \quad (\text{C.20})$$

Therefore we receive for $\omega_{nk} \rightarrow 0$

$$\begin{aligned} I_2 &= \lim_{\epsilon \rightarrow 0} \left[J(\omega_{nk} + i\epsilon) \frac{2}{\beta\hbar\omega_{nk} + i\beta\hbar\epsilon} \right] \\ &= \lim_{\omega_{nk} \rightarrow 0} J(\omega_{nk}) \frac{2}{\beta\hbar} \left[P(1/\omega_{nk}) - i\pi\delta(\omega_{nk}) \right] \\ &= \frac{2}{\beta\hbar} \lim_{\omega_{nk} \rightarrow 0} \frac{J(\omega_{nk})}{\omega_{nk}} =: \frac{2}{\beta\hbar} \alpha \end{aligned} \quad (\text{C.21})$$

where P denotes the principal value of $1/\omega_{nk}$. The δ -term vanishes because ω_{nk} we consider the limit such that ω_{nk} is not exactly zero. α is the usual parameter characterizing the strength of the dissipative effects. Quoting all calculations done in the preceding lines we may write the rates as

$$\begin{aligned} \Gamma_{\ell mnk}^{(+)} &= \frac{1}{8\hbar} \left[\sigma_{z,\ell m}^{(1)} \sigma_{z,nk}^{(1)} J_1(\omega_{nk}) + \sigma_{z,\ell m}^{(2)} \sigma_{z,nk}^{(2)} J_2(\omega_{nk}) \right] (\coth(\beta\hbar\omega_{nk}/2) - 1) + \\ &+ \frac{i}{4\pi\hbar} \left[\sigma_{z,\ell m}^{(2)} \sigma_{z,nk}^{(2)} \int_0^{\infty} d\omega \frac{J_2(\omega)}{\omega^2 - \omega_{nk}^2} (\coth(\beta\hbar\omega/2)\omega_{nk} - \omega) + \right. \\ &\left. + \sigma_{z,\ell m}^{(1)} \sigma_{z,nk}^{(1)} \int_0^{\infty} d\omega \frac{J_1(\omega)}{\omega^2 - \omega_{nk}^2} (\coth(\beta\hbar\omega/2)\omega_{nk} - \omega) \right] \end{aligned} \quad (\text{C.22})$$

and (we do not explicitly calculate the rate $\Gamma_{\ell mnk}^{(-)}$ because this is done completely analogous to the rate $\Gamma_{\ell mnk}^{(+)}$)

$$\begin{aligned} \Gamma_{\ell mnk}^{(-)} &= \frac{1}{8\hbar} \left[\sigma_{z,\ell m}^{(1)} \sigma_{z,nk}^{(1)} J_1(\omega_{\ell m}) + \sigma_{z,\ell m}^{(2)} \sigma_{z,nk}^{(2)} J_2(\omega_{\ell m}) \right] (\coth(\beta\hbar\omega_{\ell m}/2) + 1) + \\ &+ \frac{i}{4\pi\hbar} \left[\sigma_{z,\ell m}^{(2)} \sigma_{z,nk}^{(2)} \int_0^{\infty} d\omega \frac{J_2(\omega)}{\omega^2 - \omega_{\ell m}^2} (\coth(\beta\hbar\omega/2)\omega_{\ell m} + \omega) + \right. \\ &\left. + \sigma_{z,\ell m}^{(1)} \sigma_{z,nk}^{(1)} \int_0^{\infty} d\omega \frac{J_1(\omega)}{\omega^2 - \omega_{\ell m}^2} (\coth(\beta\hbar\omega/2)\omega_{\ell m} + \omega) \right]. \end{aligned} \quad (\text{C.23})$$

The rates $\Gamma_{\ell mnk}^{(+)}$ and $\Gamma_{\ell mnk}^{(-)}$ might be inserted into (4.4) to form the Redfield tensor. Note here that for $\omega_{nk} \rightarrow 0$ (and $\omega_{\ell m} \rightarrow 0$ respectively) the real part of the rates (which is responsible for relaxation and dephasing) is of value

$$\Gamma_{\ell mnk}^{(+)} = \Gamma_{\ell mnk}^{(-)} = \frac{1}{4\beta\hbar} \left[\sigma_{z,\ell m}^{(1)} \sigma_{z,nk}^{(1)} \alpha_1 + \sigma_{z,\ell m}^{(2)} \sigma_{z,nk}^{(2)} \alpha_2 \right] \quad (\text{C.24})$$

as evaluated in equation (C.21).

C.2 Two qubits coupled to one common bath

If both qubits couple to a common environment described by one common bath of harmonic oscillators one has to perform the same calculation which was done in chapter C.1 except that the interaction Hamiltonian (C.2) has to be replaced by

$$H_I = \frac{1}{2} (\sigma_z^{(1)} + \sigma_z^{(2)}) \otimes \hat{X} \quad (\text{C.25})$$

and (C.3) by

$$H_B = H_{B_1}. \quad (\text{C.26})$$

The resulting rates read

$$\begin{aligned} \Gamma_{lmnk}^{(+)} &= \frac{1}{8\hbar} \left[\sigma_{z,\ell m}^{(1)} \sigma_{z,nk}^{(1)} + \sigma_{z,\ell m}^{(1)} \sigma_{z,nk}^{(2)} + \sigma_{z,\ell m}^{(2)} \sigma_{z,nk}^{(1)} + \sigma_{z,\ell m}^{(2)} \sigma_{z,nk}^{(2)} \right] J(\omega_{nk}) \times \\ &\quad \times (\coth(\beta\hbar\omega_{nk}/2) - 1) + \frac{i}{4\pi\hbar} \left[\sigma_{z,\ell m}^{(1)} \sigma_{z,nk}^{(1)} + \sigma_{z,\ell m}^{(1)} \sigma_{z,nk}^{(2)} + \right. \\ &\quad \left. + \sigma_{z,\ell m}^{(2)} \sigma_{z,nk}^{(1)} + \sigma_{z,\ell m}^{(2)} \sigma_{z,nk}^{(2)} \right] \int_0^\infty d\omega \frac{J(\omega)}{\omega^2 - \omega_{nk}^2} (\coth(\beta\hbar\omega/2)\omega_{nk} - \omega) \end{aligned} \quad (\text{C.27})$$

and

$$\begin{aligned} \Gamma_{lmnk}^{(-)} &= \frac{1}{8\hbar} \left[\sigma_{z,\ell m}^{(1)} \sigma_{z,nk}^{(1)} + \sigma_{z,\ell m}^{(1)} \sigma_{z,nk}^{(2)} + \sigma_{z,\ell m}^{(2)} \sigma_{z,nk}^{(1)} + \sigma_{z,\ell m}^{(2)} \sigma_{z,nk}^{(2)} \right] J(\omega_{\ell m}) \times \\ &\quad \times (\coth(\beta\hbar\omega_{\ell m}/2) + 1) + \frac{i}{4\pi\hbar} \left[\sigma_{z,\ell m}^{(1)} \sigma_{z,nk}^{(1)} + \sigma_{z,\ell m}^{(1)} \sigma_{z,nk}^{(2)} + \right. \\ &\quad \left. + \sigma_{z,\ell m}^{(2)} \sigma_{z,nk}^{(1)} + \sigma_{z,\ell m}^{(2)} \sigma_{z,nk}^{(2)} \right] \int_0^\infty d\omega \frac{J(\omega)}{\omega^2 - \omega_{\ell m}^2} (\coth(\beta\hbar\omega/2)\omega_{\ell m} + \omega). \end{aligned} \quad (\text{C.28})$$

The difference between the rates for the case of two distinct baths (4.9), (4.10) are the two extra terms $\sigma_z^{(1)}\sigma_z^{(2)}$ and $\sigma_z^{(2)}\sigma_z^{(1)}$. They originate in the tracing out over the bath because in the case of one common bath all creation and annihilation operators (harmonic oscillator coordinate \hat{X} written in terms of creation and annihilation operators) in the interaction Hamiltonian $\mathbf{H}_{int} \propto \hat{X}\sigma_z^{(i)}$ ($i=1,2$) act on the same bath and therefore also terms $a^{(1)\dagger}a^{(2)}$ and $a^{(2)\dagger}a^{(1)}$ contribute to the rates. In the case of one common bath there of course is only one spectral function $J(\omega) = (\alpha\hbar\omega)/(1 + \frac{\omega}{\omega_c^2})$ which we also assume to be ohmic.

Appendix D

Calculation of the renormalization effects

Renormalization of the oscillation frequencies ω_{nm} is mediated by the imaginary part of the Redfield tensor [16]

$$\omega_{nm} \rightarrow \tilde{\omega}_{nm} := \omega_{nm} - \text{Im}R_{nmnm}. \quad (\text{D.1})$$

Thus the real part of the Redfield tensor yields the relaxation and dephasing rates while the imaginary part causes an environment induced shift of the oscillation frequencies ω_{nm} . The imaginary part of the Redfield tensor is given by the imaginary part of the rates

$$\text{Im} \Gamma_{\ell mnk}^{(+)} = \frac{1}{\pi} \int_0^{\infty} d\omega J(\omega) P\left(\frac{1}{\omega^2 - \omega_{nk}^2}\right) [\coth(\beta\hbar\omega/2)\omega_{nk} - \omega] \quad (\text{D.2})$$

and

$$\text{Im} \Gamma_{\ell mnk}^{(-)} = \frac{1}{\pi} \int_0^{\infty} d\omega J(\omega) P\left(\frac{1}{\omega^2 - \omega_{lm}^2}\right) [\coth(\beta\hbar\omega/2)\omega_{lm} + \omega]. \quad (\text{D.3})$$

Therefore one has to evaluate the integrals

$$\frac{1}{2} \int_{-\infty}^{\infty} d\omega J(\omega) P\left(\frac{1}{\omega^2 - \omega_{nk}^2}\right) [\coth(\beta\hbar\omega/2)\omega_{nk} - \omega] \quad (\text{D.4})$$

and

$$\frac{1}{2} \int_{-\infty}^{\infty} d\omega J(\omega) P\left(\frac{1}{\omega^2 - \omega_{lm}^2}\right) [\coth(\beta\hbar\omega/2)\omega_{lm} + \omega]. \quad (\text{D.5})$$

For the sake of simplicity we first only consider the case

$$\frac{1}{2} \int_{-\infty}^{\infty} d\omega J(\omega) \frac{1}{\omega^2 - \omega_{nk}^2} [\coth(\beta\hbar\omega/2)\omega_{nk} - \omega] = \frac{1}{2} \int_{-\infty}^{\infty} d\omega f_1(\omega) - \frac{1}{2} \int_{-\infty}^{\infty} d\omega f_2(\omega), \quad (\text{D.6})$$

with an ohmic spectral density $J(\omega)$:

$$J(\omega) = \frac{\alpha\omega}{1 + \frac{\omega^2}{\omega_c^2}} = \alpha\omega \frac{\omega_c^2}{\omega_c^2 + \omega^2} = \alpha\omega \frac{\omega_c^2}{(\omega_c + i\omega)(\omega_c - i\omega)}. \quad (\text{D.7})$$

This integral (D.6) might be split into two parts

$$\begin{aligned}
I_1 &= \frac{1}{2} \int_{-\infty}^{\infty} d\omega f_1(\omega) \\
&= \frac{1}{2} \int_{-\infty}^{\infty} d\omega \frac{\alpha\omega}{1 + \frac{\omega^2}{\omega_c^2}} \frac{1}{\omega - \omega_{nk}} \frac{1}{\omega + \omega_{nk}} \coth(\beta\hbar\omega/2) \omega_{nk}
\end{aligned} \tag{D.8}$$

$$I_2 = \frac{1}{2} \int_{-\infty}^{\infty} d\omega f_2(\omega) = \frac{1}{2} \int_{-\infty}^{\infty} d\omega \frac{\alpha\omega}{1 + \frac{\omega^2}{\omega_c^2}} \frac{1}{\omega - \omega_{nk}} \frac{1}{\omega + \omega_{nk}} \omega. \tag{D.9}$$

Both $f_1(\omega)$ and $f_2(\omega)$ are even: we can integrate from $-\infty$ to ∞ and simply multiply the result by 1/2 to obtain the correct expression. The poles are $\pm\omega_{nk}$, $\pm i\omega_c$ (only the “+” counts because we have chosen the upper imaginary half plane), 0, $\pm i2n\pi/\beta\hbar$ ($n \in \mathbf{N}$, $n > 0$) [58]. Carrying out the integration (D.8) yields

$$\begin{aligned}
I_1 &= i\frac{1}{2}\pi \left(\frac{1}{2\omega_{nk}} \frac{\alpha\omega_{nk}}{1 + \frac{\omega_{nk}^2}{\omega_c^2}} \coth(\beta\hbar\omega_{nk}/2) \omega_{nk} \right) + \\
&+ i\frac{1}{2}\pi \left(\frac{1}{-2\omega_{nk}} \frac{-\alpha\omega_{nk}}{1 + \frac{\omega_{nk}^2}{\omega_c^2}} \underbrace{\coth(-\beta\hbar\omega_{nk}/2)}_{-\coth(\beta\hbar\omega_{nk}/2)} \omega_{nk} \right) + \\
&- i\frac{1}{2}2\pi \left(\frac{i\alpha\omega_c}{i\omega_c - \omega_{nk}} \frac{1}{i\omega_c + \omega_{nk}} \frac{\omega_c^2}{2i\omega_c} \underbrace{\coth(\beta\hbar i\omega_c/2)}_{\frac{1}{i}\cot(\beta\hbar\omega_c/2)} \omega_{nk} \right) + \\
&+ 0 \text{ (removable discontinuity of the coth at 0)} + \\
&+ i\frac{1}{2}2\pi \sum_{n=0}^{\infty} \frac{\alpha \frac{2n\pi i}{\beta\hbar}}{1 - \left(\frac{2n\pi}{\beta\hbar}\right)^2} \frac{1}{\frac{1}{\omega_c^2} \frac{2\pi ni}{\beta\hbar} - \omega_{nk}} \frac{1}{\frac{2\pi ni}{\beta\hbar} + \omega_{nk}} \omega_{nk} \underbrace{\frac{2}{\beta\hbar}}_{a_{-1}}.
\end{aligned} \tag{D.10}$$

The first element a_{-1} of the Laurent-series expansion can easily be calculated:

$$\begin{aligned}
a_{-1} &= \frac{f_n(z_0)}{f'_d(z_0)} \left(\text{with } f = \frac{f_n}{f_d} \right) \\
&= \frac{e^{\beta\hbar\omega/2} + e^{-\beta\hbar\omega/2}}{\frac{1}{2}\beta\hbar(e^{\beta\hbar\omega/2} + e^{-\beta\hbar\omega/2})} \Big|_{\omega = \frac{2n\pi i}{\beta\hbar}} \\
&= \frac{2}{\beta\hbar}.
\end{aligned} \tag{D.11}$$

Now we consider only the last term of (D.10) enumerated by $I_{1,5}$

$$\begin{aligned}
I_{1,5} &= +\frac{1}{4}4\pi \frac{1}{\beta\hbar} \sum_{n=0}^{\infty} \left[\frac{\beta\hbar\alpha\omega_{nk}\omega_c^2}{(\omega_{nk}^2 + \omega_c^2)(\beta\hbar\omega_c - 2n\pi)} - \frac{\beta\hbar\alpha\omega_{nk}\omega_c^2}{(\omega_{nk}^2 + \omega_c^2)(\beta\hbar\omega_c + 2n\pi)} + \right. \\
&\left. + \frac{4\beta\hbar\alpha\omega_{nk}\omega_c^2 n\pi}{(\omega_{nk}^2 + \omega_c^2)(4n^2\pi^2 + \omega_{nk}^2\beta^2\hbar^2)} \right]
\end{aligned}$$

$$\begin{aligned}
&= \frac{\pi\alpha}{(\omega_{nk}^2 + \omega_c^2)} \sum_{n=0}^{\infty} \left[\frac{\omega_{nk}\omega_c^2}{\beta\hbar\omega_c - 2n\pi} - \frac{\omega_{nk}\omega_c^2}{\beta\hbar\omega_c + 2n\pi} + \frac{4\omega_{nk}\omega_c^2 n\pi}{4n^2\pi^2 + \omega_{nk}^2\beta^2\hbar^2} \right] \\
&= \frac{\pi\alpha\omega_{nk}\omega_c^2}{(\omega_{nk}^2 + \omega_c^2)} \left[\frac{4\pi}{4\pi^2} \sum_{n=0}^{\infty} \frac{n}{n^2 + \underbrace{\frac{\omega_{nk}^2\beta^2\hbar^2}{4\pi^2}}_{=:c_1^2}} + \right. \\
&\quad \left. + \frac{1}{2\pi} \sum_{n=0}^{\infty} \left(\underbrace{\frac{1}{\beta\hbar\omega_c - n}}_{=:c_2} - \frac{1}{\frac{\beta\hbar\omega_c}{2\pi} + n} \right) \right] \\
&= \frac{\pi\alpha\omega_{nk}\omega_c^2}{(\omega_{nk}^2 + \omega_c^2)} \left[\frac{1}{\pi} \sum_{n=0}^{\infty} \frac{n}{n^2 + c_1^2} - \frac{1}{2\pi} \sum_{n=0}^{\infty} \left(\frac{1}{n - c_2} + \frac{1}{n + c_2} \right) \right] \\
&= \frac{\pi\alpha\omega_{nk}\omega_c^2}{(\omega_{nk}^2 + \omega_c^2)} \left[\frac{1}{\pi} \sum_{n=0}^{\infty} \frac{n}{n^2 + c_1^2} - \frac{1}{2\pi} \sum_{n=0}^{\infty} \frac{2n}{n^2 - c_2^2} \right] \\
&= -\frac{\alpha\omega_{nk}\omega_c^2(c_2^2 + c_1^2)}{(\omega_{nk}^2 + \omega_c^2)} \sum_{n=0}^{\infty} \frac{n}{(n^2 + c_1^2)(n^2 - c_2^2)} \tag{D.12}
\end{aligned}$$

$$= -\frac{\alpha\omega_{nk}\omega_c^2(c_2^2 + c_1^2)}{(\omega_{nk}^2 + \omega_c^2)} \left[\frac{1}{2} \frac{\psi(-ic_1)}{c_2^2 + c_1^2} + \frac{1}{2} \frac{\psi(ic_1)}{c_2^2 + c_1^2} - \frac{1}{2} \frac{\psi(-c_2)}{c_2^2 + c_1^2} - \frac{1}{2} \frac{\psi(c_2)}{c_2^2 + c_1^2} \right]. \tag{D.13}$$

The properties of the digamma-function are summarized in [59]. Inserting the reflection formula $\psi(1 - z) = \psi(z) + \pi \cot \pi z$ [60] into (D.13) leads to

$$\begin{aligned}
I_{1,5} &= -\frac{\alpha\omega_{nk}\omega_c^2}{2(\omega_{nk}^2 + \omega_c^2)} \left[\psi(ic_1) + (\psi(1 + ic_1) + \pi \cot(\pi(1 + ic_1))) - \right. \\
&\quad \left. - \psi(1 + c_2) - \pi \cot(\pi(1 + c_2)) - \psi(c_2) \right] \\
&= -\frac{\alpha\omega_{nk}\omega_c^2}{2(\omega_{nk}^2 + \omega_c^2)} \left[\psi(ic_1) + \psi(1 + ic_1) - i\pi \coth(\pi c_1) - \psi(1 + c_2) - \right. \\
&\quad \left. - \pi \cot(\pi c_2) - \psi(c_2) \right]. \tag{D.14}
\end{aligned}$$

Evaluation of the second integral (D.9) gives (poles $+i\omega_c$ and $\pm\omega_{nk}$)

$$I_2 = \pi\alpha\omega_c^3 \frac{1}{2(\omega_c^2 + \omega_{nk}^2)} + \frac{\alpha\omega_{nk}^2}{1 + \frac{\omega_{nk}^2}{\omega_c^2}} \frac{1}{2} - \frac{\alpha\omega_{nk}^2}{1 + \frac{\omega_{nk}^2}{\omega_c^2}} \frac{1}{2}. \tag{D.15}$$

Now we sum up all terms for both integrals

$$\begin{aligned}
I &= I_1 - I_2 \\
&= -\frac{\pi}{2} \frac{\alpha\omega_c^2}{\omega_c^2 + \omega_{nk}^2} \cot(\beta\hbar\omega_c/2)\omega_{nk} - \frac{\alpha\omega_{nk}\omega_c^2}{2(\omega_{nk}^2 + \omega_c^2)} \left[\psi(ic_1) + \psi(1 + ic_1) - \right. \\
&\quad \left. - i\pi \coth(\pi c_1) - \psi(1 + c_2) - \pi \cot(\pi c_2) - \psi(c_2) \right] - \pi\alpha\omega_c^3 \frac{1}{2(\omega_c^2 + \omega_{nk}^2)}
\end{aligned}$$

$$\begin{aligned}
&= \frac{\alpha\omega_c^2\omega_{nk}}{2(\omega_c^2 + \omega_{nk}^2)} \left[(1-1)\pi\cot(\pi c_2) - \psi(ic_1) - \psi(1+ic_1) + \right. \\
&\quad \left. + i\pi\coth(\pi c_1) + \psi(1+c_2) + \psi(c_2) - \pi\frac{\omega_c}{\omega_{nk}} \right] \\
&= \frac{\alpha\omega_c^2\omega_{nk}}{2(\omega_c^2 + \omega_{nk}^2)} \left[\psi(1+c_2) + \psi(c_2) - 2\text{Re}[\psi(ic_1)] - \pi\frac{\omega_c}{\omega_{nk}} \right]. \tag{D.16}
\end{aligned}$$

The result (D.16) is discussed in chapter 4.6. To circumvent problems with the points $c_1 = 0$ or $c_2 = 0$ when implementing the formula with a computer, one could also start summation in (D.12) at $n = 1$. The resulting expressions are

$$\text{Im } \Gamma_{\ell mnk}^{(+)} = C_{1b,2b} \frac{1}{\pi} \frac{\alpha\omega_c^2\omega_{nk}}{2(\omega_c^2 + \omega_{nk}^2)} \left[\psi(1+c_2) + \psi(c_2) - 2\text{Re}[\psi(ic_1)] - \pi\frac{\omega_c}{\omega_{nk}} \right] \tag{D.17}$$

and

$$\text{Im } \Gamma_{\ell mnk}^{(-)} = C_{1b,2b} \frac{1}{\pi} \frac{\alpha\omega_c^2\omega_{lm}}{2(\omega_c^2 + \omega_{lm}^2)} \left[\psi(1+c_2) + \psi(c_2) - 2\text{Re}[\psi(ic_1)] + \pi\frac{\omega_c}{\omega_{lm}} \right], \tag{D.18}$$

where $c_1 := (\omega_{lm}\beta\hbar)/(2\pi)$ for $\Gamma_{\ell mnk}^{(-)}$. Here $C_{1b,2b}$ denotes a pre-factor, which reads in the case of two distinct baths

$$C_{2b} = \frac{1}{4} \left[\sigma_{z,\ell m}^{(1)} \sigma_{z,nk}^{(1)} + \sigma_{z,\ell m}^{(2)} \sigma_{z,nk}^{(2)} \right] \tag{D.19}$$

and in the case of one common bath

$$C_{1b} = \frac{1}{4} \left[\sigma_{z,\ell m}^{(1)} \sigma_{z,nk}^{(1)} + \sigma_{z,\ell m}^{(1)} \sigma_{z,nk}^{(2)} + \sigma_{z,\ell m}^{(2)} \sigma_{z,nk}^{(1)} + \sigma_{z,\ell m}^{(2)} \sigma_{z,nk}^{(2)} \right]. \tag{D.20}$$

List of symbols

List of symbols

Symbol	Explanation	Equation
$\hat{\sigma}_{x,y,z}$	Pauli spin operators	
$\curvearrowright, (\curvearrowright\rangle = 1\rangle)$	Clockwise flowing current	
$\curvearrowleft, (\curvearrowleft\rangle = 0\rangle)$	Counterclockwise flowing current	
I_c	Critical current of a Josephson junction	(2.1)
γ	Gauge invariant phase	(2.2), (6.13)
E_C	Charging energy	Section 2.1
E_J	Josephson energy	(2.3)
F	Coupling free energy	(2.3)
Q	Charge	(2.4)
C_J	Capacitance of a Josephson junction	(2.4)
Φ_0	Magnetic flux quantum $\Phi_0 = h/2e$	(2.4)
Φ_x	Externally applied bias flux	(2.4), figure 2.2
$\Delta_{1,2}$	Transmission amplitude of a single qubit	(2.6)
$\epsilon_{1,2}$	Energy bias of a single qubit	(2.6)
K	Inter-qubit coupling strength	(2.7)
ϵ	Energy bias of the two-qubit system ($\epsilon = \epsilon_1 + \epsilon_2$)	(2.10)
η	Transmission amplitude of the two-qubit system ($\eta = \Delta_1 + \Delta_2$)	(2.10)
\mathbf{H}_{2qb}	Two qubit Hamiltonian	(2.7), (2.10), (2.14)
\mathbf{H}_{op}^{2b}	Two qubit Hamiltonian; the two qubits couple to two distinct baths	(2.8), (2.11), (2.12)
\mathbf{H}_{op}^{1b}	Two qubit Hamiltonian; the two qubits couple to one common bath	(2.9), (2.13)
$ E1\rangle, E2\rangle, E3\rangle, E4\rangle$	Eigenstates of the two qubit system	Section 2.4
ω_{nm}	Transition frequency between energy levels n and m	Section 2.4, (4.3)
$\hat{V}(t)$	Periodic perturbation of the two-qubit Hamiltonian	(3.3)

Symbol	Explanation	Equation
T	Temperature	
β	Inverse temperature, $\beta = 1/(k_B T)$	
$P_\Psi(t)$	Occupation probability of the state Ψ at time t	
$\rho(t)$	Reduced density matrix	(4.3)
R_{nmkl}	Redfield relaxation tensor	(4.4)
$\Gamma_{lmnk}^{(+),(-)}$	Golden Rule rates	(4.5), (4.6)
α	Dimensionless parameter which gives the strength of the dissipative effects [34]	(4.8)
ω_c	Cutoff-frequency	(4.8)
$J(\omega)$	Spectral function	(4.8)
\tilde{R}_i	Eigenvalues of the Redfield-tensor, written as a diagonal matrix	Section 4.2
\hat{X}	Coordinate of the bath of harmonic oscillators	Section 4.2
$\Gamma_{\varphi_{ij}}$	Dephasing rates	Section 4.4
Γ_R	Relaxation rate	Section 4.4
\mathcal{F}	Fidelity	(5.1)
\mathcal{P}	Purity	(5.2)
\mathcal{Q}	Quantum degree	(5.3)
\mathcal{C}	Entanglement capability	Chapter 5
U_{XOR}	XOR (CNOT) quantum gate operation	(5.6), (5.7)
I_1	Circulating current in qubit 1	Figure 6.2, (6.2), (6.3)
I_2	Circulating current in qubit 2	Figure 6.2, (6.2), (6.3)
M_{QQ}	Self-inductance of a qubit	Table 6.1
M_{TT}	Self-inductance of the flux transformer	Table 6.1
M_{QT}	Mutual inductance between qubit and flux transformer	Table 6.1
I_S	Screening current in the flux transformer loop	Figure 6.2, (6.7)
Φ_S	Screening flux	Section 6.2.1
L	Geometric inductance	Figure 6.3
Y	Admittance	(6.23)
L_J	Josephson inductance	(6.29)
Z	Partition function	(C.8)

List of constants

Symbol	Explanation
$e = 1.60 \cdot 10^{-19}$ C	Electron charge
$h = 6.63 \cdot 10^{-34}$ Js	Planck constant
$\hbar = 1.05 \cdot 10^{-34}$ Js	Reduced Planck constant
$k_B = 1.38 \cdot 10^{-23}$ J/K	Boltzmann constant
$\Phi_0 = 2.07 \cdot 10^{-15}$ Wb	Magnetic flux quantum

List of Figures

2.1	Equivalent circuit diagram and image of a Josephson junction.	7
2.2	Equivalent circuit diagram and image of a flux qubit.	7
2.3	Schematic representation of the persistent-current states of a superconducting qubit loop.	8
2.4	Superconducting single qubit loop and the switching SQUID.	9
2.5	3d plot of the energy spectrum of the coupled two qubit system.	12
2.6	Plot of the eigenenergies of the eigenstates $ E1\rangle$, $ E2\rangle$, $ E3\rangle$ and $ E4\rangle$	13
2.7	Plot of the amplitude of the different singlet/triplet states of which the eigenstates denoted by $ E1\rangle$, $ E2\rangle$, $ E3\rangle$ and $ E4\rangle$ are composed for the four eigenstates.	15
3.1	Plot of the squared absolute value of the matrix elements (3.5)-(3.14) for different parameters.	19
3.2	Plot of the transition frequencies ω_{32} , ω_{42} and ω_{31}	20
3.3	Plot of the transition frequencies ω_{21} , ω_{41} and ω_{34}	21
4.1	Plot of the occupation probability of the four eigenstates $ E1\rangle$, $ E2\rangle$, $ E3\rangle$ and $ E4\rangle$ for initially starting in one of the eigenstates at $T = 0$ K.	26
4.2	Plot of the occupation probability of the four eigenstates $ E1\rangle$, $ E2\rangle$, $ E3\rangle$ and $ E4\rangle$ for initially starting in one of the eigenstates at $T = 100$ mK.	27
4.3	Plot of the occupation probability $P_{ 11\rangle}(t) = P_{ \uparrow\uparrow\rangle}(t) = \langle 11 \rho(t) 11\rangle$ for starting in the initial state $ 11\rangle$ at $t = 0$ s and $T = 0$ K.	28
4.4	Plot of the occupation probability $P_{(1/\sqrt{2})(E3\rangle+ E4\rangle)}(t)$ when starting in the initial state $(1/\sqrt{2})(E3\rangle + E4\rangle)$ at $T = 0.1$ K.	29
4.5	Log-log plot of the temperature dependence of the sum of the four relaxation rates and selected dephasing rates.	30
4.6	Plot of the temperature dependence of the sum of the four relaxation rates and selected dephasing rates.	32
4.7	Illustration of the size of the renormalization effects.	34
5.1	Pulse sequence needed to perform the quantum XOR operation.	39
5.2	Temperature dependence of the gate quality factors.	40
5.3	Log-log plot of the temperature dependence of the deviations of the four gate quantifiers from their ideal values.	41
5.4	Dissipation strength dependence of the deviation of the gate quality factors from their ideal values in log-log representation.	42
5.5	Time resolved XOR operation. The system is initially prepared in the state $ 00\rangle$	43
5.6	Time resolved XOR operation. The system is initially prepared in the state $ 11\rangle$	44

5.7	Time resolved Purity during the quantum XOR operation.	45
6.1	Schematic sketch of a Josephson field-effect transistor and image of a SNS transistor.	46
6.2	Schematic sketch of the flux transformer circuit.	47
6.3	Equivalent circuit diagram of the flux transformer.	50

List of Tables

5.1	Parameters of the Hamiltonians, only the non-zero parameters are listed; $\xi = 1$ GHz in our case.	38
6.1	Explanation of the several inductances introduced the circuit depicted in figure 6.2.	48

Bibliography

- [1] P. Shor, in Proc. 35th Ann. Symp. on the Foundations of Computer Science (ed. S. Goldwasser), pp. 124-134 (IEEE Computer Society Press, Los Alamitos, California, 1994)
- [2] L.K. Grover: *Quantum Mechanics Helps in Searching for a Needle in a Haystack*, Phys. Rev. Lett. **79**, 325 (1997)
- [3] D. Deutsch: *Quantum theory, the Church-Turing principle and the universal quantum computer*, Proc. R. Soc. Lond. A **400**, 97 (1985)
- [4] C.H. Bennett: *Quantum information and computation*, Phys. Today **48**(10), 24 (1995)
- [5] D.P. DiVincenzo: *Quantum Computation*, Science **269**, 255 (1995)
- [6] L.M.K. Vandersypen, M. Steffen, G. Breyta, C.S. Yannoni, M.H. Sherwood, I.L. Chuang: *Experimental realization of Shor's quantum factoring algorithm using nuclear magnetic resonance*, Nature **414**, 883 (2001)
- [7] M.A. Nielsen, I.L. Chuang: *Quantum Computation and Quantum Information*, Cambridge University Press (2000)
- [8] S. Lloyd: *A potentially realizable quantum computer*, Science **261**, 1569 (1993)
- [9] D. Loss and D.P. DiVincenzo: *Quantum computation with quantum dots*, Phys. Rev. A **57**, 120 (1998)
- [10] R.H. Blick and H. Lorenz: *Coherent modes in artificial molecules - possible definition of quantum bits in coupled quantum dots*, ISCAS 2000 proceedings, pp. II245-II248
- [11] U. Hartmann and F.K. Wilhelm, phys. stat. sol. (b) **233**, No. 3 (2002)
- [12] A.J. Leggett: *Superconducting Qubits-a Major Roadblock Dissolved?*, Science **296**, 861 (2002)
- [13] C.H. van der Wal: *Quantum Superpositions of Persistent Josephson Currents*, Ph.D. thesis TU Delft (2001)
- [14] Y. Makhlin, G. Schön, A. Shnirman: *Quantum-state engineering with Josephson-junction devices*, Rev. Mod. Phys. **73**, 357 (2001)
- [15] L. Tian: *A Superconducting Flux QuBit: Measurement, Noise and Control*, Ph.D. thesis MIT (2002)

- [16] M. Governale, M. Grifoni, G. Schön: *Decoherence and dephasing in coupled Josephson-junction qubits*, Chem. Phys. **268**, 273 (2001)
- [17] G.J. Milburn, R. Laflamme, B.C. Sanders, E. Knill: *Quantum dynamics of coupled qubits*, Phys. Rev. A **65**, 032316 (2002)
- [18] M. Dubé and P.C.E. Stamp: *Dynamics of a pair of interacting spins coupled to an environmental sea*, Int. J. Mod. Phys. B **12**, 1191 (1998)
- [19] Y. Makhlin, G. Schön, A. Shnirman: *Josephson-junction qubits with controlled couplings*, Nature **398**, 305 (1999)
- [20] S. Lloyd: *Almost Any Quantum Logic Gate is Universal*, Phys. Rev. Lett. **75**, 346 (1995)
- [21] P.N. Argyres and P.L. Kelley: *Theory of Spin Resonance and Relaxation*, Phys. Rev. **134**, A98 (1964)
- [22] K. Blum: *Density Matrix Theory and Applications*, Plenum Pub. Corp. (1981)
- [23] L. Hartmann et al.: *Driven tunneling dynamics: Bloch-Redfield theory versus path-integral approach*, Phys. Rev. E **61**, 4687 (2000)
- [24] J.F. Poyatos, J.I. Cirac, P. Zoller: *Complete Characterization of a Quantum Process: The Two-Bit Quantum Gate*, Phys. Rev. Lett. **78**, 390 (1997)
- [25] M. Tinkham: *Introduction to Superconductivity*, McGraw-Hill (1996)
- [26] Y. Nakamura, Yu. A. Pashkin, J.S. Tsai: *Coherent control of macroscopic quantum states in a single-Cooper-pair box*, Nature **398**, 786 (2002)
- [27] D. Vion, A. Aassime, A. Cottet, P. Joyez, H. Pothier, C. Urbina, D. Esteve and M.H. Devoret: *Manipulating the Quantum State of an Electrical Circuit*, Science **296**, 886 (2002)
- [28] J.R. Friedman, V. Patel, W. Chen, S.K. Tolpygo, J.E. Lukens: *Quantum superposition of distinct macroscopic states*, Nature **406**, 43 (2000)
- [29] T.P. Orlando, J.E. Mooij, C.H. van der Wal, L. Levitov, S. Lloyd, J.J. Mazo: *A Superconducting Persistent Current Qubit*, Phys. Rev. B **60**, 15398 (1999)
- [30] Y. Nakamura et al.: *Rabi oscillations in a josephson-junction charge two-level system*, Phys. Rev. Lett. **87**, 246601 (2001)
- [31] Y. Nakamura et al., priv. comm. (2002)
- [32] C.H. van der Wal, F.K. Wilhelm, C.J.P.M. Harmans, and J.E. Mooij: *Engineering decoherence in Josephson persistent-current qubits*, submitted
- [33] T.P. Orlando, L. Tian, D.S. Crankshaw, S. Lloyd, C.H. van der Wal, J.E. Mooij, F.K. Wilhelm: *Engineering the quantum measurement process for the persistent current qubit*, Physica C **368**, 294 (2002)
- [34] A.J. Leggett, S. Chakravarty, A.T. Dorsey, M.P.A. Fisher, A. Garg, W. Zwerger : *The dissipative two state system*, Rev. Mod. Phys **59**, 1 (1987)

- [35] I. Goychuk, priv. comm. (2002)
- [36] D.A. Lidar, I.L. Chuang and K.B. Whaley: *Decoherence Free Subspaces for Quantum Computation*, Phys. Rev. Lett. **81**, 2594 (1998)
- [37] J. Kempe, D. Bacon, D.A. Lidar, and K.B. Whaley: *Theory of decoherence-free fault-tolerant universal quantum computation*, Phys. Rev. A **63**, 042307 (2001)
- [38] M.S. Byrd and D.A. Lidar: *Comprehensive Encoding and Decoupling Solution to Problems of Decoherence and Design in Solid-State Quantum Computing*, Phys. Rev. Lett. **89**, 047901 (2002)
- [39] P. Zanardi, priv. comm. (2002)
- [40] H. Majer, priv. comm. (2002)
- [41] T. Fließbach: *Quantenmechanik*, Spektrum Verlag (1995)
- [42] U. Weiss: *Quantum Dissipative Systems*, World Scientific (1999)
- [43] C. Cohen-Tannoudji, B. Diu, F. Laloë: *Quantum Mechanics*, Vol. 1, chapter 4
- [44] M.C. Goorden: *Theory of Josephson persistent-current qubits with driving and dissipation*, Master's thesis, TU Delft (2002)
- [45] S. Kehrein and M. Vojta: *Soliton Fermi sea in models of Ising-coupled Kondo impurities*, preprint (2002)
- [46] C.H. Bennett, G. Brassard, S. Popescu, B. Schumacher, J.A. Smolin, and W.K. Wootters: *Purification of Noisy Entanglement and Faithful Teleportation via Noisy Channels*, Phys. Rev. Lett. **76**, 722 (1996); J.F. Clauser, M.A. Horne, A. Shimony, and R.A. Holt: *Proposed Experiment to Test Local Hidden-Variable Theories*, Phys. Rev. Lett. **23**, 880 (1969)
- [47] M. Thorwart, P. Hänggi: *Decoherence and dissipation during a quantum XOR gate operation*, Phys. Rev. A **65**, 012309 (2001)
- [48] A. Peres: *Separability Criterion for Density Matrices*, Phys. Rev. Lett. **77**, 1413 (1996)
- [49] A. Barenco, C.H. Bennett, R. Cleve, D.P. DiVincenzo, N. Margolus, P. Shor, T. Sleator, J.A. Smolin, and H. Weinfurter: *Elementary Gates For Quantum Computation*, Phys. Rev. A **52**, 3457 (1995)
- [50] P. Baars, A. Richter and U. Merkt: *Elektrischer Transport in Nb/InAs-HEMT Josephsonkontakten*, DPG-Tagung, Poster TT 7.14 (2002)
- [51] I.O. Kulik and A.N. Omelyanchuk, Sov. J. Low Temp. Phys. **3**, 459 (1977)
- [52] K.K. Likharev: *Superconducting weak links*, Rev. Mod. Phys. **51**, 101 (1979)
- [53] A.J. Leggett: *Quantum tunneling in the presence of an arbitrary linear dissipation mechanism*, Phys. Rev. B **30**, 1208 (1984)

- [54] A. Richter: *Nb/InAs(2DEG)/Nb hybrid quantum structures*, Advances in Solid State Physics Vol. **40**, 321
- [55] S. Keil et al.: *Imaging of Vortices and 1/f Noise Sources in YBCO dc SQUIDs Using Low-Temperature Scanning Electron Microscopy*, IEEE Trans. Appl. Supercond. **9**, 2961 (1999)
- [56] C.H. van der Wal et al.: *Quantum Superposition of Macroscopic Persistent-Current States*, Science **290**, 773 (2000)
- [57] I.L. Chuang, L.M.K. Vandersypen, X. Zhou, D.W. Leung, S. Lloyd: *Experimental realization of a quantum algorithm*, Nature **393**, 143 (1998)
- [58] G.B. Arfken and H.J. Weber: *Mathematical Methods for Physicists*, Harcourt (2001)
- [59] I.E. Stegun, M. Abramowitz: *Handbook of Mathematical Functions*, Dover Publications, New York, 1st edition (1965)
- [60] W. Magnus, F. Oberhettinger, R.P. Soni: *Formulas and Theorems for the Special Functions of Mathematical Physics*, Springer (1966)